

**Kinematic Fit of $t\bar{t}$ Events
in the Semi-Leptonic Decay Channel
with a χ^2 Method at the ATLAS Experiment**

Diplomarbeit

[Nr.: II.Physik-UniGö-Dipl-2008/01]

vorgelegt von

Matthias Stein

aus

Göttingen

angefertigt im

II. Physikalisches Institut
der Georg-August-Universität zu Göttingen

2008

GEORG-AUGUST-UNIVERSITÄT GÖTTINGEN

II. Physikalisches Institut

Kinematic Fit of $t\bar{t}$ Events in the Semi-Leptonic Decay Channel with a χ^2 Method at the ATLAS Experiment

Matthias Stein

(Place of birth: Göttingen)

In this thesis a kinematic χ^2 fit of a $t\bar{t}$ system in the semi-leptonic decay channel is established and applied to a Monte Carlo signal sample of simulated ATLAS data in NLO. A jet-parton matching is performed allowing the explicit reconstruction of the decay topology in $(20.1 \pm 5.5)\%$ of the events. Investigations of the improvement of the energy resolution due to the fit are performed, yielding $(5.25 \pm 0.05)\%$ for light quark jets and $(3.88 \pm 0.05)\%$ for b quark jets.

The calibration of the Jet Energy Scale of the calorimeter is investigated, as well as b -tagging efficiencies, the fit of the transverse momentum of the $t\bar{t}$ system and the reconstruction of the top quark mass.



Post address:
Friedrich-Hund-Platz 1
37077 Göttingen
Germany

II. Physikalisches Institut
Georg-August-Universität Göttingen
April 2008

GEORG-AUGUST-UNIVERSITÄT
GÖTTINGEN

II. Physikalisches Institut

**Kinematic Fit of $t\bar{t}$ Events in the Semi-Leptonic Decay Channel
with a χ^2 Method at the ATLAS Experiment**

von

Matthias Stein

(Geburtsort: Göttingen)

Dieser Forschungsbericht wurde als Diplomarbeit von der Fakultät für Physik der Georg-August-Universität zu Göttingen angenommen.

Angenommen am: 25. April 2008
Referent: Prof. Quadt
Korreferent: Prof. Klute

Contents

1. Introduction	1
2. Physics	3
2.1. The Standard Model of Particle Physics	3
2.2. Top Quark Physics	5
2.2.1. Top Quark Production via Strong Interaction	6
2.2.2. Top Quark Production via the Electroweak Interaction	8
2.2.3. Top Quark Decay	8
2.2.4. Background Processes	10
3. Experimental Setup	13
3.1. The Large Hadron Collider	13
3.2. The ATLAS Detector	15
3.2.1. Tracking System	15
3.2.2. Calorimeter System	18
3.2.3. Muon System	21
3.2.4. Magnet System	22
3.2.5. Trigger System and Data Acquisition	23
4. Kinematic Fit – The Mathematical Concept	25
4.1. χ^2 without Constraints	25
4.2. χ^2 with Linear Constraints – The Method of the Lagrangian Multipliers	27
5. Test of the χ^2 Method: $\pi^0 \rightarrow \gamma\gamma$	29
5.1. Development of the Lagrange Function	29
5.2. Description of the Used Data	31
5.3. Studies with the KF	32
5.3.1. Parameter Space of the Lagrange Function of a Single Event	32
5.3.2. Studies of the Energy Resolution	33
6. Application of the χ^2 Method: $t\bar{t} \rightarrow q\bar{q}b\bar{b}e\bar{\nu}_e$	35
6.1. Development of the Lagrange Function	35
6.2. Description of the Used Data	40
6.2.1. $t\bar{t}$ Events Generated with MadEvent	40
6.2.2. $t\bar{t}$ Events Generated with MC@NLO Using TopView	41
6.3. Overview of the Performed Studies	45
6.4. Parameter Space of the Lagrange Function of a Single Event	46
6.5. Studies with the Kinematic Fit Using MadEvent Data – Gaussian smeared	48
6.5.1. Studies of the Energy Resolution	48
6.5.2. Reconstruction of the Decay Topology of $t\bar{t}$ Events	50

6.5.3.	b -tagging Efficiencies	51
6.5.4.	Reconstruction of the Top Quark Mass	52
6.5.5.	Studies of the Transverse Momentum of the $t\bar{t}$ System	54
6.6.	Studies with the Kinematic Fit Using MadEvent Data – ATLAS Smeared	57
6.6.1.	Studies of the Energy Resolution	57
6.6.2.	Reconstruction of the Decay Topology of $t\bar{t}$ Events	58
6.6.3.	b -tagging Efficiencies	59
6.6.4.	Reconstruction of the Top Quark Mass	60
6.6.5.	Studies of the Transverse Momentum of the $t\bar{t}$ System	60
6.7.	Studies with the Kinematic Fit Using Simulated ATLAS Data	61
6.7.1.	JES – Calibration	61
6.7.2.	JES – Sensitivity of the Kinematic Fit	63
6.7.3.	Studies of the Energy Resolution	67
6.7.4.	Reconstruction of the Decay Topology of $t\bar{t}$ Events	69
6.7.5.	b -tagging Efficiencies	70
6.7.6.	Reconstruction of the Top Quark Mass	71
6.7.7.	Studies of the Transverse Momentum of the $t\bar{t}$ System	72
6.7.8.	Studies of the Energy Resolution Including Jet Combinatorics	73
7.	Conclusion and Outlook	75
7.1.	Summary and Conclusion	75
7.2.	Outlook	76
A.	Notation	79
B.	Auxiliary Calculations	81
B.1.	Determination of the Lagrangian Multipliers	81
B.2.	Reconstruction of the Neutrino	82
B.3.	Derivatives of the Equal Mass Constraint	84
C.	A Brief Outline of a Likelihood Function	89
	Bibliography	90
	Acknowledgements	95

1. Introduction

The Standard Model of particle physics summarises today's grasp of the building blocks of nature and the interactions between them. Huge efforts have been made to build larger and larger machines to investigate the fundamental particles of our world.

However, there are still many unanswered questions. Humans have always wondered how the Universe works and what it is composed of. Undiscovered particles like the Higgs boson or super-symmetric particles, the existence of extra dimensions or the nature of the mysterious dark matter are just a few keywords for the riddles which fascinate scientists today. Therefore, the construction of the Large Hadron Collider is in progress – a tool which allows to solve some of the questions which are still open. With the Large Hadron Collider higher energies than ever before can be reached. Pushing technological limits onward, the realm of the Terascale (up to 14 TeV) will be reached. The commissioning of such a complex machine is neither trivial nor optional. Data calibration methods are needed for the calibration, alignment and data selection for instance. One *standard candle* for calibration comes from top quark physics: the invariant mass of a top quark is the most precisely measured quark mass ($m_{top} = 172.6 \pm 0.8$ (stat) ± 1.1 (syst) GeV/c²) [1]. Hence, developing data calibration methods using top quark events gives a good possibility to calibrate a detector and to prepare it for data taking.

In this thesis a data calibration method – the *kinematic fit* – is presented. It is a powerful tool which is applied to the example of top quark physics. The kinematic fit offers the possibility to calibrate the calorimeter of a particle detector. It uses fundamental laws of nature like energy- and momentum conservation to establish a model of a physics process. Therefore, it contains the potential to be sensitive to the Jet Energy Scale of a calorimeter.

In the presented studies the kinematic fit is applied to the semi-leptonic decay of a $t\bar{t}$ system. A next-to-leading-order signal sample of simulated $t\bar{t}$ events with respect to the ATLAS detector is examined. Certain assumptions are made for the decay pattern, yielding constraints which are included into the fit model. Thereby, physical information is integrated into the fit which results in an improvement of the relative energy resolution of the involved particle energies. Consequently, the kinematic fit provides an estimation of the *true* particle energies. This allows to evaluate the assignment of the detector signals to the partons of the decay. Hence, the method also contains the potential of the explicit reconstruction of the event topology. Additionally, the determination of the energy of an undetectable particle (the neutrino) is also realised.

In this thesis the χ^2 method is used in order to realise the kinematic fit. It is extended by the method of Lagrangian multipliers to take the constraints into account. The focus of the presented studies is on the calibration of the jet energy scale, the improvement of the energy resolution and the reconstruction of the event topology. As further applications, the identification efficiency of b quark jets and the reconstruction of the invariant mass of the top quark are investigated. The consideration of the transverse momentum of the $t\bar{t}$ system is also examined.

Since the application of the kinematic fit results in an improvement of the relative energy resolution it offers the potential for *physics beyond detector resolution*.

In the following chapter, the Standard Model of particle physics is introduced. The top quark is discussed in more detail, since the presented data calibration method relies on top quark physics. Its signature and background processes are also described.

Chapter 3 introduces the experimental setup to which the used data is referred, namely the ATLAS detector along with the Large Hadron Collider. The components of the ATLAS detector are presented, among which the calorimeter is discussed more precisely.

In Chapter 4 the mathematical concept of the kinematic fit is demonstrated by deriving the χ^2 method from a more general principle, the Likelihood method. Subsequently, the method is extended by the method of the Lagrangian multipliers.

The kinematic fit is applied to the simple example of the decay of a pion into two photons in Chapter 5. This is done in order to verify of the concept of the χ^2 method and to test its performance. Therefore, the Lagrange function of the decay is established and its parameter space is analysed for a single event, before the energy resolution is tested for an ensemble of particles.

Eventually, in Chapter 6 the method is applied to the decay of a $t\bar{t}$ system via the semi-leptonic channel. Firstly, the corresponding Lagrange function is developed. For a systematic investigation of the method, different data sources are used. They are described, before the kinematic fit is applied to the data. The motivation is to test the method with simple events on parton level and subsequently, with more realistic data, simulated with respect to the properties of the ATLAS detector. The results of the kinematic fit are presented for each data set separately. Various modifications of the method are carried out in order to study systematic effects. The same investigations as for the pion decay are performed. However, multiple additional aspects are examined: the calibration and variation of the jet energy scale, the efficiency of the reconstruction of the event topology and the b -tagging, the reconstruction of the top quark mass and the introduction of the transverse momentum into the kinematic fit. Finally, the energy resolution of light quark and b quark jets are investigated considering jet combinatorics.

A conclusion and an outlook can be found in Chapter 7. The appendix contains references, a notation index, detailed calculations and acknowledgments.

2. Physics

The Standard Model of particle physics (SM) is introduced in this chapter. Since the studies presented in this thesis are applied to top quark physics, an emphasis is placed on the top quark, its properties, production- and decay processes. Additionally, background processes are mentioned concerning the signature which is subject of the presented studies.

2.1. The Standard Model of Particle Physics

The SM describes the properties of all known particles and the interaction between them [2–4]. There are four fundamental interactions based on certain gauge symmetries: the electromagnetic force ($U(1)$), the weak force ($SU(2)$), the strong force ($SU(3)$) and gravitation. The latter one is not described in the SM due to its relative weak strength. The first three forces are described by quantum field theories. The theory describing the electromagnetic interaction is called Quantum Electro Dynamics (QED). It is unified with the weak force resulting in the electroweak force. The strong interaction is described by Quantum Chromo Dynamics (QCD).

The forces between the particles are believed to be mediated by *gauge bosons*. Gauge bosons are particles with an integer spin. The mediator for the electromagnetic force is the photon (γ) and for the weak force there are the neutral Z^0 - and charged W^\pm -bosons. The strong force is mediated by eight gluons (g). Thus, there are 12 gauge bosons in total.

The SM of particles physics also predicts a particle called Higgs-boson (H) which has not yet been discovered [5]. Its corresponding Higgs field is held responsible for the mass of all particles via a spontaneous breaking of the gauge symmetry. In the *Higgs-mechanism* a Higgs field is introduced which interacts with the fields of the other gauge bosons and with itself. Table 2.1 gives a short summary of the four fundamental forces and some of their properties.

Table 2.1.: The fundamental forces, their mediators and some of their properties. Gravitation is not included in the SM.

Force	Mediator	Rel. strength	Range	Mass
Strong	8 gluons g	1	10^{-15} m	0 GeV
Electromagnetic	photon γ	10^{-2}	∞	0 GeV
Weak	W^\pm, Z^0	10^{-6}	10^{-18} m	≈ 80 GeV, ≈ 91 GeV
Gravitation	graviton G	$< 10^{-40}$	∞	0 GeV

There are three families of particles, each consisting of one doublet of leptons and one doublet of quarks. A doublet contains two particles which differ in their so-called weak *isospin*. The isospin is an abstract quantum number. Via the Isospin formalism transitions of particles can be described for instance.¹

¹An up- and a down quark can be interpreted as the same particle in a different state, characterized by the isospin.

For the leptons there are the electron (e) and its neutrino (ν_e), the muon (μ) and its neutrino (ν_μ) and the tau (τ) and its neutrino (ν_τ). The quark doublets consist of up- (u) and down quark (d), charm- (c) and strange quark (s) and bottom- (b) and top quark (t). The quarks are carriers of an abstract *color charge* which can be *red*, *green* or *blue*. Leptons and quarks are called *fermions*. Each fermion has an anti-particle with opposite charge (12 leptons, 36 quarks). Consequently, with the gauge bosons and the Higgs boson, there are 61 particles altogether.

Processes in which a certain quark flavour (e.g. an up-quark) changes into another flavour (e.g. a down-quark) have been observed. Processes between different families are rare but have been measured too. The Cabbibo-Kobayashi-Maskawa matrix (CKM matrix) describes the mixing of all known quark flavours within a 3×3 matrix, whereas its squared entries $|V_{xy}|^2$ give a measure for the transition probability of flavour x to flavour y . A schematic representation of the fermions of the SM and their isospin doublets is given in Table 2.2.

Table 2.2.: Schematic representation of the fermions of the SM and their isospin doublets. They are grouped in three families. The mass of the fermions increases with increasing family number.

Family :	I	II	III
Quarks :	$\begin{pmatrix} u \\ d \end{pmatrix}$	$\begin{pmatrix} c \\ s \end{pmatrix}$	$\begin{pmatrix} t \\ b \end{pmatrix}$
Leptons :	$\begin{pmatrix} \nu_e \\ e \end{pmatrix}$	$\begin{pmatrix} \nu_\mu \\ \mu \end{pmatrix}$	$\begin{pmatrix} \nu_\tau \\ \tau \end{pmatrix}$

All quarks and leptons are spin-half particles and therefore underlie the Pauli Principle. The Pauli Principle postulates that two identical fermions can not occupy the same quantum state simultaneously. Experiments have shown that the spatial extension of fermions is smaller than 10^{-18} m. Their masses increase with increasing family number. The masses of the W - and Z -bosons with $m_W \approx 80 \text{ GeV}/c^2$ and $m_Z \approx 91 \text{ GeV}/c^2$ are large compared to the mass of an up quark for instance $m_u \approx 2 \text{ MeV}/c^2$ [6]. Thus in scattering processes, they exist only for a very short period of time as virtual particles², according to the Heisenberg uncertainty principle which postulates that one can not measure two non-commutative observables – like time and energy e.g. – with arbitrary precision. Therefore, the range of the weak force is small (about 10^{-18} m).

Neutrino oscillations have been observed recently [7–9] – a phenomenon which only occurs when a mass difference between neutrinos of different flavours exists. The mixing of neutrinos can be described by the Pontecorco-Maki-Nakagawa-Sakata matrix (PMNS matrix). Consequently, at least two neutrinos must have a finite mass. The masses of the electron, muon and tau also increase with increasing family number. The mass hierarchy of the neutrinos has not yet been verified.

²A virtual particle does not need to fulfill the relation $E^2 - \vec{p}^2 = m^2$, where E is the energy, \vec{p} the momentum and m the mass of the particle, respectively.

2.2. Top Quark Physics

The top quark is the weak isospin partner of the bottom-quark. It has been discovered in 1995 at the CDF and DØ experiments at the Fermi National Accelerator Laboratory (FNAL) [10, 11]. One noticeable property is its large mass. This implies the very short lifetime of about $4.2 \cdot 10^{-25}$ s of the top quark.³ As the hadronisation time scale is about 10^{-23} s, no hadrons made of top quarks have been observed yet.

Except for these characteristics of the top quark there are further motivations to study top quark physics: the prediction for the value of the Higgs mass strongly depends on the top quark mass (Figure 2.1). This is due to the fact that the Higgs boson couples most strongly to the top quark because the coupling to fermions is proportional to their masses and the top quark is the most massive fermion. There are also studies in which top quark events form background processes for physics beyond the SM. Therefore, understanding top quark physics also means being better prepared for the discovery of new physics.

The top quark mass also provides a *standard candle* for particle detectors: it offers the possibility to calibrate a particle detector.

In the following, the production- and decay processes of the top quark as well as some background processes are described.

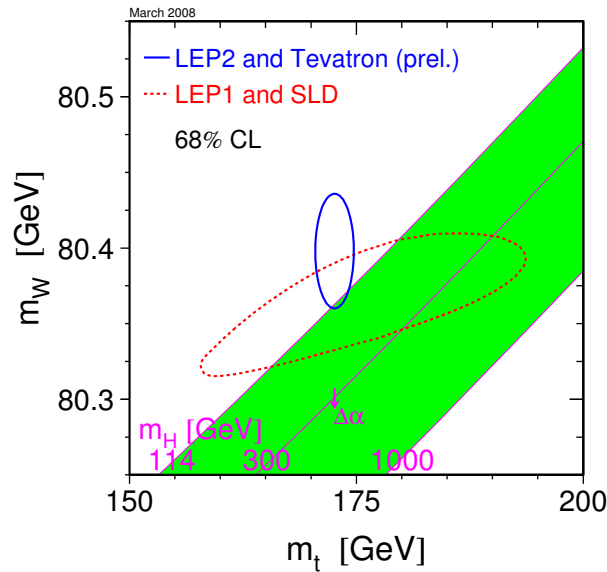


Figure 2.1.: W boson mass vs. top quark mass with lines of constant Higgs masses. The solid line shows the measurements by LEP2 and preliminary results from the Tevatron experiments, whereas the dashed line marks electroweak precision measurements made by LEP1 and SLD (both at 68% CL) [12, 13].

³This value results from an assumed top quark mass width of $\Gamma_{top} = 1.55$ GeV [4].

2.2.1. Top Quark Production via Strong Interaction

The top quark is mainly produced in $t\bar{t}$ -pairs via the strong interaction. Two production processes exist in Leading Order (LO): gluon-gluon-fusion (gg -fusion) and quark-antiquark-annihilation ($q\bar{q}$ -annihilation). Feynman diagrams of these processes are depicted in Figure 2.2.

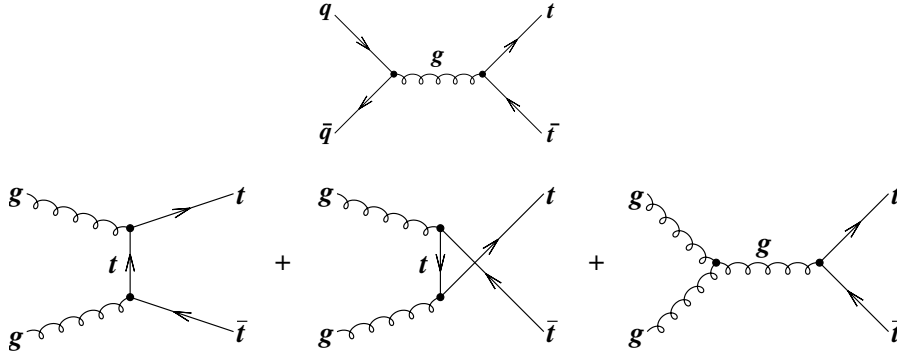


Figure 2.2.: LO Feynman diagrams of the strong $t\bar{t}$ production. Top: quark-antiquark annihilation. Bottom: gluon-gluon fusion. At the LHC the ratio of gg -fusion and $q\bar{q}$ -annihilation is approximately 85%/15% at a centre-of-mass energy of about $\sqrt{s} = 14$ TeV.

At a centre-of-mass energy of about $\sqrt{s} = 14$ TeV gg -fusion dominates with approximately 85% whereas the $q\bar{q}$ -annihilation contributes only 15% (at the Tevatron the ratio is roughly reversed). The ratio depends on \sqrt{s} which can be explained with the parton model (Figure 2.3).

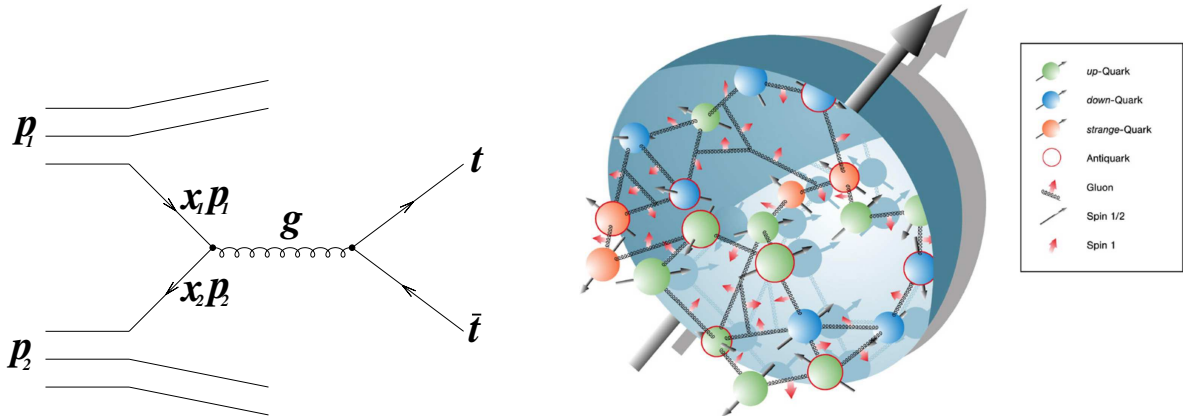


Figure 2.3.: Left: LO Feynman diagram of a scattering process of two partons coming from different protons, releasing a $t\bar{t}$ pair. Right: illustration of one proton with its partons. The spin of the quarks (spin 1/2) and gluons (spin 1) are marked with arrows.

Let p_1 and p_2 be the four-momenta of two incoming protons with a squared centre-of-mass energy of

$$s = (p_1 + p_2)^2 \approx 2 \cdot p_1 p_2, \quad (2.1)$$

where the mass of the proton is neglected. According to the parton model, a collision of two protons means that (at least) two partons – one from each proton – interact. They carry fractions x_1 and x_2 of the four-momentum of the proton.

Thus the centre-of-mass energy of this colliding parton system $\sqrt{\hat{s}}$ is given by

$$\hat{s} = (x_1 p_1 + x_2 p_2)^2 \approx 2 \cdot x_1 x_2 p_1 p_2. \quad (2.2)$$

The expectation value of the two fractions x_1 and x_2 is the same. Lets assume $x_1 \approx x_2 =: x$. A $t\bar{t}$ -pair can be produced if

$$\sqrt{\hat{s}} \geq 2m_t, \quad (2.3)$$

with m_t being the top quark mass. It follows

$$\hat{s} = 2 \cdot x_1 x_2 p_1 p_2 \approx x^2 \cdot 2 \cdot p_1 p_2 = x^2 \cdot s \stackrel{!}{\geq} 4m_t^2 \quad (2.4)$$

$$\Rightarrow x \approx \frac{2m_t}{\sqrt{s}} \quad (\text{at threshold}). \quad (2.5)$$

Assuming a top quark mass of $175 \text{ GeV}/c^2$, Equation (2.5) yields $x \approx 0.025$ at $\sqrt{s} = 14 \text{ TeV}$ for the LHC. For the Tevatron the equation yields $x \approx 0.18$ with $\sqrt{s} = 1.96 \text{ TeV}$.

Parton Distribution Functions (PDFs) describe the probability $xf(x)dx$ of a parton to have a certain fraction of the proton momentum between x and $x+dx$ as a function of x (Figure 2.4). It increases with decreasing x . Thus, at higher centre-of-mass energies more partons fulfill Equation (2.3). The PDFs for quarks and gluons are not identical. For smaller x the PDF for gluons increases stronger than the PDF for quarks. Consequently, for an increasing centre-of-mass energy more and more gluons fulfill Equation (2.3) compared to the quarks. This shifts the ratio of the production processes.

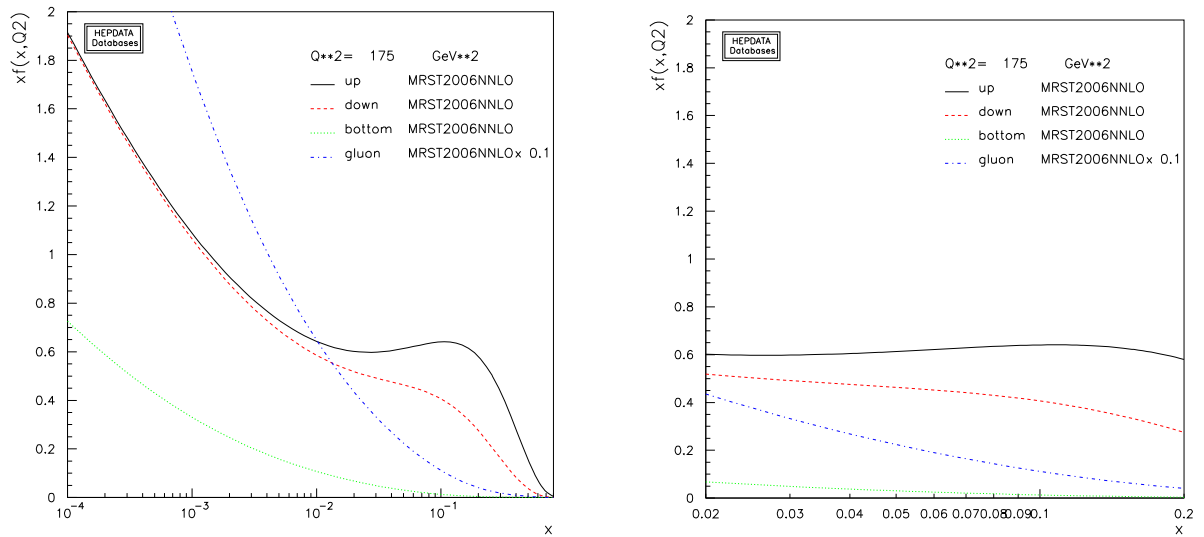


Figure 2.4.: Parton distribution functions for the up quark (black solid line), down quark (red dashed line), bottom quark (green dotted line) and gluon (blue dotted line) at $Q^2 = 175 \text{ GeV}/c^2$. The gluon function is divided by a factor of 10. Left: momentum fraction region $0.0001 < x < 0.8$. Right: momentum fraction region $0.02 < x < 0.2$. The plots are created with the MRST2006NNLO generator [14, 15].

The total cross section for the $t\bar{t}$ -production has been measured at CDF [16] and DØ [17]:

$$\begin{aligned} \sigma_{t\bar{t}} &= 7.3 \pm 0.5 \text{ (stat)} \pm 0.6 \text{ (syst)} \pm 0.4 \text{ (lumi)} \text{ pb} && \text{CDF Run II } (\sqrt{s} = 1.96 \text{ TeV}), \\ \sigma_{t\bar{t}} &= 7.42 \pm 0.53 \text{ (stat)} \pm 0.46 \text{ (syst)} \pm 0.45 \text{ (lumi)} \text{ pb} && \text{DØ Run II } (\sqrt{s} = 1.96 \text{ TeV}). \end{aligned}$$

For $D\bar{O}$ the $l + jets$ channel is quoted from results of March 2008 at a luminosity of 910 pb^{-1} and for CDF the combined result until April 2008 at a luminosity of 760 pb^{-1} is taken. At the LHC the expected total cross section is about [18]

$$\sigma_{t\bar{t}} = 833_{-39}^{+52} \text{ pb} \quad \text{LHC } (\sqrt{s} = 14 \text{ TeV}), \quad (2.6)$$

where this value originates from a Next-to-Leading Order (NLO) + Next-to-Leading Logarithmic (NLL) accuracy calculation with only scale uncertainty.

2.2.2. Top Quark Production via the Electroweak Interaction

Top quarks can also be produced by the electroweak interaction. Within such an event, a single top quark is released. Figure 2.5 shows the LO Feynman diagrams of the weak production processes.

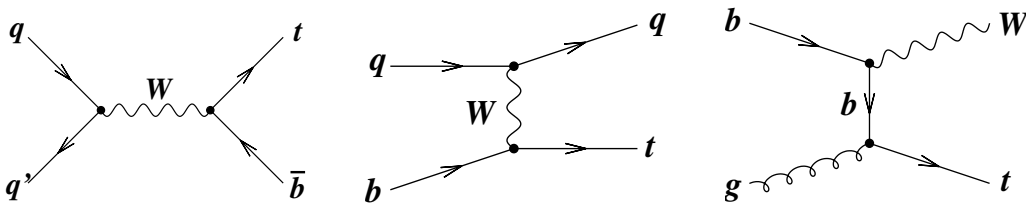


Figure 2.5.: LO Feynman diagrams for single top quark production via the electroweak force. Left: s-channel. Middle: t-channel. Right: Wt associated production.

The cross section of single top quark production has been calculated in NLO [18] for the LHC setting

$$\text{t - channel :} \quad \sigma_{t\bar{t}} = 246_{-12.2}^{+11.8} \text{ pb} \quad (\sqrt{s} = 14 \text{ TeV}), \quad (2.7)$$

$$\text{s - channel :} \quad \sigma_{t\bar{t}} = 10.65_{-1.02}^{+1.12} \text{ pb} \quad (\sqrt{s} = 14 \text{ TeV}). \quad (2.8)$$

Although the cross section is expected to be of the same order of magnitude as the cross section of the strong top production, single top quark events are very hard to detect. Their signature is very similar to that of other processes (the semi-leptonic decay channel of a $t\bar{t}$ -pair for instance) and thus it is difficult to separate these events from the background. Evidence for the single top quark production was recently found at the Tevatron [19–22]. The value of the cross section for the combined results of the $l + jet$ channel of CDF (March 2008, [21]) and of $D\bar{O}$ (March 2008, [22]) are:

$$\sigma_{t\bar{t}} = 4.7 \pm 1.3 \text{ pb} \quad D\bar{O} \text{ Run II } (\sqrt{s} = 1.96 \text{ TeV}),$$

$$\sigma_{t\bar{t}} = 2.2 \pm 0.7 \text{ pb} \quad \text{CDF Run II } (\sqrt{s} = 1.96 \text{ TeV}).$$

Measuring the single top quark production cross section also means to be sensitive to the CKM-mixing-matrix element $|V_{tb}|$. So far, it could only be calculated indirectly by the assumption of a unitary CKM-matrix and by using the elements $|V_{ts}|$ and $|V_{td}|$.

2.2.3. Top Quark Decay

The top quark decays mostly into a W boson and a b quark. This is because $|V_{tb}|^2 \approx 1$ which gives a measure for the coupling of the t - with the b -flavour. The branching ratio is calculated to be $BR(t \rightarrow Wb) > 0.998$.

Top quarks can not be measured directly but only via their decay products. The signature of a $t\bar{t}$ events depends on the decay channel of the involved W bosons. The W boson can decay into a pair of quarks or into a charged lepton and its corresponding (anti-)neutrino. The branching ratios of the W boson are summarised in Table 2.3. There are three decay channels

Table 2.3.: Branching ratios of the W boson decay [6].

Process	Branching ratio
$W \rightarrow e\nu_e$	$(10.75 \pm 0.13)\%$
$W \rightarrow \mu\nu_\mu$	$(10.57 \pm 0.15)\%$
$W \rightarrow \tau\nu_\tau$	$(11.25 \pm 0.20)\%$
$W \rightarrow \text{hadrons}$	$(67.60 \pm 0.27)\%$

for a $t\bar{t}$ event: the *di-leptonic* channel (both W bosons decay leptonically), the *semi-leptonic* channel (one W decays leptonically, one hadronically) and the *full-hadronic* channel (both W bosons decay hadronically). Figure 2.6 (left) shows a pie chart of the branching ratios in LO. The studies presented in this thesis are based on the semi-leptonic decay channel (Figure 2.6, right).

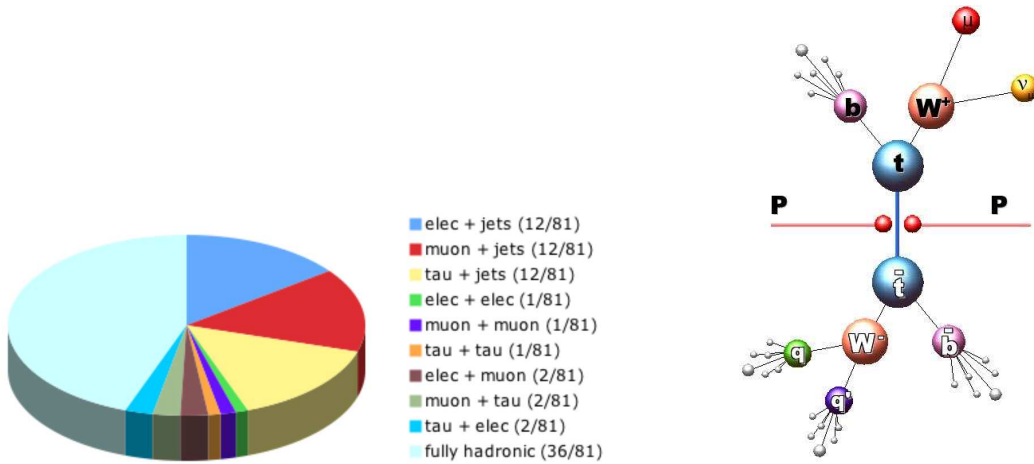


Figure 2.6.: Left: pie chart of the branching ratios of the $t\bar{t}$ -decay. The fractions come from theoretical predictions. Right: illustration of the semi-leptonic decay of a $t\bar{t}$ -system.

The branching ratio of a specific lepton flavour can be calculated as:

$$\begin{aligned} BR(t\bar{t} \rightarrow l + jets) &= BR(t\bar{t} \rightarrow W^+W^-b\bar{b} \rightarrow q\bar{q}'b\bar{b}l\nu_l) \\ &= [BR(t \rightarrow Wb)]^2 \cdot 2 \cdot BR(W \rightarrow q\bar{q}') \cdot BR(W \rightarrow l\nu_l). \end{aligned}$$

Including the values for the different leptons of Table 2.3 this yields

$$\begin{aligned} BR(t\bar{t} \rightarrow e + jets) &= (14.48 \pm 0.23)\%, \\ BR(t\bar{t} \rightarrow \mu + jets) &= (14.23 \pm 0.26)\%, \\ BR(t\bar{t} \rightarrow \tau + jets) &= (15.15 \pm 0.33)\%. \end{aligned}$$

Due to *confinement* a single quark hadronizes and develops a jet of particles which can be measured in a detector. Consequently, the signature of the semi-leptonic decay of a $t\bar{t}$ system results in four jets – two light quark jets and two b quark jets – and one lepton. Since neutrinos almost never interact with matter, they cannot be detected and contribute to the missing transverse energy. For the reconstruction of the kinematics the semi-leptonic channel has the advantage that only one neutrino is emitted (not two as in the case in the di-leptonic channel) and that the jet combinatorics is easier than in the full-hadronic case (four jets instead of six).

2.2.4. Background Processes

A background process is a physics process which leads to the same signature in a detector as the signal process. For the semi-leptonic decay of a $t\bar{t}$ system there are mainly two background processes, as measurements at the Tevatron have confirmed: QCD-processes, meaning multijet events, and W +jets events.

In multijet events a jet can be misidentified as an electron. In order to misidentify a muon for a hadron, the hadron must reach the outer muon chambers which is of low probability. However, b quarks release muons and it is possible that the isolation criteria for the muon is fulfilled, although the muon is actually part of a jet. Furthermore, missing transverse energy (MET) can be faked by inefficiencies of the calorimeter or neutrinos coming from weakly decaying quarks (in particular from b quarks).

Another source of background for $t\bar{t}$ events is W boson production. If the W boson decays leptonically and additional jets are found in the event (e.g. from initial state radiation), the final state resembles the semi-leptonic $t\bar{t}$ -decay.

LO Feynman diagrams for $W + 1 \text{ jet}$ and $W + 2 \text{ jets}$ are sketched in Figure 2.7 and 2.8 respectively.

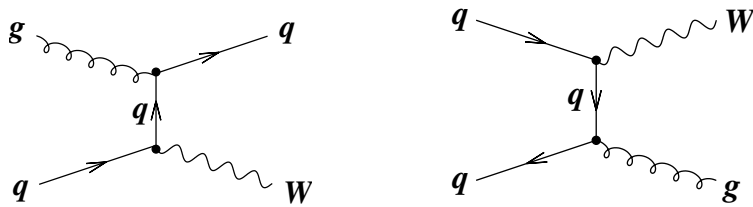


Figure 2.7.: LO Feynman diagrams of $W + 1 \text{ jet}$ production.

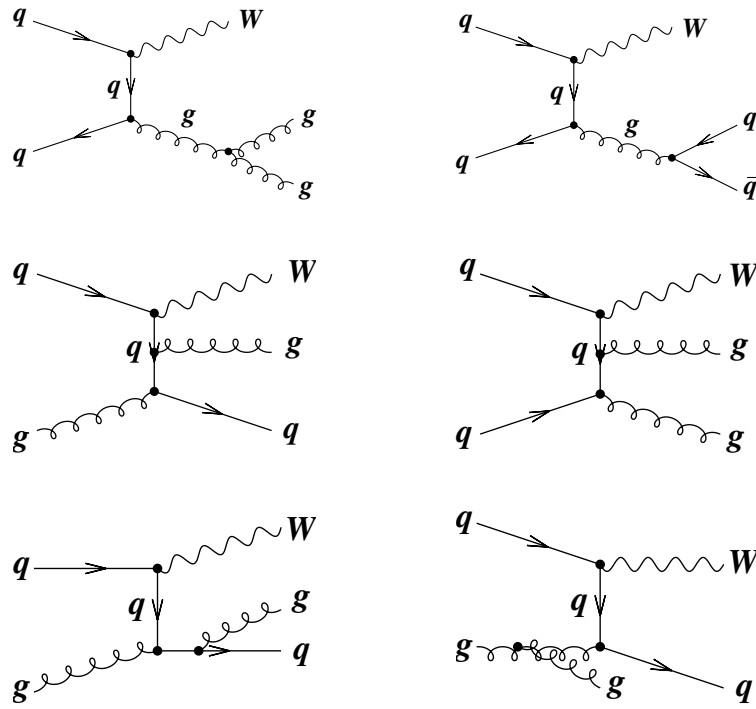


Figure 2.8.: LO Feynman diagrams of $W + 2$ jets production.

3. Experimental Setup

In the studies presented in this thesis the kinematic fit is applied to simulated data. These come from MC simulations of the ATLAS (A Toroidal LHC ApparatuS) experiment. ATLAS is a general-purpose detector which is scheduled to start operations in mid-2008. It is one of six particle detectors at the Large Hadron Collider (LHC). The LHC is about to start up within the year 2008. It will run at a nominal centre-of-mass energy of 14 TeV at an aimed luminosity of $10^{34} \text{ cm}^{-2}\text{s}^{-1}$. An upgrade is planned for around 2015 leading to an intended luminosity of $2 \cdot 10^{35} \text{ cm}^{-2}\text{s}^{-1}$ [23]. In the following, the LHC and the ATLAS experiment are introduced. The presented studies rely on the calorimeter performance. The calorimeter is thus described more precisely.

The following right-handed coordinate system is used: the z -axis is defined by the beam direction, the positive x -axis points from the interaction point to the centre of the LHC, whereas the positive y -axis points upwards. The transverse momentum is defined in the x - y -plane as

$$p_T := \sqrt{p_x^2 + p_y^2} \quad (3.1)$$

and the missing transverse energy is denoted as E_T^{miss} , respectively. ϕ is defined as the azimuthal angle measured around the beam axis with θ being the polar angle from the beam axis. For relativistic energies it is useful to define the pseudo-rapidity¹

$$\eta := -\ln\left(\tan\frac{\theta}{2}\right). \quad (3.2)$$

Furthermore, the distance ΔR in the η - ϕ -plane is defined as

$$\Delta R := \sqrt{\Delta\eta^2 + \Delta\phi^2}. \quad (3.3)$$

3.1. The Large Hadron Collider

The LHC [24–26] is a ring-shaped proton-proton accelerator with a circumference of 27 km. It is installed in a tunnel of 3.8 m diameter, 45 m to 170 m below ground at the CERN Laboratory (European Organization for Nuclear Research), Geneva, Switzerland (Figure 3.1). Two beams of protons are injected from the Super Proton Synchrotron (SPS) at 450 GeV. They travel in opposite directions in separate beam pipes at an ultrahigh vacuum of 10^{-10} mbar. The acceleration of the particles is induced by Radio Frequency (RF) cavities which are located intermittently along the beam pipe. Passing the electric field of a RF cavity, some of its energy is transferred to the particles. 1,232 dipole magnets made of niobium-titanium of 15 m length each and with magnetic fields of about 8.4 T, bend the beam around the ring. The focusing of the beam is realised by 392 quadrupole magnets of 5 m to 7 m length.

¹Pseudo-rapidity differences are invariant under Lorentz- transformations

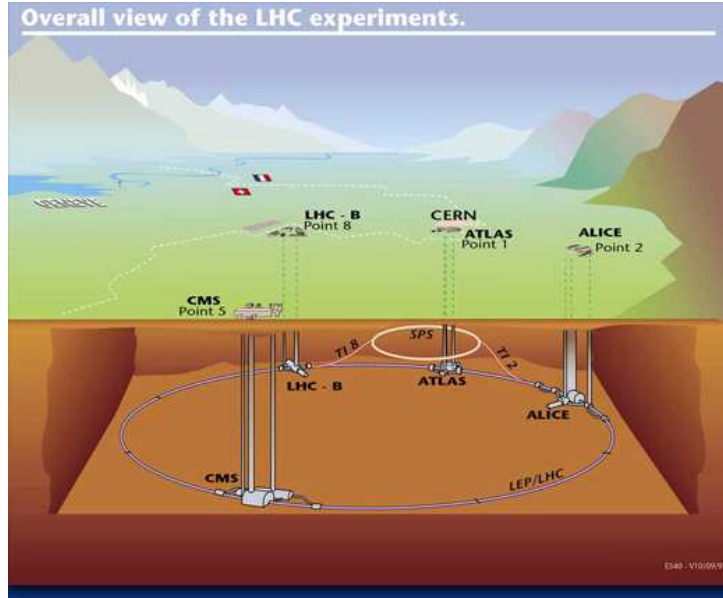


Figure 3.1.: Principle view of the LHC below ground near Geneva, Switzerland. The largest four experiments are labeled. Lake Geneva and the Jura Mountains can be recognized as well as the border between France and Switzerland.

The strong magnetic fields can only be generated by coils operating in a superconducting state. Therefore, a cooling of the magnets down to 1.9 K is required which is realised by a distribution system of liquid helium. The refrigeration power of the cryogenic system is larger than 140 kW. Each beam contains accelerated protons with an energy of 7 TeV which will be stored for 10 to 20 hours. There are 2808 well-defined bunches of $1.1 \cdot 10^{11}$ protons. Every 25 ns a bunch crossing occurs, each causing 19 collisions in an event on average (at a luminosity of $10^{34} \text{ cm}^{-2}\text{s}^{-1}$) such that 760 billion collisions are expected in one second. The total proton-proton cross section at 7 TeV per beam is approximately 100 mb (inelastic: 60 mb, elastic 40 mb) [24]. The size of the bunches varies along the ring. They get squeezed in the x - y -direction to about $16 \mu\text{m}$ at the interaction point in order to increase the probability of an interaction.

At the LHC, there are four different interaction points where four experiments are built: ATLAS with LHCf, CMS with TOTEM, ALICE and LHCb. In the following these experiments are briefly introduced.

ATLAS – A Toroidal LHC ApparatuS

ATLAS is a general-purpose detector. It will be discussed in the next section in more detail.

CMS – Compact Muon Solenoid

The CMS [27, 28] detector is the second general-purpose experiment of the LHC. Its design is dominated by a huge superconducting solenoid. It has the shape of a cylindrical coil made of superconducting cable that will generate a magnetic field of about 4 T. A tracking system, a massive scintillating crystal electromagnetic calorimeter and a sampling calorimeter for hadron detection are placed inside the magnet. CMS has a size of 21 m in length and about 16 m in diameter. With a weight of 12,500 tons it is relatively *compact* compared to the ATLAS experiment.

ALICE – A Large Ion Collider Experiment

ALICE [29] is a special-purpose experiment, built for studying heavy-ion collisions in which a quark-gluon plasma is produced. Therefore, lead-ions are injected into the LHC which will collide at a centre-of-mass energy of 5.5 TeV. The quark-gluon plasma resembles the state of the universe shortly after the Big Bang where the gluons and quarks were not confined.

LHCb Large Hadron Collider beauty experiment

The focus of LHCb [30] is the measurement of the interaction of b -hadrons for determining the parameters of the Charge Parity (CP) violation. The detector consists of a series of subdetectors for detecting mainly particles radiated in forward direction. Therefore, it forms a single arm forward spectrometer of 20 m length.

LHCf – Large Hadron Collider forward experiment

LHCf [31] is a special-purpose experiment and affiliated to ATLAS. Particles in the very forward region in hadronic interactions will be measured. Therefore, it consists of two detectors, 140 m on both sides of an interaction point. At LHCf highly energetic collisions and cascades will be investigated similar to particle showers of the earth's atmosphere. Investigating these events will help scientists to interpret and calibrate large-scale cosmic-ray experiments.

TOTEM – TOTal cross section and Elastic scattering Measurement experiment

TOTEM [32] is affiliated to CMS. Its purpose is to measure the effective total proton-proton cross section with an absolute error of 1 mb by using a luminosity independent method. Furthermore, elastic scattering and hard diffractive dissociation processes will be studied. Particles which are very close to the LHC beam will be measured using *Roman pots* [33].

3.2. The ATLAS Detector

The ATLAS detector [34] is one of two general-purpose detectors at the LHC. It covers the widest possible range of particle signals to ensure sensitivity to new physics. It will search for the Higgs boson, super-symmetric particles, extra dimensions, dark matter and other physics processes. The design of the detector differs considerably from the design of the CMS detector. Different concepts are used to measure the same type of physics, which opens the opportunity to complement the results.

The ATLAS detector is 44 m long, 25 m in diameter and weights about 7,000 tons. It has an onion-like structure of concentric cylinders built around the interaction point (Figure 3.2). Every layer has its own purpose. The detector consists of several sub-systems: the tracking system, calorimeter system, muon system and magnet system. In the following, these systems are discussed in more detail as well as the trigger system and Data Acquisition (DAQ).

3.2.1. Tracking System

The purpose of the tracking system [36–38], or *Inner Detector* (ID), is to measure the tracks and the momentum of charged particles produced in proton-proton collisions. Therefore, their paths are reconstructed from the signals arising from their penetration through the tracking system (Figure 3.3, left). The ID is a combination of the pixel detector, the Semi-Conductor Tracker (SCT) and the Transition Radiation Tracker (TRT) (Figure 3.3, right).

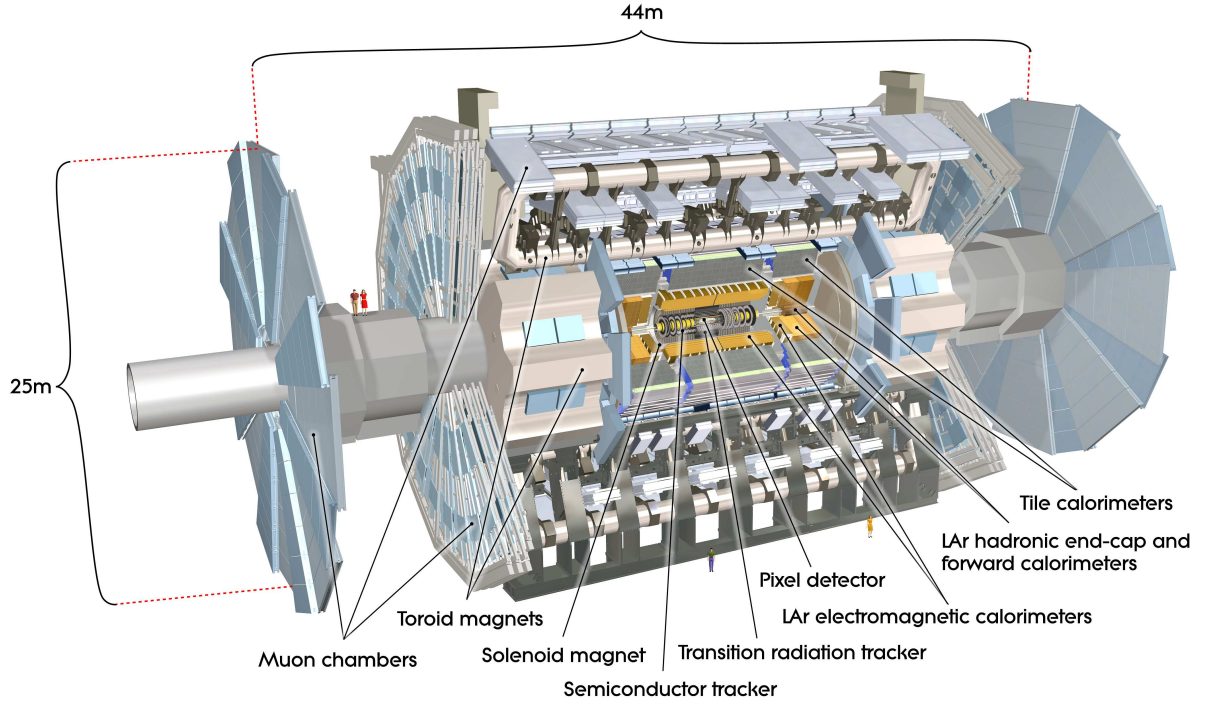


Figure 3.2.: Sliced 3D view of the ATLAS detector. The individual components are labeled. To illustrate the size of the detector a few humans are sketched for comparative reasons [35].

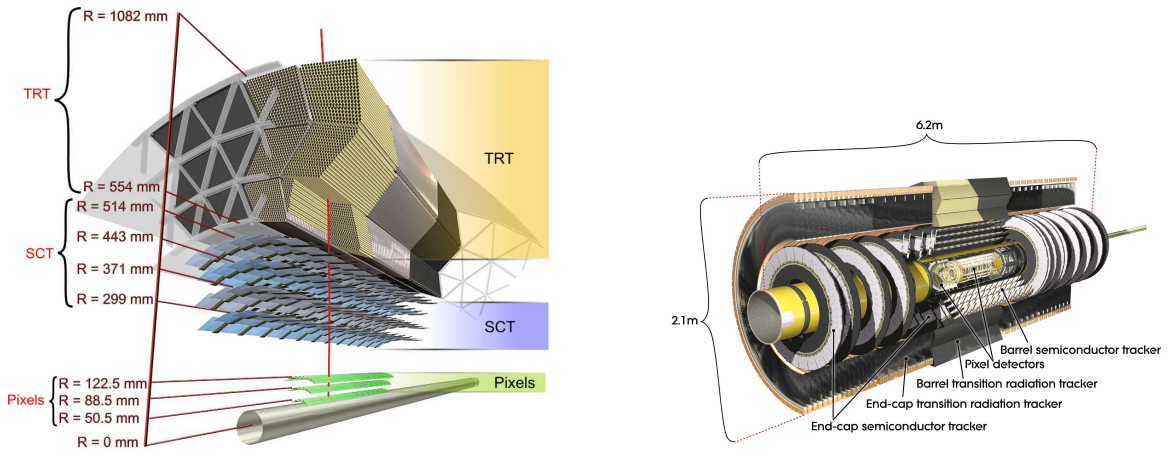


Figure 3.3.: Left: sketch of the elements of the tracking system in the barrel region. It is traversed by a charged track of $p_T = 10$ GeV. The track passes the beryllium beam-pipe, the three silicon-pixel layers, the four cylindrical double layers of the SCT, and on average 36 axial straw tubes of the TRT. Right: cut-away view of the ATLAS inner detector. The pixel detector is located in the innermost region (yellow) enveloped by the SCT with its end-cap disks. The TRT forms the outermost part of the tracker system [35].

This configuration has been chosen to achieve a high momentum and vertex resolution: at smaller radii the high granularity of the pixel detector ensures a good spatial resolution, while for larger radii the TRT contributes with a large number of hit points to the track reconstruction.

The first two components are based on the ionization of silicon when a charged particle passes through. The TRT, however, uses the phenomenon of the transition radiation which occurs when a charged particle passes materials with different dielectric constants. Approximately 1,000 particles will be produced every 25 ns within $|\eta| < 2.5$ and penetrate the detector leading to a high track density. On the one hand the tracking components must thus be radiation hard, especially at small radii. On the other hand they must not influence the particle track.

The ID is located in a magnetic field of 2 T generated by the central solenoid. It extends over a length of 6.2 m with a diameter of 2.1 m. The pixel detector and the SCT cover a region of $|\eta| < 2.5$ and the TRT of $|\eta| < 2.0$, respectively. In the barrel region the ID is arranged around the beam axis in concentric cylinders. In the end-cap regions disks are located perpendicular to the beam axis.

In the following, the performance of the ID, the pixel detector, the SCT and the TRT are discussed in more detail.

Performance

A good pattern recognition and high precision in both R - ϕ and z coordinates is achieved by the combination of high precision trackers at small radii with the TRT at a larger radius. In general the relative momentum resolution for the transverse momentum p_T of a tracking system is given by

$$\frac{\sigma_{p_T}}{p_T} = \frac{\sigma_x \cdot p_T [\text{GeV}]}{0.3 \cdot l^2 \cdot B [\text{T}]} \sqrt{\frac{720}{N+4}}, \quad (3.4)$$

where B is the magnetic field, σ_x the spacial resolution, l the length of the track and N the number of track points. Charged particles are bent within the ID due to the magnetic field of the solenoid. The bending radius r in a magnetic field B is given by:

$$r [\text{m}] = \frac{p_T [\text{GeV}/c]}{0.3 \cdot B [\text{T}]} \quad (3.5)$$

Pixel Detector

Since the pixel detector is the innermost component of the ID, it has the highest granularity compared to the other tracking components. It consists of 1,744 identical silicon pixel modules with a minimum pixel size of $50 \times 400 \mu\text{m}$. They are arranged in three barrel layers and two end-caps each with three disk layers. To avoid holes between single modules, they are built in tile-like shingled arrays, leading to small overlap regions between them. Each module has 47,232 pixels with 46,090 readout channels. The pixel detector has approximately 80.4 million readout channels in total. In the barrel region the intrinsic spatial resolution are $10 \mu\text{m}$ in R - ϕ -direction and $115 \mu\text{m}$ in z -direction while in the disks they are $10 \mu\text{m}$ in R - ϕ -direction and $115 \mu\text{m}$ in R -direction.

SCT – Semi-Conductor Tracker

The SCT consists of four cylindrical double strip layers. The strips are parallel to the beam axis. In the barrel region, half of them have a small stereo angle of 40 mrad for measuring both R and ϕ coordinate. The SCT consists of 15,912 strip sensors of 6.4 cm length with a pitch of $80 \mu\text{m}$ in the barrel region. There are nine disks on each side with one set of strips radially arranged and another set of strips at an angle of 40 mrad in the end-cap region. The total number of readout channels in the SCT is approximately 6.3 million. Both the barrel and the disks have an intrinsic resolution of $17 \mu\text{m}$ (R - ϕ -direction) and $580 \mu\text{m}$ (z -direction) for a single module.

TRT – Transition Radiation Tracker

The TRT consists of 4 mm diameter straw tubes filled with a Xe/CO₂/O₂ gas mixture. This gas is ionized by penetrating particles as well as by photons coming from the transition radiation of these particles. A gold wire in the centre of the tubes measures the electric pulse, coming from the ionization. The intensity of the transition radiation depends on the type of the particle which allows to distinguish between them. In the barrel region the straw tubes are arranged parallel to the beam axis. At about $\eta = 0$ the wires are divided into two halves of 67 cm length each. The total number of TRT readout channels is approximately 351,000. The intrinsic resolution per straw tube is about 130 μm in the barrel. In the end-cap region the straw tubes are arranged radially in wheels and have a length of 37 cm. Although the granularity of the TRT is not as high as for the pixel detector, it contributes significantly to the momentum measurement due to the large number of hits per track (typically 36) and because it is located at larger radii than the pixel detector.

3.2.2. Calorimeter System

The purpose of the calorimeter system is to measure the energy of particles from their interaction with the material of the calorimeter [39–42]. Electrons and photons are stopped in the electromagnetic calorimeter, hadrons in the hadronic calorimeter. Muons deposit a very small fraction of their energy in the calorimeter and penetrate the whole detector including the muon chambers. Neutrinos hardly ever interact with matter and cannot be measured with the ATLAS detector.

The calorimeter system consists of four parts: the Liquid Argon Electromagnetic Calorimeter (LAr EM Cal), the Hadronic Tile Calorimeter (HTC), The Hadronic Liquid Argon End-cap Calorimeter (LAr HEC Cal) and the Liquid Argon Forward Calorimeter (LAr FCal). Altogether they cover a range of $|\eta| < 4.9$. A cut-away view of the calorimeter system is given in Figure 3.4. The granularity of the EM Cal is much finer than that of other components because the signals of electromagnetic particles are more collimated compared to hadronic jets and because the LAr EM Cal is closer to the interaction point.

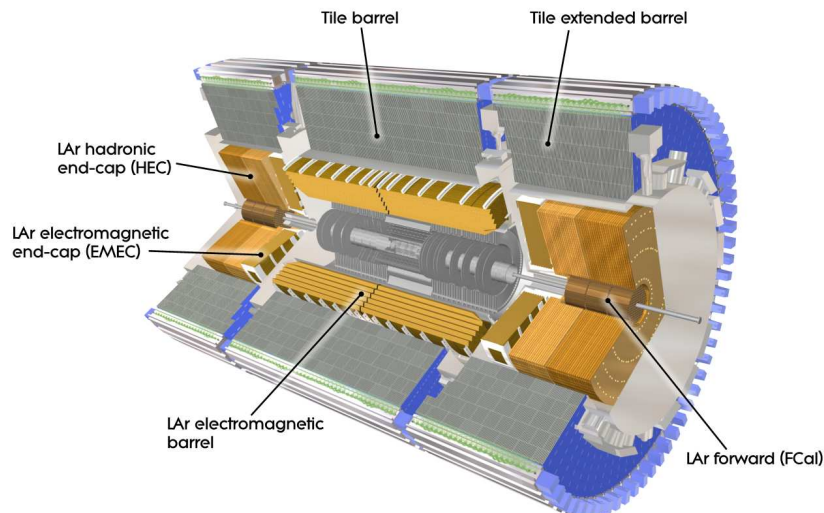


Figure 3.4.: Cut-away view of the ATLAS calorimeter system. It envelopes the tracking system. The components of the calorimeter are labeled. [35].

A high precision of the energy resolution, a good containment for electromagnetic and hadronic showers and the limitation of a punch-through into the muon system are important properties of a calorimeter. Therefore, the depth of the calorimeter is an important criterion. The radiation length X_0 is defined as the thickness in which the energy of a particle shower is reduced to $1/e$ of its original energy on average. For electrons the LAr EM Cal has a radiation length of $X_0 > 22$ in the barrel region and $X_0 > 24$ in the end-cap region. The interaction length λ is defined as the mean free path of a particle before interacting with matter. For hadrons, the approximate interaction length of the hadronic calorimeter is $\lambda \approx 9.7$ for the barrel and $\lambda \approx 10$ for the end-caps. Both the large η coverage and the thickness of the calorimeter are important for the measurement of E_T^{miss} , which is of crucial relevance for many physics signatures, especially SUSY particle searches.

In the following, the components of the calorimeter are introduced in more detail and the calorimeter energy resolution and the jet energy scale are discussed.

LAr EM Cal – Liquid Argon Electromagnetic Calorimeter

The LAr EM Cal is the innermost component of the calorimeter system. It consists of two parts: the barrel part which covers a range of $|\eta| < 1.475$ and an end-cap part covering $1.375 < |\eta| < 3.2$. A presampler detector is installed to correct for energy lost by electrons and photons upstream of the calorimeter in a range of $|\eta| < 1.8$. The barrel calorimeter is built of two identical half-barrels which are separated by a 4 mm gap. It is segmented into three sections in the longitudinal direction.

The end-caps are divided into two wheels, the inner one covering a range of $1.373 < |\eta| < 2.5$ and the outer one $2.5 < |\eta| < 3.2$, respectively. The end-cap inner wheel is segmented into two longitudinal sections which have a coarser lateral granularity than the rest of the calorimeter.

The shape of the EM calorimeter has an accordion-like geometry in order to provide a complete ϕ symmetry without azimuthal cracks. The scintillating material is the liquid argon. Lead plates are assembled over the whole coverage of the LAr calorimeter as absorber material. Their thickness has been optimized as a function of η by means of calorimeter performance in energy resolution. The LAr EM Cal contains a LAr layer with a thickness of 1.1 cm (0.5 cm) in the barrel (end-cap) region. Particle showers in the argon liberate electrons that are collected and recorded.

Both the barrel and the end-caps have their own cryostat. The cryostats are needed to ensure that the argon stays liquid at a temperature of about 85 K. The LAr calorimeter and the central solenoid share a common vacuum vessel, eliminating two vacuum walls.

HEC Cal – Hadronic LAr End-cap Calorimeter

The HEC Cal consists of two independent wheels per end-cap. It is located directly behind the end-caps of the LAr EM Cal. There is an overlap between the HEC and the forward calorimeter at around $3.1 < |\eta| < 3.2$ in order to prevent the drop in material density at the transition between them. Likewise, the HEC overlaps with the tile calorimeter in the region of $1.5 < |\eta| < 1.7$. Each wheel contains 32 identical wedge-shaped modules and is divided into two longitudinal segments. In total there are four layers per end-cap. The wheels are made of parallel copper plates. The innermost has a thickness of 25 mm and those further away have a thickness of 50 mm.

LAr FCal – Liquid Argon Forward Calorimeter

The FCal is integrated into the end-cap cryostats. Thus the uniformity of the coverage and a reduced radiation background level in the muon spectrometer is preserved. It consists of three modules in each end-cap. The first one is made of copper and optimised for electromagnetic measurements. The other two are made of tungsten and will be used predominantly to measure the energy of hadronic showers. Each module consists of a metal matrix. There are regularly spaced longitudinal channels filled with an electrode structure which consists of rods and tubes. The LAr in the gap between the rod and the tube is the sensitive medium.

The FCal is approximately ten interaction lengths deep. It is recessed by about 1.2 m with respect to the LAr EM Cal front face. This is due to the reduction of diffusely reflected neutrons (albedo) in the inner detector cavity.

HTC – Hadronic Tile Calorimeter

The HTC consists of one barrel in the centre region of $|\eta| < 1.0$ and two extended barrels which cover $0.8 < |\eta| < 1.7$. It is located directly outside the EM calorimeter envelope at an inner radius of 2.28 m and an outer radius of 4.25 m. The barrel and extended barrels are divided azimuthally into 64 modules and longitudinally into three layers of 1.5, 4.1 and 1.8 interaction lengths.

Steel is used as absorber material whereas the scintillating tiles build the active material. The scintillating tiles are read out by wavelength shifting fibers on each side, which go into two separate photomultiplier tubes.

Energy Resolution

The intrinsic energy resolution of a calorimeter follows from Poisson statistics: the number of ionized particles N is proportional to the deposited energy E . The error σ_N for the counted particles N follows from Poisson statistics $\sigma_N = \sqrt{N}$. This leads to the intrinsic energy resolution of

$$\frac{\sigma_E^{intr}}{E} \propto \frac{\sigma_N}{N} = \frac{1}{\sqrt{N}} = \frac{a}{\sqrt{E}}, \quad (3.6)$$

where a is a detector specific proportionality factor for the relative energy resolution, the *sampling term*. Solving Equation (3.6) for the sampling term, yields a (*quasi-*)*relative energy resolution* which is of relevance for later studies

$$a = \frac{\sigma_E^{intr}}{\sqrt{E^{true}}} = \frac{(E' - E^{true})}{\sqrt{E^{true}}}, \quad (3.7)$$

with E^{true} being the true energy value which is known from the simulation of the events and E' being the measured energy value. For the measurement of electrons via the LAr EM Cal the relative energy resolution is close to $10\%/\sqrt{E} [\text{GeV}]$ and for the measuring of pions via the hadronic Cal $50\%/\sqrt{E} [\text{GeV}]$, respectively [43].

However, considering calibration effects a *local constant term* c must be added to the energy resolution as well as a term proportional to $\frac{1}{E}$ which takes instrumental effects into account. The energy resolution of a calorimeter is thus given by

$$\frac{\sigma_E}{E} = \sqrt{\frac{a^2}{E} + \frac{b^2}{E^2} + c^2} =: \frac{a}{\sqrt{E}} \oplus \frac{b}{E} \oplus c. \quad (3.8)$$

JES – Jet Energy Scale

The JES of a calorimeter defines the correspondence between the energy of a particle and a measured signal E' . Due to instrumental noise, large fluctuations in particle showering or non-linear response of the calorimeter (especially for hadrons) for instance, the JES must be estimated for every detector. A corrected energy E^{calib} can be calculated from a measured Energy E' using the relation

$$E^{calib} = \frac{E' - E_0}{R_{jet} \cdot S}, \quad (3.9)$$

with E_0 being an offset energy including the instrumental noise for example. R_{jet} represents the calorimeter response to jets which corrects the absolute energy scale and S is the showering correction which corrects for energy emitted outside the jet cone. Investigating the sensitivity of the kinematic fit to the JES in later studies (Section 6.7.2), the absolute energy scale is varied according to

$$E^{calib} = \alpha \cdot E', \quad (3.10)$$

with α being the constant of proportionality.

3.2.3. Muon System

The muon system [44] is the outermost detector component of the ATLAS detector. It surrounds the calorimeter and measures muon tracks and their momentum with a precision of

$$\frac{\sigma_{pT}}{pT} \approx 10\% \quad (\text{at 1 TeV}). \quad (3.11)$$

in a range of $|\eta| < 2.7$. Additionally, it performs the muon triggering within a region of $|\eta| < 2.4$. To achieve these two main requirements different types of muon chambers are used: chambers with a short response time for the triggering and chambers with a higher resolution for the track reconstruction.

In Figure 3.5 the layout of the muon system is shown. In the barrel region three cylindrical muon chamber shells extend from a radius of 4.25 m to approximately 11 m. Each end-cap is formed by three wheels which are perpendicular to the beam axis at distances of approximately 7.4 m, 10.8 m and 14 m to the interaction point. In the centre of the detector (at about $|\eta| < 0.08$) there is a gap in the muon system for services of other detector components (solenoid magnet, calorimeters and inner detector).

There are four different chamber types: Monitored Drift Tubes (MDTs), Cathode Strip Chambers (CSCs), Resistive Plate Chambers (RPCs) and Thin-Gap Chambers (TGCs).

The MDTs consist of three to eight layers of drift tubes which have an average resolution of $80 \mu\text{m}$ per tube yielding a resolution of about $35 \mu\text{m}$ per chamber. The drift tubes are filled with an Ar/CO₂ gas mixture which is ionized by muons passing through. A tungsten-rhenium wire is situated in the centre of each drift tube. The electrons from an ionization process are collected there: Because of a high voltage which is impressed between tube and wire, an electric field causes them to drift towards the wire. By measuring the time which the electrons need to drift to the wires, it is possible to reconstruct muon tracks according to a drift-time-space-relation.

The CSCs are inserted in the forward region ($2 < |\eta| < 2.7$). They are multiwire proportional chambers with a resolution of approximately $5 \mu\text{m}$ per chamber in the transverse plane (x - y -plane) and $40 \mu\text{m}$ in the bending plane (R - z -plane).

RPCs are located in the region $|\eta| < 1.05$, whereas the TGCs in the end-cap cover a region of $1.05 < |\eta| < 2.4$. Both RPCs and TGCs are used to trigger muons.

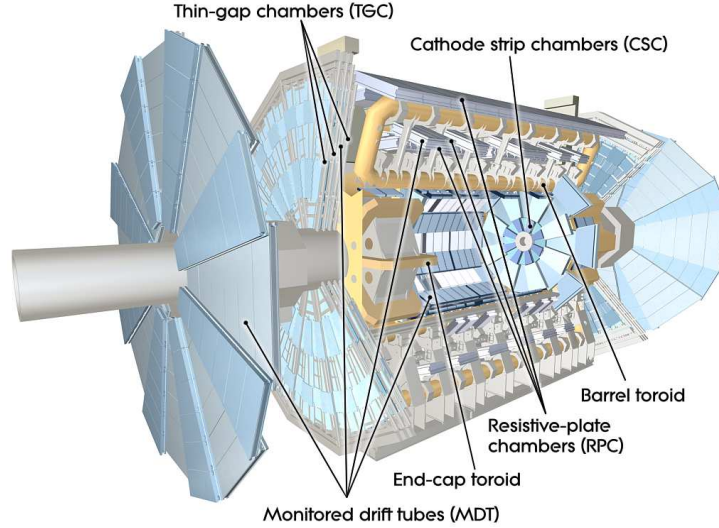


Figure 3.5.: Cut-away view of the muon system of the ATLAS detector. The components are labeled [35].

3.2.4. Magnet System

The magnet system of the ATLAS detector [45–48] consists of two main components: the solenoid magnet and the toroid magnet. Charged particles are bent in the magnetic field. Their momentum and the sign of their charge can be deduced from the curvature of their path (Equation (3.4)). Therefore, the magnet system is essential for the identification and the momentum determination of particles. The solenoid provides the magnetic field for the ID and the toroid for the muon system, respectively.

The bending power P_{bend} can be expressed via the integral $P_{bend} = \int B_{\perp} ds$, where B_{\perp} is the field component perpendicular to the charged particle direction and ds an infinitesimal small path element along the track of the particle.

Solenoid magnet

The ATLAS central solenoid has a length of around 5.3 m and a diameter of 2.4 m. It produces a 2 T axial magnetic field which penetrates the whole ID. The peak magnetic field reaches 2.6 T. Flat superconducting cables in the centre of an aluminium stabilisator are used for the coils. The operating current is approximately 7.7 kA. The total mass of the coils is 5.4 tons and the stored energy is 40 MJ.

Toroid magnet

The ATLAS toroid magnet (Figure 3.6) system consists of one barrel toroid and two end-cap toroids lined up with the central solenoid. One toroid consists of eight large coils which are arranged symmetrically around the beam axis. The end-cap toroid is rotated by 22.5° with respect to the barrel toroid, such that a radial overlap and an optimization of the bending power in the transition region of the two coil systems is ensured. Each barrel coil consists of a Ni/Ti/Cu-alloy and is housed in a cryostat for cooling it down to 4 K making it superconducting. A current of around 21 kA flows through the toroid which is needed to provide the detector with a strong magnetic field of maximally 3.9 T.

The stored energy in the whole central toroid is roughly 1.1 GJ. In the barrel region a bending power of $P_{bend} = 1.5$ Tm up to $P_{bend} = 5.5$ Tm is reached in a pseudo-rapidity range of $|\eta| < 1.4$ and in the end-cap $P_{bend} = 1.0$ Tm to $P_{bend} = 7.5$ Tm in the region of $1.6 < |\eta| < 2.7$.

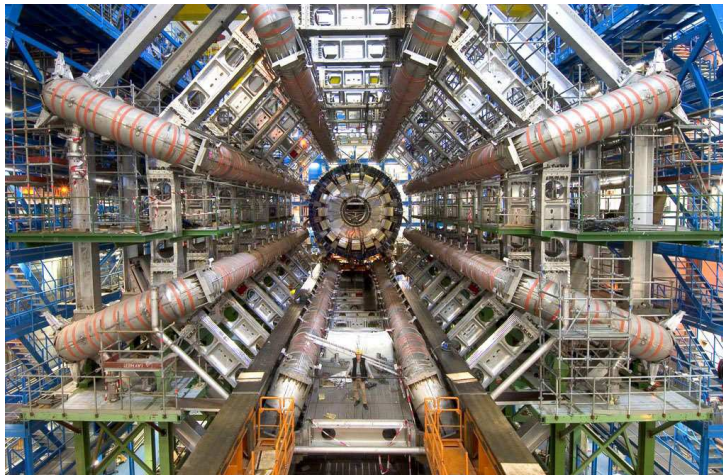


Figure 3.6.: View in the direction of the beam through the ATLAS detector, before the installation of the ID and the calorimeter. The eight huge coils of the Toroid magnet system are arranged in 45° distances. An engineer is standing in front of the detector to demonstrate the size of the detector.

3.2.5. Trigger System and Data Acquisition

The trigger system [49, 50] is needed to reduce the large amount of data which is produced at a particle physics experiment. Events occur with a rate of 40 MHz. The ATLAS experiment will produce about 1.6 MB per event from approximately 10^8 readout channels. Saving all this data is impossible at present. Approximately 60 TB of data would have to be saved per second if no trigger existed at the ATLAS experiment. Therefore, only one in 200,000 events will be selected via the trigger system yielding a saving rate of approximately 300 MB/s. However, it is essential that no interesting physics processes are rejected.

There are three trigger levels: the Level 1 Trigger (L1T), the Level 2 Trigger (L2T) and the Event Filter (EF). The L2T and EF together form the *High Level Trigger* (HLT). The whole trigger system reduces the total data rate from 40 MHz to 200 Hz. The L1T is a hardware based trigger whereas the L2T and the EF are software-based and run on a large computer cluster near the detector.

L1T – Level 1 Trigger

The L1T reduces the data rate from 40 MHz to 100 kHz. Its selection is based on the measurements of a subset of the calorimeter and muon detectors. It searches for high transverse momentum muons, electrons, photons, jets, τ -leptons decaying into hadrons and for large E_T^{miss} . The latency of the L1T is about $2 \mu\text{s}$ until reaching its decision (including propagation delays in the cables). Pipeline memories save the information from the detector. Events that pass the L1T selection are forwarded to the next stages of the detector electronics and thus to the DAQ.

Regions of interest (RoI's) are defined by the L1T in each event, meaning that certain $\eta - \phi$ -regions, where interesting features have been identified within the selection process (e.g. where threshold criteria are fulfilled), are provided to the HLT. Readout buffers store the data for such events. The information remains until the L2 decision is available.

L2T – Level 2 Trigger

The L2T reduces the data rate from 100 kHz to 3.5 kHz. It uses the RoI's provided by the L1T and has an average latency of 40 ms. The L2T exploits the full information of all detectors using processor farms to refine the selection of candidate objects, made by the L1T.

EF – Event Filter

The EF reduces the data rate from 3.5 kHz to approximately 200 Hz. Its latency is roughly 1 s due to event building which happens at this stage. It uses offline analysis procedures on fully-built events for its selection. These procedures turn the signal patterns from the detector into physics objects, e.g. jets, photons or leptons.

DAQ System – Data Acquisition System

The DAQ system manages the data flow and the configuration, control and monitoring of the ATLAS detector during data taking. It receives and buffers event data from the readout electronics at the L1T rate. Each readout buffer contains information of several events for one part of a subdetector. The event builder reassembles this information into a single memory of the EF processor.

The DAQ system saves events which have been selected by the EF to permanent storages. Grid computing will be extensively used for event reconstruction, allowing the use of parallel computer networks.

In Figure 3.7 a functional view of the trigger system is sketched.

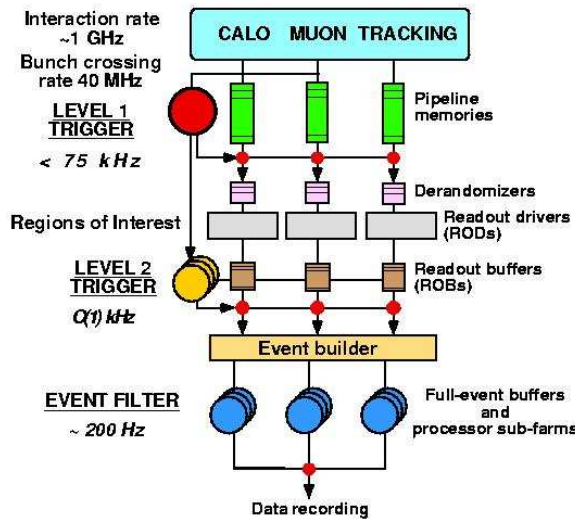


Figure 3.7.: Schematic diagram of the ATLAS trigger system.

4. Kinematic Fit – The Mathematical Concept

In this chapter the mathematical concept of the Kinematic Fit (KF) is introduced. It is a method which uses model assumptions of a physics process for fitting physical measured quantities. In the presented studies a certain topology of a particle decay is the assumed model. Constraints can be derived from the decay topology by applying energy- and momentum-conservation. The integration of the constraints into the KF positively affects its result.

The χ^2 method provides a technique to realise a fit to measured data. It is extended by the method of Lagrangian multipliers in order to take constraints into account. This extension allows to perform a KF. The aim is to fit the energies of the decay products of a $t\bar{t}$ system which are measured in the calorimeter. Thereby, the values of the measured energies, their assumed distribution and the constraints build the input for the method. On the one hand, the KF estimates how well the fitted energies fit to the measured values within their assumed errors. On the other hand, it takes the constraints into account. A systematical shift of the measured energies consequently affects the fit of the energies. Therefore, the KF yields a data calibration method for studying the JES for light quark and b quark jets separately.

The reconstruction of the decay topology can also be realised. A distinction between different jet assignments can be made, performing a KF for each jet combination. Using the combination of the best fit, results in an estimated jet assignment.

The implementation is carried out in ROOT [51], a C^{++} based object-oriented data analysis framework. The minimisation of the Lagrange function is performed by MINUIT [52], a tool for finding the minimum value of a multi-parameter function which is part of ROOT.

In the following, the mathematical concept of the χ^2 method is derived and the method of the Lagrangian multipliers is introduced. The application of the method to two concrete particle decays is realised in Chapter 5 for a pion decay as a simple example and in Chapter 6 for the decay of $t\bar{t}$ pairs as the central study of this thesis.

4.1. χ^2 without Constraints

The χ^2 -method (or *method of least squares*) can be deduced directly from the Likelihood method under the assumption of Gaussian distributed random variables [53–55]. It yields a χ^2 -function which gives a measure for the deviation of a theoretical model from a set of random variables (typically a data set). Minimising this function for the parameters of the model gives a possibility to estimate the most likely parameter values.

Let $\vec{y} := (y_1, \dots, y_n)^T$ be a vector of n random variables and \vec{y}' a particular set of measured data values with components y'_i , $i = 1, 2, \dots, n$ and a standard deviation σ'_i . Let furthermore \hat{y}_i , $i = 1, 2, \dots, n$ be predictions for the variables y_i given by a model $f(x'_i, \vec{a}) = \hat{y}_i$, which depends on n input variables x'_i and r parameters a_i , $i = 1, 2, \dots, r$. The probability to measure a certain value y'_i is denoted by $P(y'_i, \vec{a})$.

The Likelihood function \mathcal{L} is defined as the probability to obtain a whole dataset $\vec{y}' := (y'_1, y'_2, \dots, y'_n)^T$

$$\mathcal{L}(\vec{y}', \vec{a}) := P(y'_1, \vec{a}) \cdot P(y'_2, \vec{a}) \cdot \dots \cdot P(y'_n, \vec{a}). \quad (4.1)$$

Assuming Gaussian distributed random variables

$$P(y'_i, \vec{a}) = \frac{1}{\sigma_i \sqrt{2\pi}} \exp\left(-\frac{[y'_i - f(x'_i, \vec{a})]^2}{2\sigma_i'^2}\right) \quad (4.2)$$

the logarithm of the negative Likelihood function yields

$$-\ln \mathcal{L}(\vec{y}', \vec{a}) = \frac{1}{2} \sum_{i=1}^n \left[\frac{y'_i - f(x'_i, \vec{a})}{\sigma_i'} \right]^2 + \underbrace{\sum_{i=1}^n \ln \sigma_i' \sqrt{2\pi}}_{=\text{const.}}. \quad (4.3)$$

The χ^2 -function is defined as the negative logarithm of the total probability disregarding the factor $\frac{1}{2}$ and neglecting the constant term

$$\chi^2 := \sum_{i=1}^n \frac{[y'_i - f(x'_i, \vec{a})]^2}{\sigma_i'^2}. \quad (4.4)$$

Minimising the χ^2 -function gives a set of optimal parameter values \vec{a} with respect to the measured data \vec{y}'

$$\nabla_{\vec{a}}(\chi^2) \stackrel{!}{=} \vec{0}. \quad (4.5)$$

Thus the sum of the squared differences between the measured values and the predictions of the model takes its minimum weighted with the variance $\sigma_i'^2$ (*principle of least squares*).

Introducing matrix notation Equation (4.4) can be elegantly expressed which is from advantage for later calculations. Define the covariance matrix V as

$$V := \begin{pmatrix} \text{var}(y'_1) & \text{cov}(y'_1, y'_2) & \dots & \text{cov}(y'_1, y'_n) \\ \text{cov}(y'_2, y'_1) & \text{var}(y'_2) & \dots & \text{cov}(y'_2, y'_n) \\ \vdots & \vdots & \ddots & \vdots \\ \text{cov}(y'_n, y'_1) & \text{cov}(y'_n, y'_2) & \dots & \text{var}(y'_n) \end{pmatrix}. \quad (4.6)$$

If there is no correlation of the components y'_i , the covariance matrix becomes diagonal

$$V = \begin{pmatrix} \sigma_1'^2 & 0 & \dots & 0 \\ \vdots & \sigma_2'^2 & & \vdots \\ & & \ddots & 0 \\ 0 & \dots & 0 & \sigma_n'^2 \end{pmatrix}. \quad (4.7)$$

Assuming a linear model, $f(x'_i, \vec{a})$ can be written as

$$f(x'_i, \vec{a}) = a_1 f_1(x'_i) + a_2 f_2(x'_i) + \dots + a_p f_p(x'_i) \quad (4.8)$$

and a $n \times r$ matrix A , can be defined as

$$A := \begin{pmatrix} f_1(x'_1) & f_2(x'_1) & \cdots & f_r(x'_1) \\ f_1(x'_2) & f_2(x'_2) & \cdots & f_r(x'_2) \\ \vdots & \vdots & & \vdots \\ f_1(x'_n) & f_2(x'_n) & \cdots & f_r(x'_n) \end{pmatrix}. \quad (4.9)$$

Finally the χ^2 function can be rewritten as

$$\chi^2 := \sum_{i=1}^n \frac{[y'_i - f(x'_i, \vec{a})]^2}{\sigma_i'^2} = (\vec{y}' - A\vec{a})^T V^{-1} (\vec{y}' - A\vec{a}). \quad (4.10)$$

4.2. χ^2 with linear Constraints – The Method of the Lagrangian Multipliers

The method of Lagrangian multipliers is a technique to determine a local extremum with simultaneous consideration of constraints. Let a model consist of m constraints

$$f_k(\hat{\vec{a}}, \hat{\vec{y}}) = 0 \quad , k = 1, 2, \dots, m, \quad (4.11)$$

where $\hat{\vec{a}}$ and $\hat{\vec{y}}$ are the true values of r parameters and n variables, respectively. For each constraint an additional Lagrangian multiplier is introduced [56]. The Lagrange function L results from the sum of the χ^2 function and the constraints multiplied with a Lagrangian multiplier λ_k

$$L = \chi^2 + 2 \sum_{k=1}^m [\lambda_k \cdot f_k(\vec{a}, \vec{y})]. \quad (4.12)$$

The factor 2 is convention and cancels out when L is derived for the parameters \vec{a} or for the variables \vec{y} . The most suitable parameters \vec{a} are thus found by minimising the χ^2 -function considering the constraints $f_k(\vec{a}, \vec{y}) = 0$. However, in general equations $f_k(\vec{a}, \vec{y}) = 0$ are not exactly fulfilled, but perform a restraint to the random variables, such that the constraints are taken into account.

It is useful to introduce matrix notation. Define the vector consisting of the Lagrangian multipliers as follows

$$\vec{\lambda} := \begin{pmatrix} \lambda_1 \\ \lambda_2 \\ \vdots \\ \lambda_m \end{pmatrix}. \quad (4.13)$$

If one assumes that the constraints are *linear* they can be written as

$$\begin{pmatrix} f_1(\vec{a}, \vec{y}) \\ f_2(\vec{a}, \vec{y}) \\ \vdots \\ f_m(\vec{a}, \vec{y}) \end{pmatrix} =: (B\vec{a} + \vec{b}), \quad (4.14)$$

where B is a coefficient matrix of the parameters \vec{a} , and \vec{b} are the constant terms of the constraints. In the case of non-linear constraints a *linearisation* via a Taylor expansion is possible. Then the coefficient matrix has the form

$$B = \begin{pmatrix} \partial f'_1/\partial y_1 & \partial f'_1/\partial y_2 & \cdots & \partial f'_1/\partial y_n \\ \partial f'_2/\partial y_1 & \partial f'_2/\partial y_2 & \cdots & \partial f'_2/\partial y_n \\ \vdots & \vdots & \ddots & \vdots \\ \partial f'_m/\partial y_1 & \partial f'_m/\partial y_2 & \cdots & \partial f'_m/\partial y_n \end{pmatrix}, \quad (4.15)$$

where the prime symbol denotes a derivative at certain parameter values which represent initial values for the Taylor expansion

$$\frac{\partial f'}{\partial y_i} := \left(\frac{\partial f}{\partial y_i} \right)_{\vec{y} = \vec{y}'} = \text{const.}, \quad i = 1, 2, \dots, n. \quad (4.16)$$

Note that this implies that for every parameter y_i a corresponding value y'_i must exist. Using the defined matrices the Lagrange function can be finally written as

$$L = \underbrace{\left(\vec{y}' - A\vec{a} \right)^T V^{-1} \left(\vec{y}' - A\vec{a} \right)}_{\chi^2} + 2\vec{\lambda}^T \cdot \underbrace{\left(B\vec{a} - \vec{b} \right)}_{\text{Constraints}}. \quad (4.17)$$

Assuming the covariance matrix to be diagonal (as it has been done before), it follows that $(V^{-1})^T \equiv V^{-1}$ is fulfilled and the Lagrange multiplier can be written as a function of the parameters \vec{y}' and \vec{a}

$$\vec{\lambda}^T = \vec{\lambda}^T(\vec{y}', \vec{a}) = V_B^{-1} B C^{-1} \vec{c} - V_B^{-1} B \vec{a} \quad (4.18)$$

with $V_B := B C^{-1} B^T$, $C := A^T V^{-1} A$ and $\vec{c} := A^T V^{-1} \vec{y}'$. The complete calculation of the Lagrangian multipliers can be found in the appendix.

5. Test of the χ^2 Method: $\pi^0 \rightarrow \gamma\gamma$

In this chapter, the method of the KF is applied to the decay of a pion into two photons. The motivation is to test the performance of the KF using a simple example and to verify the concept of the χ^2 method works. Therefore, the Lagrange function of the decay is established in the first section. Subsequently, the data on which the method is applied is briefly described. Eventually, the results of the KF are presented.

5.1. Development of the Lagrange Function

In this section the χ^2 method is applied to the decay of a pion into two photons as a simple example of the KF. The fit parameters are the two energies E_1 and E_2 of the photons. The decay topology of a decaying pion is shown in Figure 5.1. The invariant mass of the photon pair is constrained to the pion mass.

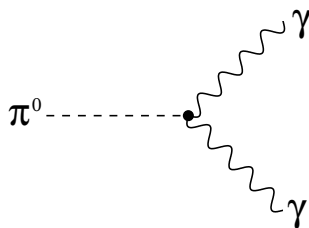


Figure 5.1.: LO Feynman diagram of a $\pi^0 \rightarrow \gamma\gamma$ decay.

Applying the KF, four assumptions (A) must be made:

- (A.1) The constraints can be expressed in linear terms.
- (A.2) There is no correlation between the measured values.
- (A.3) The direction of the particles are exactly known.
- (A.4) The fit parameters (photon energies) are Gaussian distributed.

The first assumption can be fulfilled by a linearisation of the constraints (e.g. via a Taylor extension). The second one is true because the measurement of the photon energy values happens independently within the detector. It follows that the covariance matrix of the measured values is diagonal which is essential for the applicability of the method (Section 4.2). The third assumption is legitimate, since the error of the measurement of the direction is much smaller compared to the resolution of the fitted quantities, the particle energies. The direction is needed for the reconstruction of the invariant mass of the pion. The last assumption is an approximation of the energy resolution of a calorimeter which is necessary in order to apply the χ^2 method. In Section 6.6.1 the bias of this assumption to the KF is investigated.

Let E'_i be the energy of the i -th photon and σ'_i the corresponding uncertainty of the measurement which is assumed to be Gaussian-like distributed (A.4). Then the χ^2 function is given by

$$\chi^2 = \frac{(E'_1 - E_1)^2}{\sigma_1'^2} + \frac{(E'_2 - E_2)^2}{\sigma_2'^2}. \quad (5.1)$$

Note that there is no model $f(x'_i, \vec{a}) = \hat{y}_i$ for the energies E_i which gives a theoretical value \hat{E}_i for the photon energies. E_i are free parameters. Minimisation for E_i leads to the measured values: for $E_i \equiv E'_i$ the χ^2 function becomes minimal, namely 0.

The χ^2 function alone does not improve the overall measurement. Thus constraints have to be taken into account. If the photons are assumed to originate from a π^0 , the invariant mass of the photon pair must be equal to the invariant mass of the pion. Hence, the following constraint f can be formulated:

$$f(E_1, E_2) := (p_1 + p_2)^2 - m_{\pi^0}^2 \stackrel{!}{=} 0 \quad (5.2)$$

$$\Leftrightarrow 2E_1E_2(1 - \cos\theta) - m_{\pi^0}^2 \stackrel{!}{=} 0, \quad (5.3)$$

where the angle between the two photons in the laboratory frame is denoted by θ , the mass of a photon is $m_\gamma = 0$ and for the pion mass the value $m_{\pi^0} = 134.9766$ MeV is used [6]. Without loss of generality the square of the invariant masses is taken. This is done due to simplicity. Otherwise the derivatives (see below) become more complicated. This constraint can be taken into account by the method of the Lagrangian multipliers (Section 4.2). Using the matrix notation for this decay this yields

$$\vec{y}' := \begin{pmatrix} E'_1 \\ E'_2 \end{pmatrix}; \quad \vec{a} := \begin{pmatrix} E_1 \\ E_2 \end{pmatrix}; \quad A := \begin{pmatrix} 1 & 0 \\ 0 & 1 \end{pmatrix} = \mathbf{1}_2; \quad B := \begin{pmatrix} \frac{\partial f'}{\partial E_1} & \frac{\partial f'}{\partial E_2} \end{pmatrix}; \quad (5.4)$$

$$V := \begin{pmatrix} \sigma_1'^2 & 0 \\ 0 & \sigma_2'^2 \end{pmatrix} \Leftrightarrow V^{-1} = \begin{pmatrix} \frac{1}{\sigma_1'^2} & 0 \\ 0 & \frac{1}{\sigma_2'^2} \end{pmatrix}; \quad \vec{b} := m_{\pi^0}^2, \quad (5.5)$$

where the prime mark denotes a derivative at certain parameter values

$$\frac{\partial f'}{\partial E_i} := \left(\frac{\partial f}{\partial E_i} \right)_{\substack{E_1 = E'_1 \\ E_2 = E'_2}} = \text{const.}, \quad i = 1, 2. \quad (5.6)$$

For the Lagrangian multiplier some auxiliary variables are needed (Equation (4.18)):

$$C := A^T V^{-1} A = \begin{pmatrix} \frac{1}{\sigma_1'^2} & 0 \\ 0 & \frac{1}{\sigma_2'^2} \end{pmatrix} \equiv V^{-1} \quad (5.7)$$

$$\vec{c} := A^T V^{-1} \vec{y}' = \begin{pmatrix} E'_1 / \sigma_1'^2 \\ E'_2 / \sigma_2'^2 \end{pmatrix} \quad (5.8)$$

$$V_B := B C^{-1} B^T = \left(\frac{\partial f'}{\partial E_1} \right)^2 \cdot \sigma_1'^2 + \left(\frac{\partial f'}{\partial E_2} \right)^2 \cdot \sigma_2'^2. \quad (5.9)$$

Inserting the matrices into Equation (4.18) one gets for the Lagrangian multiplier

$$\vec{\lambda}^T = \frac{\frac{\partial f'}{\partial E_1} \cdot (E'_1 - E_1) + \frac{\partial f'}{\partial E_2} \cdot (E'_2 - E_2)}{\left(\frac{\partial f'}{\partial E_1}\right)^2 \cdot \sigma_1'^2 + \left(\frac{\partial f'}{\partial E_2}\right)^2 \cdot \sigma_2'^2}. \quad (5.10)$$

The Lagrange function becomes according to Equation (4.17):

$$L(E'_1, E'_2, E_1, E_2) = \underbrace{\sum_{i=1}^2 \frac{(E'_i - E_i)^2}{\sigma_i'^2}}_{=(\vec{y}' - A\vec{a})^T V^{-1}(\vec{y}' - A\vec{a})} + 2\vec{\lambda}^T \cdot \left[\underbrace{\frac{\partial f'}{\partial E_1} \cdot E_1 + \frac{\partial f'}{\partial E_2} \cdot E_2}_{=B\vec{a}} - \underbrace{m_{\pi^0}^2}_{=\vec{b}} \right], \quad (5.11)$$

where the derivatives are

$$\frac{\partial f}{\partial E_1} = 2E_2 \cdot (1 - \cos \theta), \quad (5.12)$$

$$\frac{\partial f}{\partial E_2} = 2E_1 \cdot (1 - \cos \theta), \quad (5.13)$$

where θ is the angle between the two photons in the laboratory frame. Note that the final Lagrange function is identical to the Lagrange function which results from an analytical calculation without matrix notation, where a Taylor approximation is applied to linearise the constraints. Minimising this function for the energy parameters results in fitted photon energies which are – on average – closer to the true energy values of the photons than the measured ones (Section 5.3.2). This improvement arises from the insertion of the constraint into the KF: on the one hand the Lagrange function evaluates how well the energy parameters fit to the measured values within their errors σ_i' and on the other hand it takes the constraints into account.

The measured energy values represent *initial values* for the KF. This is pointed out when the Lagrange function is established analytically, including Taylor expansion of the constraints which is equivalent to the matrix notation as was mentioned before. For Taylor expansion an initial value is needed within the two-dimensional parameter space of the function. The Lagrange function can not be set up if there exist no initial value for all parameters.

The same holds for the error of a parameter: For the evaluation of Lagrangian multipliers an error is needed for every parameter (Equation (5.10)). Changing the error strongly affects the result of the KF.

5.2. Description of the Used Data

Events in which neutral pions decay into two photons are generated using the following algorithm: first, the momenta of the two photons in the rest frame of the pion are randomly generated in the x - y -plane, conserving the invariant mass of a π^0 . The mass of the pion is fixed to $m_{\pi^0} = 134.966$ GeV [6] and for the photons $m_\gamma = 0$ GeV, respectively. Secondly, the two photons are boosted into the y -direction with a gamma-factor of ten. Finally the energies of the photons are smeared according to a Gaussian resolution. Let

$$P_i := \begin{pmatrix} E_i \\ \vec{p}_i \end{pmatrix} = \begin{pmatrix} E_i \\ p_{i,x} \\ p_{i,y} \\ 0 \end{pmatrix} = E \cdot \begin{pmatrix} 1 \\ \cos \theta \\ \sin \theta \\ 0 \end{pmatrix}, \quad i = 1, 2 \quad (5.14)$$

be the four-momentum of the i -th photon in the rest frame of the decaying pion. One photon is generated uniformly distributed in a cone of 90° while the other one is exactly back-to-back $\vec{p}_1 = -\vec{p}_2$ (Figure 5.2).

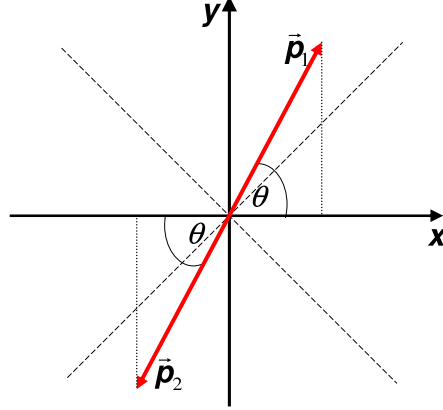


Figure 5.2.: Sketch of the decay $\pi^0 \rightarrow \gamma\gamma$ in the π^0 rest frame. The π^0 decays at the origin. The photons are released back-to-back in the x - y -plane, each within an angular range of 90° .

The simulated measured energy results from the energy resolution introduced in Chapter 3.2.2, Equation 3.6

$$\frac{\sigma'_i}{E_i^{true}} = \frac{(E'_i - E_i^{true})}{E_i} = \frac{a \cdot g}{\sqrt{E_i^{true}}} \quad \Leftrightarrow \quad E'_i = E_i^{true} + a \cdot g \cdot \sqrt{E_i^{true}}, \quad (5.15)$$

with $a = 10\%$ $\text{GeV}^{1/2}$ being the assumed detector specific resolution parameter for the measurement of the photon energy and g being a Gaussian distributed random number with a mean at zero and a width of one. These simulated measured energies are also called *smeared energies* in this thesis.

5.3. Studies with the KF

As an example, the parameter space of the Lagrange function is investigated for a single event with and without an invariant mass constraint. Subsequently, the relative energy resolution of 50,000 events before and after the KF are compared.

5.3.1. Parameter Space of the Lagrange Function of a Single Event

In case of the pion decay, the parameter space of the Lagrange function is two-dimensional (Equation (5.11)): one dimension for the energy of each photon. The parameter space is scanned by varying the photon energy parameters E_1 and E_2 and evaluating the Lagrange function. Figure 5.3 (left) shows the value of the χ^2 -terms of the Lagrange function (Equation (5.1)). The invariant mass constraint is not included here.

The peak marks the energy values of the photons for which the Lagrange function becomes minimal. These are the estimated energy values of the fit. Every other choice of the photon energies would lead to a larger value of the Lagrange function. The parameter space is continuous. It has only a global minimum, which yields the estimated energy values.

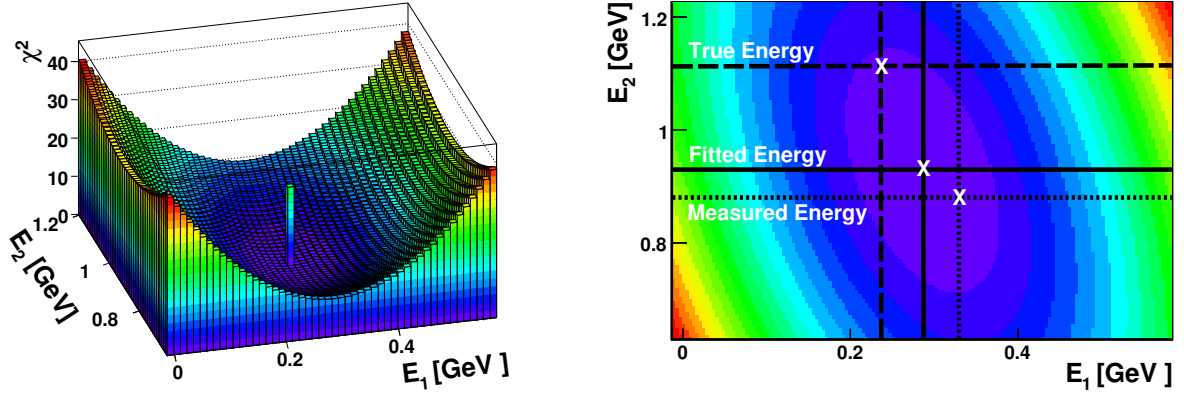


Figure 5.3.: Left: χ^2 terms of the Lagrange function of a pion decay as a function of the two photon energies for one single event. The fitted energy values are marked as a peak. Right: Lagrange function of a pion decay as a function of the two photon energies for one single event. Thereby the value of the Lagrange function is color-coded. Solid line: fitted energy value. Dashed line: true energy value. Dotted line: measured energy value. The anti-correlation of the two photon energies E_1 and E_2 can be recognized.

The parabolic character of the quadratic χ^2 terms can be recognized in the shape of the plot in Figure 5.3. The Lagrange function depends more strongly on the energy E_1 which can be recognized in the shape along the E_1 -axis: the parabola is narrower than along the E_2 -axis. This is because in this particular event the energy E_1 is smaller than the energy E_2 . Consequently, the error σ'_1 is smaller than σ'_2 and E_1 has a larger weight in the Lagrange function (Equation (5.1)).

The Lagrange function for the same event including the invariant mass constraint is shown in Figure 5.3 (right). The value of the Lagrange function is color-coded and the fitted, true and simulated measured energy values are marked.

An anti-correlation of the two photon energies can be recognized. This tendency results from the constraint. Inserting Equations (5.12) and (5.13) into Equation (5.11) yields the linearised constraint \tilde{f} :

$$\tilde{f} = 2(1 - \cos \theta)(E'_2 \cdot E_1 + E'_1 \cdot E_2) - m_{\pi^0}^2 \stackrel{!}{=} 0. \quad (5.16)$$

If the energy of the first photon increases the energy of the second one must decrease in order to provide the invariant mass of the pion. Note that including a distinct value for m_{π^0} an *absolute reference value* is introduced into the KF. Consequently, this constraint performs a strong restraint to the fit and establishes the relationship to an absolute energy scale (compare the investigations for the JES, Section 6.7.2). In this particular event plotted in Figure 5.3 the fitted energy values are closer to the true energy values than the measured ones. Thus for this single event the fit result yields an improvement of the measured energies. If this tendency holds on average for an ensemble of events, the KF positively affects the energy resolution. This is investigated in the next section.

5.3.2. Studies of the Energy Resolution

The characteristic calorimeter resolution parameter for the energy resolution is chosen to be $a = 10\% \text{ GeV}^{1/2}$ (Section 5.2). In Figure 5.4 (left) the energy resolution of the simulated measured energies of one photon is plotted.

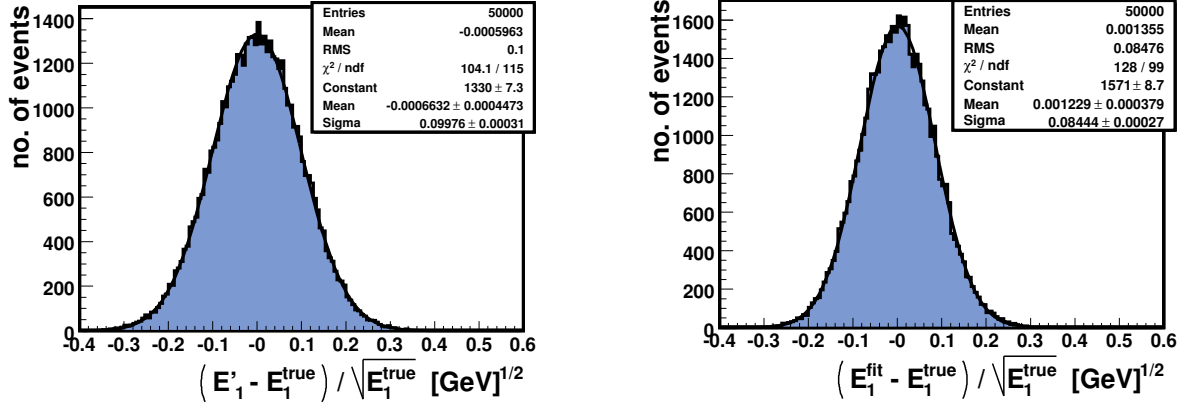


Figure 5.4.: Left: energy resolution of one photon before the KF. The characteristic energy resolution parameter is assumed to be $a = 10\%$. The width of the gauss fit correspond to this parameter and is $\sigma_1 = (0.09976 \pm 0.00031) \text{ GeV}^{1/2} \approx a$. Right: energy resolution for the two photons after the KF. The width of the gauss fit yields $\sigma_1 = (0.08444 \pm 0.00027) \text{ GeV}^{1/2}$ which is an improvement of the resolution of about 15.4%.

The width of the Gauss fit of this distribution directly reflects the characteristic energy resolution parameter 'a' of the detector. For this sample $\sigma_1 = (0.09976 \pm 0.00031) \text{ GeV}^{1/2}$ for one photon. This is in accordance with the implemented resolution of $a = 10\% \text{ GeV}^{1/2}$.

The same quantity is plotted for the photon energy obtained from the fit in Figure 5.4 (right). The corresponding width of the distribution is $\sigma_1 = (0.08444 \pm 0.00027) \text{ GeV}^{1/2}$. Similar results follow for the second photon. Table 5.1 summarises the widths of the energy resolutions and their relative improvement $\frac{|\sigma'_i - \sigma_i^{\text{fit}}|}{\sigma_i}$.

Table 5.1.: Widths σ of the Gaussian fit to the energy resolutions of the two photons. The widths of the measured values represents the characteristic energy resolution parameter of the detector. "Rel. impr." denotes the relative improvement of the width due to the fit. The error is the error of the mean of the Gaussian fit.

object	$\sigma' [\text{GeV}]^{1/2}$	$\sigma^{\text{fit}} [\text{GeV}]^{1/2}$	rel. impr. [%]
photon 1	0.09976 ± 0.00031	0.08444 ± 0.00027	15.357 ± 0.003
photon 2	0.09981 ± 0.00032	0.08443 ± 0.00027	15.409 ± 0.003

Regarding an ensemble of particles the consideration of the invariant mass constraint yields an improvement of the energy resolution: without the constraint the fitted energy values are identical to the smeared ones and no improvement of the energy resolution can be performed. Insertion of the constraint results in fitted energies which, on average, are closer to the true energy values than the smeared ones. This is reflected in the relative improvement of the energy resolution of more than 15%. Thus the KF is successful and it positively affects the fit result.

6. Application of the χ^2 Method: $t\bar{t} \rightarrow q\bar{q}b\bar{b}e\bar{\nu}_e$

In this chapter the method of the KF is applied to the decay of a $t\bar{t}$ system via the semi-leptonic channel. Firstly, the Lagrange function of the decay is established. Subsequently, the data on which the method is applied is briefly described. The studies performed in this thesis are fully based on simulated MC data. Thereby, the KF is applied to different data sources for studying systematical effects. Eventually, the results of the KF are presented separately for every data source.

6.1. Development of the Lagrange Function

In this section the χ^2 method is applied to the semi-leptonic decay of a $t\bar{t}$ system. The fit parameters are the energies $E_q, E_{\bar{q}}, E_{b_{had}}, E_{b_{lep}}$ and E_{lep} of the two light quark jets, the two b quark jets and the released lepton, respectively.

In this case, the same assumptions are made as for the decay of a pion (Section 5.1, assumptions A.1 to A.4). The following notation is used: let p_α be the four-vector for the momentum of particle α

$$p_\alpha = \begin{pmatrix} E_\alpha \\ p_{\alpha,x} \\ p_{\alpha,y} \\ p_{\alpha,z} \end{pmatrix} = \begin{pmatrix} E_\alpha \\ \vec{p}_\alpha \end{pmatrix}. \quad (6.1)$$

The index α labels the final state particle: light quark (q), anti-light quark (\bar{q}), bottom quark (b_{had}) of the hadronically decaying top quark (t_{had}), bottom quark (b_{lep}) of the leptonically decaying top quark (t_{lep}), lepton (lep) and the corresponding neutrino (ν). The χ^2 function for the $t\bar{t}$ system is

$$\chi^2 = \sum_{\alpha} \frac{(E'_\alpha - E_\alpha)^2}{\sigma_\alpha'^2}, \quad \alpha = q, \bar{q}, b_{had}, b_{lep}, lep. \quad (6.2)$$

Note that the sum does not include the neutrino, since it is not measured. However, the unknown energy of the neutrino is replaced by exploiting a constraint (see below).

Three constraints can be formulated from the decay topology of the semi-leptonic channel:

$$f_1(E_q, E_{\bar{q}}, E_{b_{had}}, E_{b_{lep}}, E_{lep}, E_\nu) := (p_q + p_{\bar{q}} + p_{b_{had}})^2 - (p_{b_{lep}} + p_{lep} + p_{b_\nu})^2 \stackrel{!}{=} 0, \quad (6.3)$$

$$f_2(E_q, E_{\bar{q}}) := (p_q + p_{\bar{q}})^2 - m_W^2 \stackrel{!}{=} 0, \quad (6.4)$$

$$f_3(E_{lep}, E_\nu) := (p_{lep} + p_\nu)^2 - m_W^2 \stackrel{!}{=} 0. \quad (6.5)$$

The first constraint, the *equal-mass constraint*, comes from the assumption that the invariant mass of the top quark and anti-top quark are equal.¹ The second constraint, the *first W-mass constraint*, implies that the invariant mass of the hadronically decaying W boson is equal to the invariant mass of the sum of the two released light quarks. The third constraint, the *second W-mass constraint*, demands that the invariant mass of the leptonically decaying W boson is equal to the invariant mass of the sum of the released lepton and neutrino. The distribution of the W masses remain unconsidered. The mass is assumed to be $m_W = 80.403$ GeV [6].

The transverse momentum of the neutrino can be reconstructed from the transverse momentum of the other decay products via two additional assumptions

$$p_{\nu,x} = - (p_{q,x} + p_{\bar{q},x} + p_{b_{had},x} + p_{b_{lep},x} + p_{lep,x}), \quad (6.6)$$

$$p_{\nu,y} = - (p_{q,y} + p_{\bar{q},y} + p_{b_{had},y} + p_{b_{lep},y} + p_{lep,y}). \quad (6.7)$$

For the complete reconstruction of the neutrino, its z -component must be determined. Thus one additional piece of information is needed. Using the third constraint, Equation (6.5) can be solved for $p_{\nu,z}$ which leads to a quadratic equation and thus to two solutions $p_{\nu,z}^{(1)}$ and $p_{\nu,z}^{(2)}$ for the longitudinal momentum:

$$p_{\nu,z}^{(1,2)} = ab \cdot p_{lep,z} \pm \sqrt{a^2 b^2 \cdot p_{lep,z}^2 + ab^2 - a \cdot E_{lep}^2 \cdot (p_{\nu,x}^2 + p_{\nu,y}^2)}, \quad (6.8)$$

with

$$a := \frac{1}{p_{lep,x}^2 + p_{lep,y}^2}; \quad b := \left[\frac{m_W^2}{2} + (p_{lep,x} p_{\nu,x} + p_{lep,y} p_{\nu,y}) \right]. \quad (6.9)$$

The full calculation can be found in the appendix. It is possible that the discriminant of Equation 6.8 becomes negative. No physically reasonable neutrino can be reconstructed in this case and a KF is not possible. If applicable both solutions are evaluated. The solution with the smaller χ^2 value is chosen. Calculating $p_{\nu,z}$ the energy of the neutrino can be determined as

$$E_\nu = |\vec{p}_\nu| = \sqrt{p_{\nu,x}^2 + p_{\nu,y}^2 + p_{\nu,z}^2}, \quad (6.10)$$

where the assumption $m_\nu \approx 0$ is made. Therefore, the neutrino energy is a function of the other energies

$$E_\nu = E_\nu(E_q, E_{\bar{q}}, E_{b_{had}}, E_{b_{lep}}, E_{lep}). \quad (6.11)$$

The reconstructed neutrino can be inserted into the first constraint (Equation (6.3)). Consequently, it no longer depends on the neutrino energy, but only on the five energies of the observable particles. Thus the Lagrange function for the $t\bar{t}$ decay only contains the first two constraints (the third constraint is entirely exploited for the neutrino reconstruction). The matrices and vectors needed for the calculation of the Lagrange function and the Lagrange multipliers are:

$$\vec{y} := \begin{pmatrix} E'_q \\ E'_{\bar{q}} \\ E'_{b_{had}} \\ E'_{b_{lep}} \\ E'_{lep} \end{pmatrix}; \quad \vec{a} := \begin{pmatrix} E_q \\ E_{\bar{q}} \\ E_{b_{had}} \\ E_{b_{lep}} \\ E_{lep} \end{pmatrix}; \quad A := \begin{pmatrix} 1 & 0 & 0 & 0 & 0 \\ 0 & 1 & 0 & 0 & 0 \\ 0 & 0 & 1 & 0 & 0 \\ 0 & 0 & 0 & 1 & 0 \\ 0 & 0 & 0 & 0 & 1 \end{pmatrix} = \mathbf{1}_5; \quad (6.12)$$

¹In fact, the masses of the measured particles are not exactly determined, but Breit-Wigner-like distributed with a width of approximately 1.5 GeV/ c^2 . This is not accounted for in the formulation of the χ^2 -function. The Likelihood method offers the possibility to apply Breit-Wigner distributed parameters.

$$V := \begin{pmatrix} \sigma_q'^2 & 0 & 0 & 0 & 0 \\ 0 & \sigma_{\bar{q}}'^2 & 0 & 0 & 0 \\ 0 & 0 & \sigma_{b_{had}}'^2 & 0 & 0 \\ 0 & 0 & 0 & \sigma_{b_{lep}}'^2 & 0 \\ 0 & 0 & 0 & 0 & \sigma_{lep}'^2 \end{pmatrix} \Leftrightarrow V^{-1} = \begin{pmatrix} \frac{1}{\sigma_q'^2} & 0 & 0 & 0 & 0 \\ 0 & \frac{1}{\sigma_{\bar{q}}'^2} & 0 & 0 & 0 \\ 0 & 0 & \frac{1}{\sigma_{b_{had}}'^2} & 0 & 0 \\ 0 & 0 & 0 & \frac{1}{\sigma_{b_{lep}}'^2} & 0 \\ 0 & 0 & 0 & 0 & \frac{1}{\sigma_{lep}'^2} \end{pmatrix}; \quad (6.13)$$

$$\vec{b} := \begin{pmatrix} 0 \\ m_W^2 \end{pmatrix}; \quad B := \begin{pmatrix} \frac{\partial f_1'}{\partial E_q} & \frac{\partial f_1'}{\partial E_{\bar{q}}} & \frac{\partial f_1'}{\partial E_{b_{had}}} & \frac{\partial f_1'}{\partial E_{b_{lep}}} & \frac{\partial f_1'}{\partial E_{lep}} \\ \frac{\partial f_2'}{\partial E_q} & \frac{\partial f_2'}{\partial E_{\bar{q}}} & \frac{\partial f_2'}{\partial E_{b_{had}}} & \frac{\partial f_2'}{\partial E_{b_{lep}}} & \frac{\partial f_2'}{\partial E_{lep}} \end{pmatrix}; \quad (6.14)$$

$$C := A^T V^{-1} A = \begin{pmatrix} \frac{1}{\sigma_q'^2} & 0 & 0 & 0 & 0 \\ 0 & \frac{1}{\sigma_{\bar{q}}'^2} & 0 & 0 & 0 \\ 0 & 0 & \frac{1}{\sigma_{b_{had}}'^2} & 0 & 0 \\ 0 & 0 & 0 & \frac{1}{\sigma_{b_{lep}}'^2} & 0 \\ 0 & 0 & 0 & 0 & \frac{1}{\sigma_{lep}'^2} \end{pmatrix} \equiv V^{-1}; \quad (6.15)$$

$$\vec{c} := A^T V^{-1} \vec{y}' = \begin{pmatrix} E_q' / \sigma_q'^2 \\ E_{\bar{q}}' / \sigma_{\bar{q}}'^2 \\ E_{b_{had}}' / \sigma_{b_{had}}'^2 \\ E_{b_{lep}}' / \sigma_{b_{lep}}'^2 \\ E_{lep}' / \sigma_{lep}'^2 \end{pmatrix}; \quad (6.16)$$

$$V_B := B C^{-1} B^T = \sum_{\alpha} \left(\frac{\partial f'}{\partial E_{\alpha}} \right)^2 \cdot \sigma_{\alpha}'^2, \quad \alpha = q, \bar{q}, b_{had}, b_{lep}, lep. \quad (6.17)$$

$$\Rightarrow \vec{\lambda}^T = \left(\frac{\sum_{\alpha} \frac{\partial f_1'}{\partial E_{\alpha}} \cdot (E_{\alpha}' - E_{\alpha})}{\sum_{\alpha} \left(\frac{\partial f_1'}{\partial E_{\alpha}} \right)^2 \cdot \sigma_{\alpha}'^2}, \frac{\sum_{\beta} \frac{\partial f_2'}{\partial E_{\beta}} \cdot (E_{\beta}' - E_{\beta})}{\sum_{\beta} \left(\frac{\partial f_2'}{\partial E_{\beta}} \right)^2 \cdot \sigma_{\beta}'^2} \right), \quad (6.18)$$

with $\alpha := q, \bar{q}, b_{had}, b_{lep}, lep$ and $\beta := q, \bar{q}$. The Lagrange function is

$$L(E_{\alpha}', E_{\alpha}) = \underbrace{\sum_{\alpha} \frac{(E_{\alpha}' - E_{\alpha})^2}{\sigma_{\alpha}'^2}}_{=(\vec{y}' - A\vec{a})^T V^{-1} (\vec{y}' - A\vec{a})} + 2\vec{\lambda}^T \cdot \left[\underbrace{\begin{pmatrix} \sum_{\alpha} \frac{\partial f_1'}{\partial E_{\alpha}} \cdot E_{\alpha} \\ \sum_{\beta} \frac{\partial f_2'}{\partial E_{\beta}} \cdot E_{\beta} \end{pmatrix}}_{=B\vec{a}} - \underbrace{\begin{pmatrix} 0 \\ m_W^2 \end{pmatrix}}_{=\vec{b}} \right]. \quad (6.19)$$

The derivatives can be found in the appendix. Note that for the derivatives two additional approximations are made:

$$m_q = m_{\bar{q}} \approx 0, \quad (6.20)$$

$$m_{lep} \approx 0. \quad (6.21)$$

The light quarks and leptons are assumed to be massless.

The Lagrange function contains five energy parameters. An improvement of the energy resolution is expected, meaning that on average they are closer to the true energy values than the measured ones (Section 6.5.1).

At the Tevatron the centre-of-mass energy barely suffices to produce a $t\bar{t}$ pair. Hence, the assumption that a produced $t\bar{t}$ system has no additional transverse momentum is appropriate. However, at the LHC this assumption is not fulfilled due to its higher energy. Therefore, it must be considered in the KF.

The introduction of the transverse momentum of the $t\bar{t}$ system $p_{t\bar{t},T}$ to the χ^2 method is problematic: $p_{t\bar{t},T}$ is an unmeasured parameter. Thus no initial value exists which is needed for the Taylor expansion as discussed in Section 5.1. The error for $p_{t\bar{t},T}$ is of similar importance since it is essential for the evaluation of the Lagrangian multiplier and strongly influences the fit result.

Nevertheless, in these studies the KF is also investigated with respect to $p_{t\bar{t},T}$. Therefore, two new parameters are introduced: the transverse momentum of the $t\bar{t}$ system in x -direction and in y -direction which are denoted $p_{t\bar{t},x}$ and $p_{t\bar{t},y}$, respectively.² The transverse momentum directly affects the solution of the neutrino:

$$p_{\nu,x} = p_{t\bar{t},x} - (p_{q,x} + p_{\bar{q},x} + p_{b_{had},x} + p_{b_{lep},x} + p_{lep,x}), \quad (6.22)$$

$$p_{\nu,y} = p_{t\bar{t},y} - (p_{q,y} + p_{\bar{q},y} + p_{b_{had},y} + p_{b_{lep},y} + p_{lep,y}). \quad (6.23)$$

This is the only point where the transverse momentum of the $t\bar{t}$ system occurs within the KF. It is not reasonable to add a new Gaussian term for each parameter $p_{t\bar{t},x}$ and $p_{t\bar{t},y}$ because of two reasons: firstly, the distribution of $p_{t\bar{t},x}$ and $p_{t\bar{t},y}$ is not Gaussian-like and secondly the best estimators for initial values are

$$p'_{t\bar{t},x} = 0, \quad (6.24)$$

$$p'_{t\bar{t},y} = 0, \quad (6.25)$$

because these are the most probable values. Thus a Gaussian term would yield

$$\frac{(p'_{t\bar{t},x} - p_{t\bar{t},x})^2}{\sigma'^2_{t\bar{t},x}} = \frac{(p_{t\bar{t},x})^2}{\sigma'^2_{t\bar{t},x}}, \quad (6.26)$$

$$\frac{(p'_{t\bar{t},y} - p_{t\bar{t},y})^2}{\sigma'^2_{t\bar{t},y}} = \frac{(p_{t\bar{t},y})^2}{\sigma'^2_{t\bar{t},y}}, \quad (6.27)$$

which would impose a restraint such that always smaller values are preferred. Estimated errors $\sigma'_{t\bar{t},x}$ and $\sigma'_{t\bar{t},y}$ are needed in order to calculate the Lagrangian multipliers. Therefore, constant values were taken from the RMS value of the $p_{t\bar{t},x}$ and $p_{t\bar{t},y}$ distributions. The analogous calculation for the Lagrange function with respect to the transverse momentum yields:

$$\vec{y} := \begin{pmatrix} E'_q \\ E'_{\bar{q}} \\ E'_{b_{had}} \\ E'_{b_{lep}} \\ E'_{lep} \\ 0 \\ 0 \end{pmatrix}; \quad \vec{a} := \begin{pmatrix} E_q \\ E_{\bar{q}} \\ E_{b_{had}} \\ E_{b_{lep}} \\ E_{lep} \\ p_{t\bar{t},x} \\ p_{t\bar{t},y} \end{pmatrix}; \quad A := \begin{pmatrix} 1 & 0 & 0 & 0 & 0 & 0 & 0 \\ 0 & 1 & 0 & 0 & 0 & 0 & 0 \\ 0 & 0 & 1 & 0 & 0 & 0 & 0 \\ 0 & 0 & 0 & 1 & 0 & 0 & 0 \\ 0 & 0 & 0 & 0 & 1 & 0 & 0 \\ 0 & 0 & 0 & 0 & 0 & 1 & 0 \\ 0 & 0 & 0 & 0 & 0 & 0 & 1 \end{pmatrix} = \mathbb{1}_7; \quad (6.28)$$

²An equivalent approach is the introduction of the parameters $p_{t\bar{t},T}$ and the angular $\phi_{t\bar{t}}$ in the x - y -plane.

$$V := \begin{pmatrix} \sigma_q'^2 & 0 & 0 & 0 & 0 & 0 & 0 \\ 0 & \sigma_{\bar{q}}'^2 & 0 & 0 & 0 & 0 & 0 \\ 0 & 0 & \sigma_{b_{had}}'^2 & 0 & 0 & 0 & 0 \\ 0 & 0 & 0 & \sigma_{b_{lep}}'^2 & 0 & 0 & 0 \\ 0 & 0 & 0 & 0 & \sigma_{lep}'^2 & 0 & 0 \\ 0 & 0 & 0 & 0 & 0 & \sigma_{t\bar{t},x}'^2 & 0 \\ 0 & 0 & 0 & 0 & 0 & 0 & \sigma_{t\bar{t},y}'^2 \end{pmatrix}; \quad (6.29)$$

$$\vec{b} := \begin{pmatrix} 0 \\ m_W^2 \end{pmatrix}; \quad B := \begin{pmatrix} \frac{\partial f_1'}{\partial E_q} & \frac{\partial f_1'}{\partial E_{\bar{q}}} & \frac{\partial f_1'}{\partial E_{b_{had}}} & \frac{\partial f_1'}{\partial E_{b_{lep}}} & \frac{\partial f_1'}{\partial E_{lep}} & \frac{\partial f_1'}{\partial p_{t\bar{t},x}} & \frac{\partial f_1'}{\partial p_{t\bar{t},y}} \\ \frac{\partial f_2'}{\partial E_q} & \frac{\partial f_2'}{\partial E_{\bar{q}}} & \frac{\partial f_2'}{\partial E_{b_{had}}} & \frac{\partial f_2'}{\partial E_{b_{lep}}} & \frac{\partial f_2'}{\partial E_{lep}} & \frac{\partial f_2'}{\partial p_{t\bar{t},x}} & \frac{\partial f_2'}{\partial p_{t\bar{t},y}} \end{pmatrix}; \quad (6.30)$$

$$C := A^T V^{-1} A \equiv V^{-1} \quad (6.31)$$

$$\vec{c} := A^T V^{-1} \vec{y}' = \begin{pmatrix} E_q'/\sigma_q'^2 \\ E_{\bar{q}}'/\sigma_{\bar{q}}'^2 \\ E_{b_{had}}'/\sigma_{b_{had}}'^2 \\ E_{b_{lep}}'/\sigma_{b_{lep}}'^2 \\ E_{lep}'/\sigma_{lep}'^2 \\ 0 \\ 0 \end{pmatrix}; \quad (6.32)$$

$$V_B := B C^{-1} B^T = \sum_{\gamma} \left(\frac{\partial f'_{\gamma}}{\partial E_{\gamma}} \right)^2 \cdot \sigma_{\gamma}'^2, \quad \gamma = q, \bar{q}, b_{had}, b_{lep}, lep, t\bar{t}, x, t\bar{t}, y. \quad (6.33)$$

$$\Rightarrow \vec{\lambda}^T = \begin{pmatrix} \frac{\sum_{\gamma} \frac{\partial f_1'}{\partial E_{\gamma}} \cdot (E'_{\gamma} - E_{\gamma})}{\sum_{\gamma} \left(\frac{\partial f_1'}{\partial E_{\gamma}} \right)^2 \cdot \sigma_{\gamma}'^2} & \frac{\sum_{\beta} \frac{\partial f_2'}{\partial E_{\beta}} \cdot (E'_{\beta} - E_{\beta})}{\sum_{\beta} \left(\frac{\partial f_2'}{\partial E_{\beta}} \right)^2 \cdot \sigma_{\beta}'^2} \end{pmatrix}, \quad (6.34)$$

with $\gamma := q, \bar{q}, b_{had}, b_{lep}, lep, t\bar{t}, x, t\bar{t}, y$ and $\beta := q, \bar{q}$. Finally the Lagrange function is

$$L(E'_{\alpha}, E_{\alpha}) = \sum_{\alpha} \frac{(E'_{\alpha} - E_{\alpha})^2}{\sigma_{\alpha}'^2} + 2\vec{\lambda}^T \cdot \left[\underbrace{\begin{pmatrix} \sum_{\gamma} \frac{\partial f_1'}{\partial E_{\gamma}} \cdot E_{\gamma} \\ \sum_{\beta} \frac{\partial f_2'}{\partial E_{\beta}} \cdot E_{\beta} \end{pmatrix}}_{=B\vec{a}} - \underbrace{\begin{pmatrix} 0 \\ m_W^2 \end{pmatrix}}_{=\vec{b}} \right]. \quad (6.35)$$

6.2. Description of the Used Data

Three different MC data samples serve as input for the KF in order to test its performance:

- MadEvent data on parton level in LO. The simulated measured energies are Gaussian-like smeared.
- MadEvent data on parton level in LO. The simulated measured energies are smeared with an energy resolution based on the ATLAS detector.
- Fully simulated ATLAS data in NLO. The simulated detector signals are generated with respect to the components, geometry and properties of the ATLAS detector.

The motivation for the use of different input data is to understand systematically effects coming from energy resolution or ISR and FSR for instance. In the following the different data sources are described.

6.2.1. $t\bar{t}$ Events Generated with MadEvent

10,000 $t\bar{t}$ pairs in the semi-leptonic decay channel are simulated with MadEvent [57] in LO. MadEvent is a tree-level event generator based on the matrix element creator MadGraph [58, 59]. The $t\bar{t}$ pairs are simulated to be produced solely via gluon-gluon-fusion and always decay in the same way: the top quark decays hadronically, into an up quark and an anti-down quark. The anti-top quark always decays leptonically into a muon and the corresponding muon-anti-neutrino. An η -cut of $|\eta| < 2.5$ is applied on the light quarks and the muon. The invariant top- and anti-top quark masses are Breit-Wigner distributed with a mean of 175 GeV/ c^2 and a width of 1.5 GeV/ c^2 .

The MC energies of the partons and charged leptons are smeared in two different ways for two different studies:

- Gaussian-like as used in Section 5.2 for testing the KF with the same energy resolution which is assumed in the method. To go into detail, a Gaussian distributed random number g with a mean at zero and a width of one was generated in order to simulate measured energy values according to

$$E'_\alpha = E_\alpha^{true} + a_\beta \cdot g \cdot \sqrt{E_\alpha^{true}}, \quad \alpha := q, \bar{q}, b_{had}, b_{lep}, lep; , \quad \beta := lq, b, lep. \quad (6.36)$$

For this detector resolution the parameters

$$a_{el} = 0.1627 \text{ GeV}^{1/2} \quad (\text{electrons}) \quad (6.37)$$

$$a_{lq} = 1.236 \text{ GeV}^{1/2} \quad (\text{light quarks}) \quad (6.38)$$

$$a_{bq} = 1.45 \text{ GeV}^{1/2} \quad (\text{b quarks}) \quad (6.39)$$

are taken. These values are extracted from a Gaussian fit to the energy resolution of the simulated ATLAS data which is described in Section 6.2.2.

- Smeared according to the energy resolution which results from simulated ATLAS events (Section 6.7.3) for a more realistic test.³

Since the energy of the partons is smeared according to an energy resolution which correspond to jets, the simulated measured particles are also called *jets*.

³ROOT offers the possibility to generate a distribution according to a distribution of an arbitrary histogram.

6.2.2. $t\bar{t}$ Events Generated with MC@NLO Using TopView

A sample of di-leptonic + semi-leptonic $t\bar{t}$ events of the decay of a $t\bar{t}$ system has been generated using a MC@NLO generator for the event simulation on parton level. Geant4 [60] has been used to propagate the final state particles and simulate the ATLAS detector. The generated data sample consists of roughly 540,000 events with an integrated luminosity of 217 pb^{-1} and a cross section of 461 pb. Since the data is generated as realistic as possible with respect to the ATLAS detector, the simulated detector signals of the calorimeter are not calibrated.

TopView [61] is a data analysis package for ATLAS top physics analysis and was used to create a Root-tuple from the data sample. Root-Tuples are files in which event data is systematically saved within a tree-structure. TopView also provides the matching of data. Matching means the assignment of the simulated signals of a detector to the underlying physics processes on parton level.

Matching

For the studies made in this thesis matched data is from great importance because the matching flags signals, coming directly from the $t\bar{t}$ decay. Hence, investigations with data purely consisting of signals without Initial State Radiation (ISR) or Final State Radiation (FSR) are possible by a selection of events with respect to a matching flag. Therefore, the matching criteria are discussed in the following.

There are different objects which have to be matched in different ways. Object is the genus for muon, electron, photon, tau and jet for example. It can happen that the criteria for several different objects are fulfilled for the same detector signal. In order to remove the overlap between objects the following sequence of object identification is adhered: Muon, Loose-Muon, Electron, Loose-Electron, Photon, Tau-Jet, Particle-Jet. Since in this thesis the semi-leptonic decay of $t\bar{t}$ pairs is investigated, only the matching criteria for electrons, muons and jets are shown in Table 6.1.

Table 6.1.: Cut criteria for the matching of electrons, muons and jets by TopView. E_T is the transverse energy, ΔR and Isolation Cone refer to a cone in the η - ϕ -plane, the Isolation Cut denotes the maximum allowed additional energy within the Isolation Cone, the flag “Use is EM” demands a signal in the EM Cal, whereas the Degrees of Freedom set a limit on the minimum number of hits in the muon system.

object	criterion	value
electron	E_T Cut	$\geq 20 \text{ GeV}$
	ΔR Cone	≤ 0.4
	Isolation Cone	≤ 0.2
	Isolation Cut	$\leq 6 \text{ GeV}$
	Use is EM	true
muon	E_T Cut	$\geq 20 \text{ GeV}$
	ΔR Cone	≤ 0.4
	Isolation Cone	≤ 0.2
	Isolation Cut	$\leq 6 \text{ GeV}$
	Degrees of Freedom	≤ 20
jet	E_T Cut	$\geq 15 \text{ GeV}$
	ΔR Cone	≤ 0.4

The E_T cut defines the minimum transverse energy for an object. The ΔR cone and isolation cone are defined as a cone in the η - ϕ -plane. An object must be located in a well-defined ΔR cone. If another object is already identified within the cone, the object will not be inserted. In the isolation cone it is tested how much additional energy is deposited except for the energy of the object, e.g. a muon. The isolation cut energy defines the maximum allowed additional energy deposited within the isolation cone. If it is exceeded the object is regarded as not isolated and discarded. Electrons deposit their energy in the EM Cal. Thus a signal in this detector component is expected. Therefore, a flag can be set (“Use is EM”) – if no signal is found in the EM Cal, no electron is reconstructed. Multiple hits in the tracking system are required for the track reconstruction. The number of hits is not constant. The more hit points the better the track reconstruction. If too few hit points are measured, no adequate track reconstruction can be realised. A degree of freedom arises for instance from a muon chamber layer in which no signal was measured. To set a lower limit for the minimum number of hit points, the number of degrees of freedom must not exceed a certain limit (for muons e.g. the limit is 20 degrees of freedom). Otherwise the object is discarded.

Selection Cuts

Selection cuts must be applied to the data sample in order to extract the semi-leptonic decay channel from the data sample. The selection happens in two steps: firstly, cuts are applied to data on parton level (MC data). This is done to receive a skimmed data sample which consists only of the decay products of the semi-leptonic decay of $t\bar{t}$ systems where one electron is released. In addition a bug is considered (see below). In the second step, a selection is applied to the reconstructed objects (*reco data*). Table 6.2 summarises the cuts to the Root-Tuple generated by TopView and the relative and absolute percentage of the number of skimmed events.

Table 6.2.: Overview of the number of events of the TopView data before and after applying selection cuts. The relative percentage indicates the percentage of events which remain after the use of an additional cut. The absolute percentage reflects the percentage with respect to the initial number of events in the TopView data sample. The error of the percentages follows from Poisson statistics. The top quark mass cut rejects non-realistic events which are afflicted with a bug. In the last three lines tight cuts have been applied.

No.	Cut	No. of Events	Rel. Percent.	Abs. Percent.
0	entire sample	541,050	100.00	100.00
1	1 t_{had} , 1 t_{lep} , 1 lepton	433,674	80.15 ± 0.15	80.15 ± 0.14
2	exactly 1 electron	144,243	33.26 ± 0.26	26.66 ± 0.14
3	top quark mass cut	108,202	75.01 ± 0.30	20.00 ± 0.14
4a	1 electron in detector	69,780	64.49 ± 0.38	12.90 ± 0.14
5a	4 jets in detector	18,880	27.06 ± 0.73	3.49 ± 0.14
6a	all 4 jets matched	6,564	34.77 ± 1.23	1.27 ± 0.14
4b	1 good electron in detector	16,998	24.36 ± 0.77	3.14 ± 0.14
5b	4 good jets in detector	6,276	36.92 ± 1.26	1.16 ± 0.14
6b	all 4 good jets matched	2,961	47.18 ± 1.84	0.55 ± 0.14

Selection Cuts on MC data

The first cut (cut 1) ensures that only the semi-leptonic decay channel is selected by demanding exactly one hadronically and one leptonically decaying top quark and one lepton in an event. Di-leptonic events are thus rejected. Approximately 20% of the events are removed by this cut.

This is consistent with the branching ratios of the decaying $t\bar{t}$ system: the semi-leptonic decay occurs four times more often than the di-leptonic decay (Section 2.2.3).

Cut 2 distinguishes between different lepton flavours. For each flavour approximately one third of the events are skimmed. This is in accordance with the branching ratios since the leptonic decay of the W boson into an electron happens as often as into a muon or a tau. In the following only the decay where electrons are involved is considered.

The last cut (cut 3) on parton level considers a bug of the data: in approximately 20% of the events the invariant mass of at least one of the decaying top quarks can not be correctly reconstructed on parton level. The top quark mass which follows from the invariant mass of the decay products is too small in these events. On parton level it is generated with a mass of exactly $175 \text{ GeV}/c^2$. Figure 6.1 (left plot) shows the reconstructed top quark mass before cut 3.

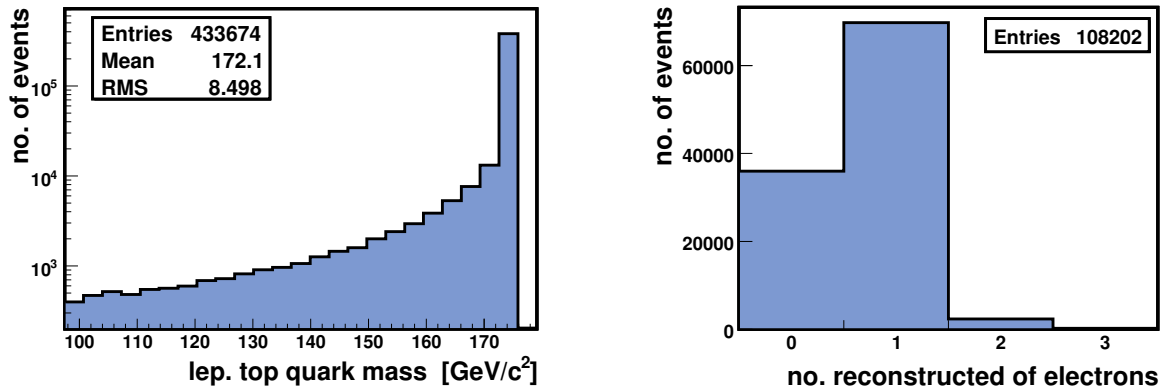


Figure 6.1.: Left: invariant mass of the leptonically decaying top quark where the bug of the invariant top quark mass is not fixed. The number of events on the y -axis is scaled logarithmically. Evidently, in approximately 20% of the events the top quark mass is too small. The top quark mass has been generated at exactly $175 \text{ GeV}/c^2$. Right: electron multiplicity reconstructed electrons. On parton level the events consist only of the semi-leptonic decay of a $t\bar{t}$ system where one electron is released. In about 33% of the events no electron is found in the detector and in approximately 65% (2%) of the events one (two) electrons are found in the reco data.

All events in which this bug occurs are rejected by claiming for the top quark mass m_t

$$|m_t - 175| [\text{GeV}/c^2] \stackrel{!}{\leq} 1 [\text{GeV}/c^2] \quad (6.40)$$

for both the hadronically and the leptonically decaying top quark.

With cut 1 to cut 3 a data sample of roughly 108,200 decaying $t\bar{t}$ pairs into $e + jets$ is created with an integrated luminosity corresponding to 43.4 pb^{-1} .

Selection cuts on reco data

Based on the data sample provided by MC cuts, cuts to the reco data must be performed in order to select the semi-leptonic decay channel from the detector signals.

Cut 4a selects events in which only one electron is detected. It is possible that either more than one electron is reconstructed or none. This is due to several effects: an electron can be taken as a jet. It can also happen that an electron is interpreted to be a part of a jet because it is located within the ΔR cone of the jet.

Furthermore, an electron can be radiated in the direction of the services. In all these cases no electron is detected. A jet can release electrons. If it happens that the jet is not reconstructed or that the electron is isolated, or a hadron of the jet is held for an electron (a pion for instance), an additional electron is counted. Figure 6.1 (right plot) shows the multiplicity of reconstructed electrons. No electron was found in approximately 33% of the events. In about 2% several electrons were reconstructed. 65% of the events pass selection cut 4a.

Cut 5a selects events with exactly four reconstructed jets in order to choose the semi-leptonic decay channel of the $t\bar{t}$ system. Due to e.g. ISR and FSR for instance the number of jets can be different from the number of hadronic partons in the final state of the hard scattering process. It can also happen that several jets can not be separated, that a jet propagates into the beam pipe or into the services or that the energy of a jet is too low to be reconstructed. The multiplicity of the reconstructed jets is plotted in Figure 6.2 (left), where the number of matched jets is colour-coded.

Cut 6a selects events in which all four jets are matched. This cut is applied only for studies in which the effect of ISR and FSR is neglected (Section 6.7).

Tight Cuts (TC)

Tight cut 4b to 6b are analogous to cut 4a to 6a. The aim is to enrich the resulting data sample with *events of interest*. Events of interest are four-jet events in which every jet is matched. In these events every jet comes directly from the semi-leptonic decay of a $t\bar{t}$ system. However, in an experiment the matching information does not exist and only the entire four-jet bin of Figure 6.2 (left plot) can be selected.

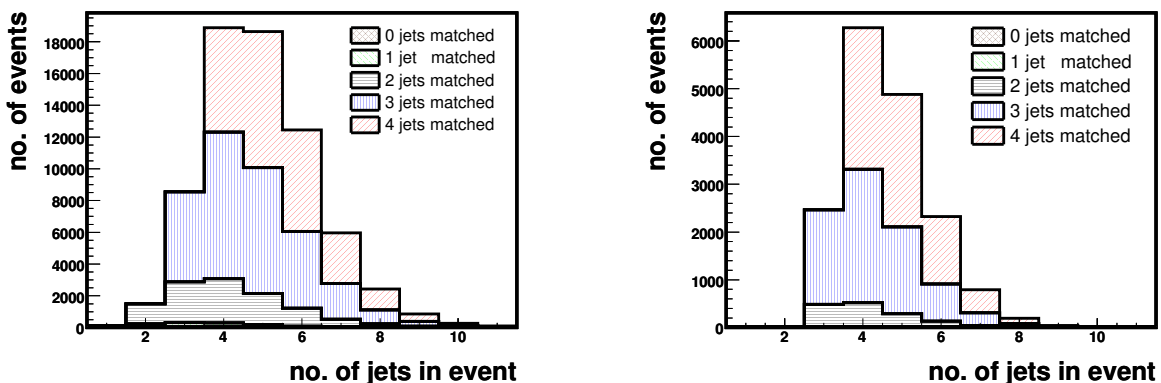


Figure 6.2.: Multiplicity of reconstructed jets. Due to ISR, FSR and various other reasons, in the detector one to 11 jets are reconstructed. The number of matched jets is colour-coded. Red, hatched ascending from right to left: four matched jets. Blue, hatched vertically: three matched jets. Black, vertically hatched: two matched jets. Green, hatched ascending from left to right: one matched jet. Brown, cross-hatched: no matched jet. Events marked in red are the events of interest because they contain all four jets coming directly from the semi-leptonic decay of a $t\bar{t}$ system. Left: multiplicity with loose cuts. In the four-jet bin the fraction of events in which all jets are matched is about $(35 \pm 1)\%$. Right: multiplicity with tight cuts. In the four-jet bin the fraction of events in which all jets are matched is approximately $(47 \pm 2)\%$. The error of the percentages is derived from Poisson statistics.

TCs are applied in order to increase the fraction of matched jets in the sample. The following TCs are chosen:

$$|\eta_{jet}| \leq 2.5 \quad (\text{for all jets}) \quad (6.41)$$

$$E_{jet} \geq 20 \text{ GeV} \quad (\text{for all jets}) \quad (6.42)$$

$$E_{jet} \geq 40 \text{ GeV} \quad (\text{for at least 3 jets}). \quad (6.43)$$

Note that these TCs are chosen according to the cuts proposed in the ATLAS CSC notes [62]. They are also suitable to separate the signal from background processes. Events which fulfill the TCs are called *good*. An event in which these requirements are not fulfilled is discarded. The TC efficiencies are shown in the relative percentage of cut *6b* (and *6a* for comparison) in Table 6.2. The fraction of events in which all four jets are matched is remarkably higher if TCs have been applied: with TCs roughly $(47 \pm 2)\%$, without approximately $(35 \pm 1)\%$. The multiplicity of reconstructed jets for events which pass the TCs is shown in Figure 6.2 (right).

6.3. Overview of the Performed Studies

The results of the KF are presented and discussed in the following. Diverse studies are performed:

- Investigation of the parameter space of the KF on a single event with and without constraints.
- Studies of the energy resolution of simulated measured and fitted energies.
- Combinatorial efficiencies considering the reconstruction of the decay topology of a $t\bar{t}$ system.
- b -tagging efficiencies of the KF.
- Reconstruction of the top quark mass from its decay products.
- Influence of a transverse momentum of the $t\bar{t}$ system to the KF.
- Result of the KF by fitting the transverse momentum of the $t\bar{t}$ system.
- Calibration of the JES for light quark and b quark jets separately by means of MC truth data.
- Investigation of the sensitivity of the KF for the JES for light quark and b quark jets separately.

The investigations are made separately for all three data sets described in the previous section. For the study of the parameter space of the Lagrange function, no distinction between the different input data is needed. The investigation of the JES is solely performed for the simulated ATLAS data, since this is the most realistic simulated set of data. Hence, a calibration of the calorimeter is only reasonable for those data.

6.4. Parameter Space of the Lagrange Function of a Single Event

The studies of the parameter space made in this section are valid for all used data samples. In this example one event of the ATLAS data sample is used. The parameter space of the Lagrange function (Equation (6.19)) is five-dimensional, one dimension for each energy parameter E_q , $E_{\bar{q}}$, $E_{b_{had}}$, $E_{b_{lep}}$ and E_{lep} . This parameter space can be visualised by varying two parameters while the others are fixed. As an example, Figure 6.3 (left) shows the value of the light- and light anti-quark jets for the χ^2 -terms of the Lagrange function (Equation (6.2)) as a function of the light quark jet energies. The smeared energy values of the light quark jets are marked as a peak.

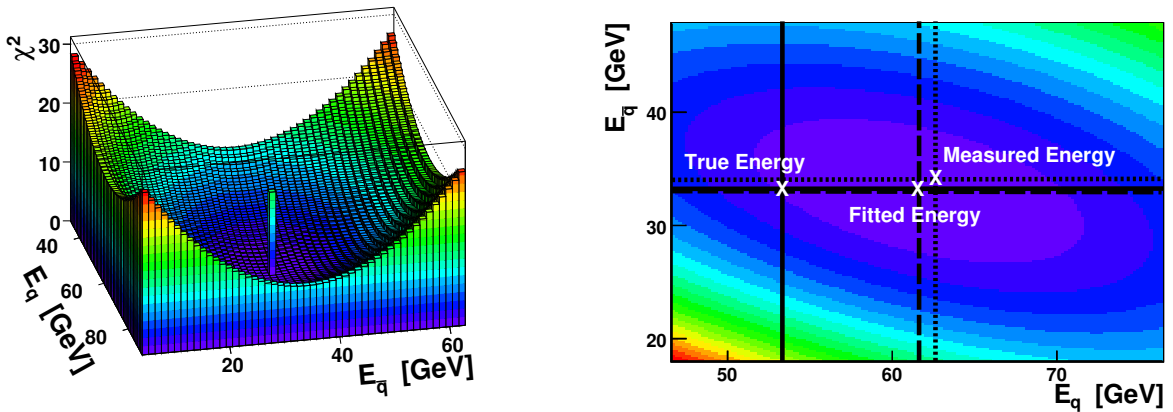


Figure 6.3.: Left: χ^2 -terms of the Lagrange function of a $t\bar{t}$ decay as a function of the two light quark jet energies for one single event. The energies of the other particles are fixed. The simulated measured energy value is marked as a peak. Right: value of the χ^2 -terms of the two light quark jets and of the first W -mass constraint as a function of the two light quark jet energies for a single event. Thereby the value of the Lagrange function is colour-coded. Solid line: fitted energy value. Dashed line: true energy value. Dotted line: measured energy value. The anti-correlation of the two energies of the photons E_q and $E_{\bar{q}}$ can be recognized.

The same observations as for the pion decay can be made: the parabolic character of the quadratic χ^2 -terms can be recognized in the shape of the plot in Figure 6.3 (left) and the Lagrange function depends stronger on the energy $E_{\bar{q}}$ with the smaller value.

The W -mass constraint for the light quarks is analogous to the π^0 mass constraint for the decaying pion. The Lagrange function including the W -mass constraint is shown in Figure 6.3 (right). The anti-correlation of the two light quark jet energies can be recognized. Furthermore, the fitted energy values are closer to the true energy values as the measured ones.

Including the equal-mass constraint leads to a difficulty: as described in Section 6.1 the energy of the neutrino must be reconstructed via the energies of the other particles. It can happen that the measured energy values result in a physically unreasonable neutrino, meaning that the discriminant D of the reconstruction of its z -momentum becomes negative (Equation (6.8)). The χ^2 method cannot be used on these events.

Furthermore, there is the possibility that a minimum of the Lagrange function is found for a set of parameter values which result in a physically unreasonable neutrino. Thus it must be ensured that regions of the five-dimensional parameter space in which no neutrino can be

reconstructed are avoided. This is done by a penalty term ψ in the Lagrange function:

$$\psi = \begin{cases} 0 & , D \geq 0 \\ -0.01 \cdot D & , D < 0. \end{cases} \quad (6.44)$$

It is essential for the convergence of the minimisation that the parameter space remains smooth, including the transition of physically reasonable regions to unreasonable regions. Therefore, for every set of parameter values within the minimisation of the Lagrange function, it is examined if the discriminant D for the solution of the z -momentum of the neutrino is positive or negative: if it is negative a number ψ is added which is proportional to the absolute value of the discriminant in order to prevent the Lagrange function to take its minimum for values which result in a physically unreasonable neutrino:

The Lagrange function including both the first W -mass constraint and the equal mass constraint, as well as the penalty term is plotted in Figure 6.4 (left) as a function of the light quark jet energies. The value of the discriminant is plotted in the same region in Figure 6.4 (right).

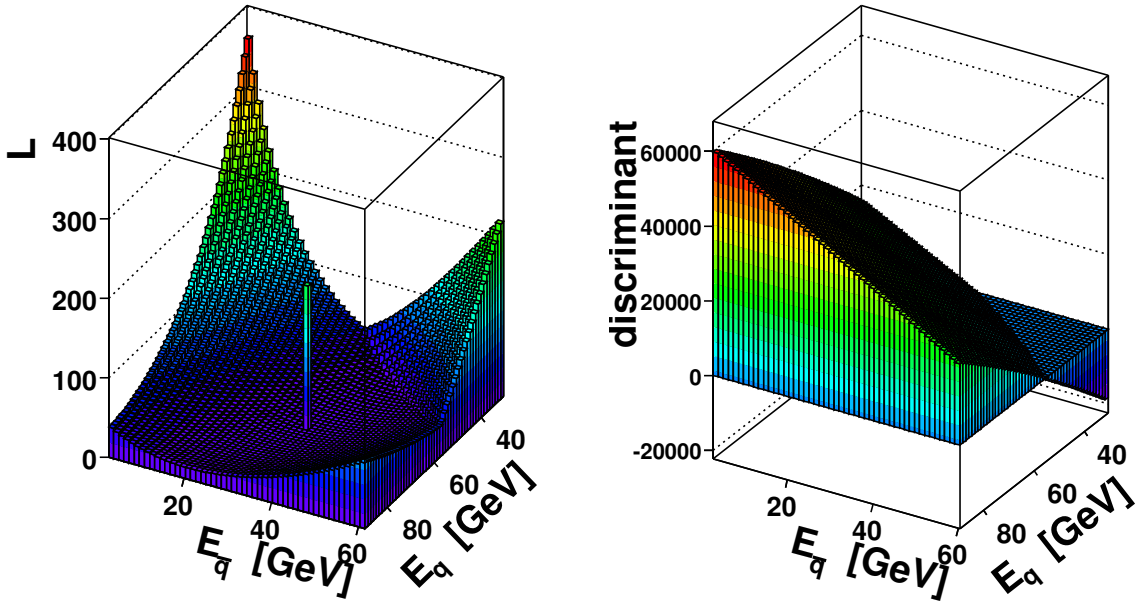


Figure 6.4.: Left: 3D-view of the value of the whole Lagrange function as a function of the light quark jet energies. Right: 3D-view of the value of the discriminant as a function of the light quark jet energies. If the value of the discriminant is negative, a factor which is proportional to it is added to the Lagrange function (compare with left plot). The parameter space of the Lagrange function is continuous which is essential to ensure the convergence of the minimisation.

In the 3D-view the smoothness of the contribution of the Lagrange function can be recognized. In this particular event, the discriminant becomes negative for small energies of E_q and large energies of $E_{\bar{q}}$ (right plot). Consequently, the penalty term contributes to the Lagrange function in this region. In Figure 6.4 in the right corner of the left plot this contribution can be recognized: a small kink indicates the transition from a physically reasonable region to an unreasonable region. However, this kink does not influence the convergence of the minimisation negatively. The crucial point is that the gradient of the Lagrange function in this physically not reasonable region points towards the minimum.

For small energies E_q and $E_{\bar{q}}$ (left corner of the left plot of Figure 6.4), there is no contribution of the penalty term because in this region the energies yield a physically reasonable neutrino solution. Compared to the right corner of this plot, the contribution of the penalty term is appropriate as it is from the same order of magnitude.

The number of events in which the minimisation does not converge is less than 1%. On the other hand, for less than 1% of the fitted events, no physically reasonable neutrino can be reconstructed. This percentage holds for all studies made with the KF.

6.5. Studies with the Kinematic Fit Using MadEvent Data – Gaussian smeared

In the following, the KF is applied to the MadEvent data sample which contains events only on parton level (Section 6.2.1). The simulated measured energy values are Gaussian smeared and labeled as *jets* because their energy resolution corresponds to the one of jets (Section 6.7.3). The motivation is to investigate the results of the KF with the same energy resolution which is assumed in the method (Section 4.1).

Studies of the energy resolution, combinatorial efficiencies, *b*-tagging, transverse momentum of the $t\bar{t}$ system and the top quark mass are mentioned the first time in the following. Therefore, they are discussed in more detail. Analogous investigations are performed in Section 6.6 and Section 6.7.

6.5.1. Studies of the Energy Resolution

In Figure 6.5 the energy resolution of the smeared and fitted energies of light quarks, b_{lep} and b_{had} are plotted. In Table 6.3 the results of Gaussian fits to the plots in Figure 6.5 are summarised.

Table 6.3.: Widths σ of the Gaussian fit to the energy resolutions of light quark and *b* quark jets. The widths of the measured values represent the characteristic energy resolution parameter of the detector. “Rel. impr.” denotes the relative improvement of the widths due to the fit. The errors are the errors of the width of the Gaussian fits.

object	σ' [GeV] ^{1/2}	σ^{fit} [GeV] ^{1/2}	rel. impr. [%]
lq jet	1.22 ± 0.01	1.031 ± 0.009	15.492 ± 0.010
b quark jet (lep)	1.406 ± 0.023	1.262 ± 0.018	10.242 ± 0.023
b quark jet (had)	1.42 ± 0.02	1.318 ± 0.020	7.183 ± 0.022

For both light quark and *b* quark jets the widths σ' of the distributions (left plots) are equal to the characteristic calorimeter parameters '*a*' which have been applied to the KF.

The energy resolution of the fitted energies (right plots) is also Gaussian distributed. Their widths are always smaller than the corresponding widths of the smeared data. Therefore, the fitted energies are on average closer to the true values than to the measured ones. Hence, the additional information of the constraints results in an improvement of the energy resolution.

The improvement of the energy resolution is larger for light quark jets compared to *b* quark jets. On the one hand, this is due to the fact that the light quark jets are influenced by both the first *W*-mass constraint and the equal mass constraint, whereas the *b* quark jets are only affected by the equal mass constraint. On the other hand, the *W*-mass constraint introduces an *absolute reference value* to the KF by the distinct value of the *W* boson pole mass.

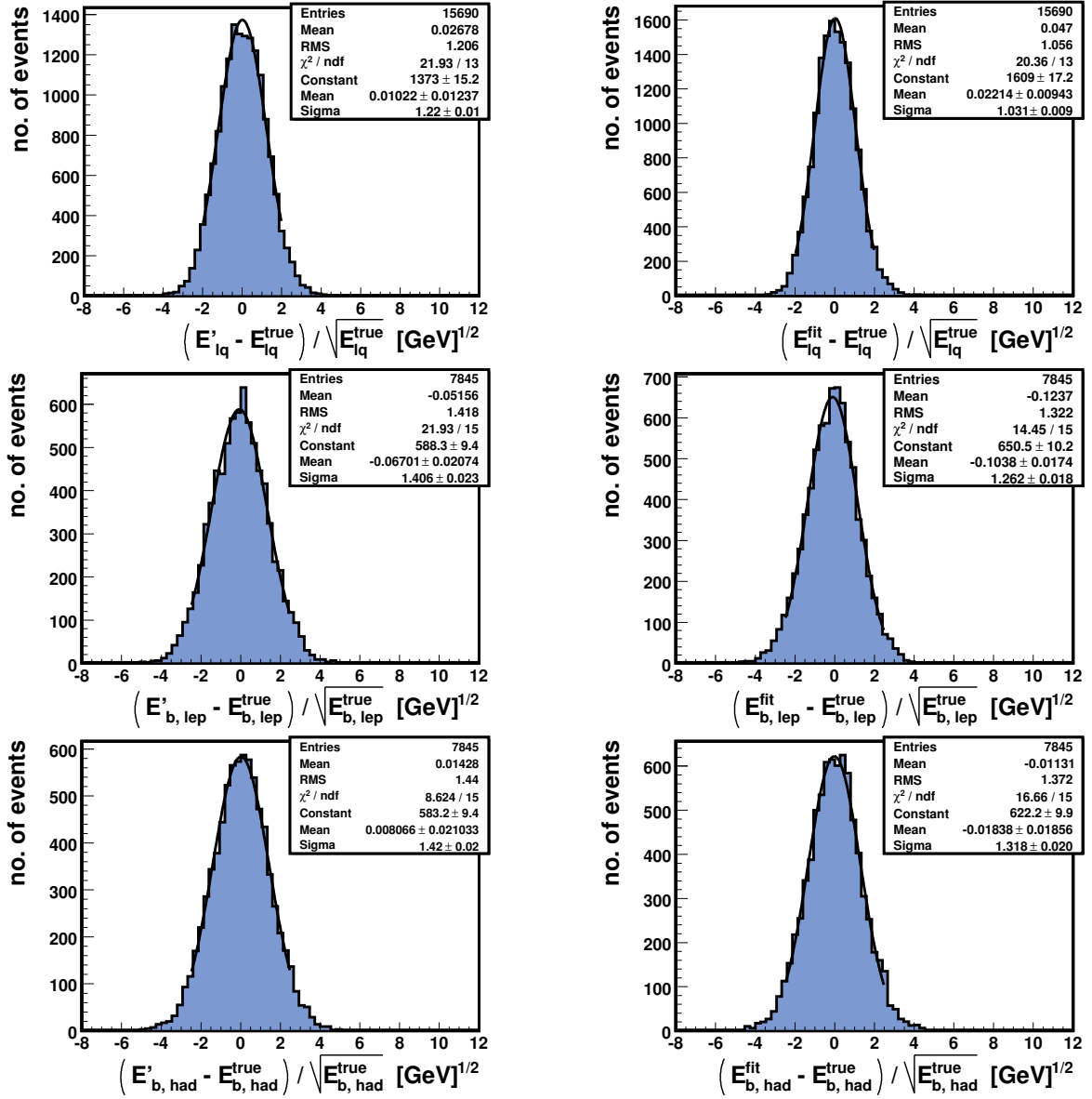


Figure 6.5.: Energy resolution of the jets coming from MC $t\bar{t}$ events of MadEvent data. Top: for light quark jets. Middle: for b quark jets from the leptonically decaying top quark. Bottom: b quark jets from the hadronically decaying top quark. On the left in each case: energy resolution of the smeared energy values. On the right in each case: energy resolution of the fitted energies.

In contrast, the equal mass constraint only demands the equality of the invariant mass of the two decayed top quarks without inserting an absolute value. This aspect is discussed in Section 6.7.2 in more detail.

The relative improvement of the energy resolution of b quark jets is different for jets, coming from leptonically decaying top quarks t_{lep} (11%), than for jets coming from the hadronically decaying top quarks t_{had} (7%). In this example a tendency which is true for all results of the KF can be recognized: the improvement of the energy resolution for b_{lep} ($\approx 10\%$) is always larger than for b_{had} ($\approx 7\%$). This is because within the reconstruction of the invariant mass of t_{lep} via the equal mass constraint, the energy of the lepton is involved.

This energy is measured with a much higher accuracy than the energies of the light quark jets from t_{had} . A large shift of the energy of b_{had} for instance can be balanced by the light quark jets. In contrast, a large shift of the energy of b_{lep} can not be balanced by the lepton. Therefore, the precisely measured lepton restrains more strongly the possible energy values E_{lep} , leading to a better energy resolution.

The latter effect can be observed for all results of the KF. However, in the following studies it is not distinguished between the fitted energies of b_{lep} and b_{had} , but only the energy resolution for all b quark jets is considered. This is because no new effect can be observed by a differentiation of the b quark jets.

6.5.2. Reconstruction of the Decay Topology of $t\bar{t}$ Events

The reconstruction of the decay topology of $t\bar{t}$ events happens via the assignment of the measured jets to the assumed partons. The aim is to find the correct jet combination.

The signature of a decaying $t\bar{t}$ system yields four jets (Section 2.2.3). The flavour of the measured jets is not known. Therefore, there are $4! = 24$ possibilities to pair jets and partons. No distinction of the light quark and anti-light quark is needed for the reconstruction of the invariant W boson mass. Thus $\frac{4!}{2} = 12$ jet combinations remain. The efficiency to find the correct combination by chance is hence $\frac{1}{12} \approx 8.3\%$. The correct combination is known for MC data. For each event, every permutation is fitted and the result which leads to the smallest value of the Lagrange function is taken as the estimated correct combination. Therefore, evaluating the Lagrange function for every jet assignment gives a handle on the reconstruction of the event topology. Table 6.4 summarises the result of the KF applied to MadEvent events.

Table 6.4.: Results of the KF applied to Gaussian smeared MadEvent data. “ ν -error” indicates the percentage of events which are rejected due to a physically unreasonable neutrino reconstruction (Section 6.1). $E_{ff}^{correct}$ stands for the fraction of the events in which all four jets of the $t\bar{t}$ decay are correctly assigned. $E_{ff}^{only\ had}$ ($E_{ff}^{only\ lep}$) is the percentage of the events in which only the hadronic (leptonic) hemisphere is correctly reconstructed. E_{ff}^{wrong} denotes the percentage of events which are completely wrongly reconstructed. The errors come from Poisson statistics.

ν -error [%]	$E_{ff}^{correct}$ [%]	$E_{ff}^{only\ had}$ [%]	$E_{ff}^{only\ lep}$ [%]	E_{ff}^{wrong} [%]
19.9 ± 2.5	56.8 ± 1.5	0.0 ± 0.0	16.8 ± 2.7	26.5 ± 2.2

As already mentioned in Section 6.1 the KF can not be accomplished if it is not possible to reconstruct a neutrino. Thus there is a percentage “ ν -error” of events which are instantly discarded. The fraction of events is about $(19.9 \pm 2.5)\%$.

In roughly 57% of the fitted events the correct jet combination is found from the evaluation of the value of the Lagrange function. This fraction is considerably larger than the fraction of 8.3% which is expected from a correct reconstruction by chance. Thus the restraint coming from the assumed decay topology of the $t\bar{t}$ system yields a positive influence for finding the correct jet assignment.

It is not possible to reconstruct only the hadronic hemisphere correctly (without all jet-parton combinations being correct) for MadEvent events, because *additional jets* coming from ISR and FSR are not simulated ($\Rightarrow E_{ff}^{only\ had} = 0\%$).

Thus if the three jets of the hadronic hemisphere are correctly assigned only the b quark jet of the leptonically decaying top quark remains and is ascribed to the leptonic hemisphere which results in an entirely correct reconstructed event. This is different for events in which ISR/FSR occurs (Section 6.7.4).

The fraction of events in which only the leptonic hemisphere is correctly reconstructed is $E_{\text{ff}}^{\text{only lep}} = (16.8 \pm 2.7)\%$. Consequently, the leptonic hemisphere can be reconstructed more often compared to the hadronic hemisphere.

In approximately 26% of the events, the topology of the $t\bar{t}$ decay is entirely wrongly reconstructed.

6.5.3. b -tagging Efficiencies

The identification of b quark jets (b -tagging) helps identifying decay signatures in which b quark jets are released. Methods have been established to perform b -tagging.

Since a jet assignment in the $t\bar{t}$ system is performed with the KF, it has the potential to identify b quark jets and can be used as a cross-check for other methods. If the topology is reconstructed correctly for instance the two b quark jets are correctly identified. However, for the b -tagging it is not required that the topology of a $t\bar{t}$ event is entirely correctly reconstructed. An event where the two b quark jets have been mixed up e.g., the event topology is wrongly reconstructed but the b -tagging is successful for the two released b quarks.

The b -tagging efficiency of the KF is influenced by the kinematics of the $t\bar{t}$ decay. The energy distribution of light quark jets and that of b quark jets is different (Figure 6.6). This is due to

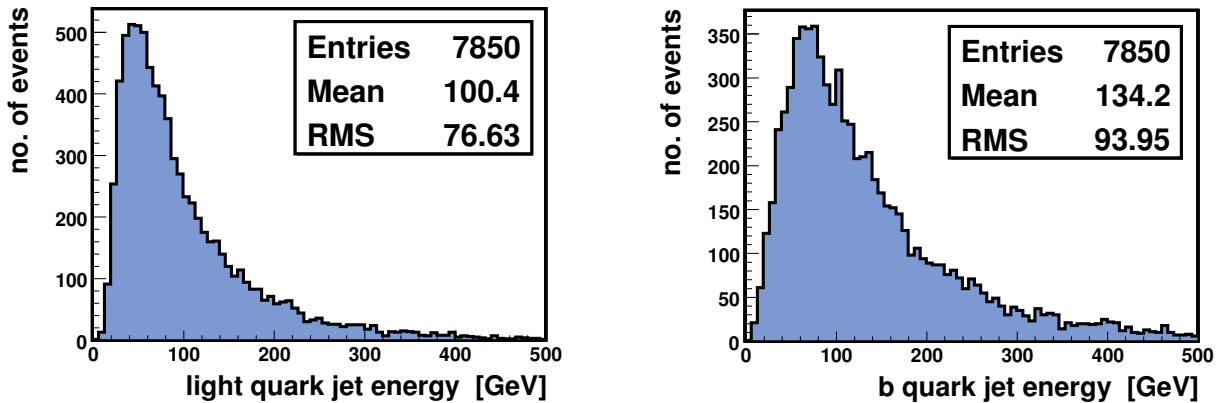


Figure 6.6.: Energy distributions of decay products of a $t\bar{t}$ system. Left: light quark jets. Right: b quark jets. Due to the decay topology the energy of b quark jets is on average larger.

the decay topology (Figure 2.6): the b quark and the W boson share the energy from the top quark decay. Finally, the two light quarks share the energy of the decaying W boson. Thus, on average, the b quarks have higher energies than the light quarks. Therefore, it is not likely to reconstruct the topology of a $t\bar{t}$ system where the two b quark jets are assigned to jets of the hadronic hemisphere, because the (on average higher) energy of the two b quark jets must be balanced by one of the remaining light quark jets for satisfying the equal mass constraint. Consequently, it is more likely that the b quark jets are mixed up with each other than assigned to a light quark jet. This effect positively affects the b -tagging efficiency because for the pure identification of the b flavour it is irrelevant if the two b quark jets are mixed up or not.

In Table 6.5 the b -tagging efficiency is presented for the same fit made in Section 6.5.2. $E_{\text{ff}}^{\text{b-tag}}$ indicates the percentage of fitted events in which a b quark jet is correctly identified to

Table 6.5.: b -tagging and combinatorial efficiencies of the KF for the Gaussian smeared MadE-event data. $E_{\text{ff}}^{\text{b-tag}}$ denotes the percentage how often a b quark jet is correctly identified to be one. “ $E_{\text{ff,b-had}}^{\text{correct}}$ ” (“ $E_{\text{ff,b-lep}}^{\text{correct}}$ ”) indicates the fraction of events in which the b quark jet of the hadronically (leptonically) decaying top quark is correctly assigned. For comparative reasons the efficiency for the complete reconstruction of the event topology is stated with $E_{\text{ff}}^{\text{correct}}$, too.

$E_{\text{ff}}^{\text{b-tag}}$ [%]	$E_{\text{ff,b-had}}^{\text{correct}}$ [%]	$E_{\text{ff,b-lep}}^{\text{correct}}$ [%]	$E_{\text{ff}}^{\text{correct}}$ [%]
82.0 ± 1.2	61.6 ± 1.4	73.5 ± 1.3	56.8 ± 1.5

be one. Additionally, “ $E_{\text{ff,b,had}}^{\text{combi}}$ ” and “ $E_{\text{ff,b,lep}}^{\text{combi}}$ ” are the fractions of events in which the b quark jet of the hadronically and leptonically decaying top quark are correctly assigned. For comparative reasons the combinatorial efficiency from Table 6.4 is denoted, too.

The b -tagging efficiency is about 82%. The b quark jet coming from the leptonically decaying top quark is more often correctly reconstructed ($(73.5 \pm 1.3)\%$) than the one coming from the hadronically decaying top quark ($(61.6 \pm 1.4)\%$). This is because a mis-assignment of b_{lep} is only possible by an interchange with one of the jets from the hadronic hemisphere. Due to kinematics this is not so likely as to interchange the hadronic b quark jet with a (hadronic) light quark jet, since the equal mass constraint demands that the two hemispheres of the hadronically and leptonically decaying top quark are balanced (Equation (6.3)).

However, compared to the efficiency of the entirely correct reconstruction of an event of roughly $E_{\text{ff}}^{\text{correct}} = 57 \pm 2\%$, the b -tagging efficiency is considerably higher. Thus, there are events in which the two b quark jets are interchanged and events in which only one b quark jet is correctly assigned.

6.5.4. Reconstruction of the Top Quark Mass

The reconstruction of the top quark mass is performed to investigate systematic effects of the KF (and not due to a physics analysis to estimate the value of its invariant mass). Every modification of the KF which changes the fit result (like the consideration of a transverse momentum of the $t\bar{t}$ system for instance, Section 6.5.5), also influences the reconstruction of the top quark mass because they depend on all fitted energy parameter.

The reconstructed invariant mass of hadronically decaying top quarks is shown in Figure 6.7 for a KF in which always the correct jet assignment is taken (left) and for a fit in which the correct jet assignment is estimated via the Lagrange function (right). For the latter plot the correctness of the reconstruction of the events is colour-coded.

In Table 6.6 the RMS value and the widths of a Gaussian fit to the peak of the plots in Figure 6.7 are summarised.

The effect of the combinatorial uncertainty can be studied comparing the latter two rows of Table 6.6. In events in which the wrong jet combination is taken, the top quark mass is on average reconstructed at a value which differs considerably from its pole-mass. From these events a *combinatorial background* is formed, causing a large increase of $\text{RMS}_{\text{had}}^{\text{top}}$. Thus on the one hand, the RMS value increases for the KF in which the correct jet assignment is chosen via the value of the Lagrange function due to the combinatorial background.

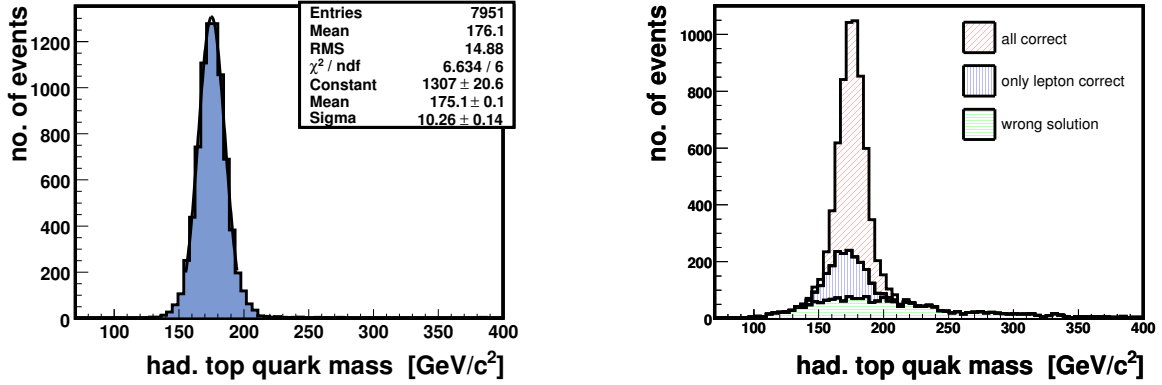


Figure 6.7.: Reconstructed invariant mass of the hadronically decaying top quark. For the reconstruction the fitted energies are taken (Section 6.5.2). Left: fit in which always the correct jet assignment is taken. Right: fit in the correct jet assignment is estimated via the Lagrange function. The correctness of the reconstruction of the events is colour-coded: red, hatched ascending from right to left: correct combination ($\approx 57\%$ of the events). Blue, hatched vertically: only the leptonic hemisphere is correctly reconstructed ($\approx 17\%$ of the events). Green, hatched horizontally: no hemisphere is correctly reconstructed ($\approx 26\%$ of the events).

Table 6.6.: Results of the reconstruction of the invariant mass of the hadronically decaying top quarks from the fitted energies. “Combi” denotes if the correct jet combinatorics has been taken or if it was estimated by the evaluation of the Lagrange function. $\sigma_{\text{top}}^{\text{had}}$ denotes the width of a Gaussian fit to the peak of the reconstructed top mass. $\text{RMS}_{\text{top}}^{\text{had}}$ is the RMS value of the histogram.

Combi.	$E_{\text{ff}}^{\text{correct}}$ [%]	$\sigma_{\text{top}}^{\text{had}}$ [GeV]	$\text{RMS}_{\text{top}}^{\text{had}}$ [GeV]
correct combi	100	10.26 ± 0.14	14.9
est. combi	56.8 ± 1.5	10.81 ± 0.17	35.2

On the other hand, the Gaussian fit to the peak of the reconstructed top quark mass is hardly affected by the combinatorial background – the correctly reconstructed events (red, hatched ascending from right to left) lead to a narrow mass peak around the pole mass of the top quark which has been generated at $175 \text{ GeV}/c^2$ (Section 6.2.1).

In Figure 6.7 (right) the blue events are events in which only the jet from the leptonic hemisphere is correctly assigned and the hadronic hemisphere is wrongly reconstructed. However, the reconstructed top quark mass of these event contributes to the peak and not to the background. This is because the invariant mass of t_{had} is not modified by the equal mass constraint if the jets of the hadronic hemisphere are interchanged – the invariant mass is independent of the permutation of the jets coming from the hadronically decaying top quark.

Nevertheless, the blue peak is slightly shifted to smaller energy values and a bit broader than the red peak of the completely correct reconstructed events. This is due to the influence of the first W mass constraint: one light quark jet is interchanged with b_{had} . As described in Section 6.5.3, the energy of a b quark jet is on average larger than the energy of a light quark jet.

Thus on average the energy of the wrongly assigned b quark jet is shifted to smaller values in order to fulfill the first W mass constraint which imposes an *absolute value* for the invariant mass of the W boson. This is because the peak of the events marked in blue is shifted to smaller masses.

6.5.5. Studies of the Transverse Momentum of the $t\bar{t}$ System

In general, $t\bar{t}$ pairs produced at the LHC have a transverse momentum $p_{t\bar{t},T}$ (Section 6.1). This transverse momentum directly affects the solution of the neutrino momentum (Equation 6.23) and thus influences the KF. In this section the influence of $p_{t\bar{t},T}$ and its fit via additional fit parameters $p_{t\bar{t},x}$ and $p_{t\bar{t},y}$ (Section 6.1) is investigated.

Figure 6.8 shows the $p_{t\bar{t},T}$ -distribution, resulting from the simulated ATLAS data. This distribution has also been applied to the MadEvent data, if a boost of the $t\bar{t}$ system is performed.

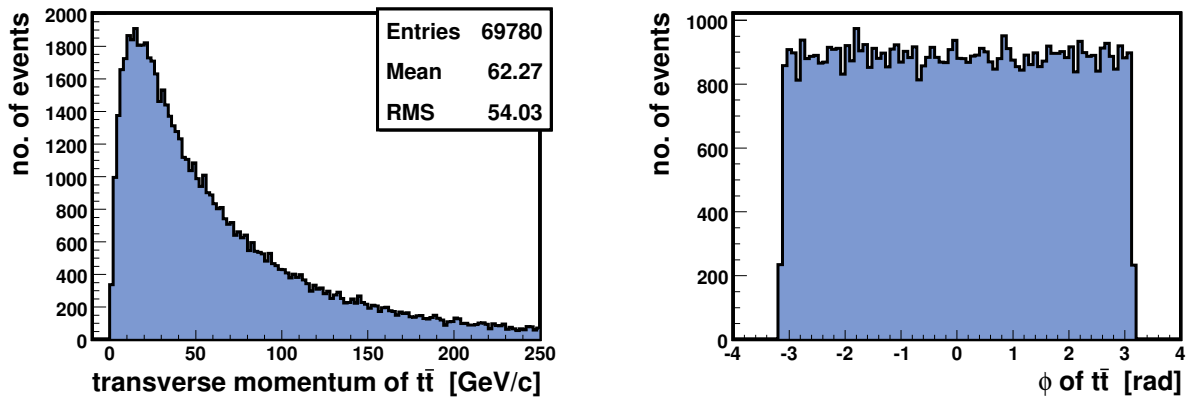


Figure 6.8.: Distribution of the transverse momentum of the $t\bar{t}$ system from simulated ATLAS data on parton level (with cut number 4b of Table 6.2). Left: transverse momentum. Right: distribution of the azimuthal angular ϕ .

The mean of the $p_{t\bar{t},T}$ -distribution is around 62 GeV (left plot). From the right plot the uniform distribution of transverse momentum on the x - y -plane is demonstrated. From these plots it can be recognized that in general, $p_{t\bar{t},T}$ is different from zero. Consequently, the consideration of the transverse momentum of the $t\bar{t}$ system within the KF is studied in the following. The effect of a $p_{t\bar{t},T}$ -boost according to the distribution shown in Figure 6.8 is investigated for a KF with different modifications. Two criteria (C) are modified:

- (C.1) The $t\bar{t}$ system has a transverse momentum (Boost-flg = 1) or not (Boost-flg = 0).
- (C.2) KF with ($p_{t\bar{t},T}$ -flg = 1) or without ($p_{t\bar{t},T}$ -flg = 0) a fit of $p_{t\bar{t},T}$.

Table 6.7 summarises the result of the KF in which criterion C.1 has been varied. For clarity, the single rows in which different configurations “Conf.” of criteria are chosen for the KF, are numbered.

Since the reconstructed top masses depend on all fitted energy parameter, they can be used as an indicator for investigating systematically effects of the KF.

Table 6.7.: Fit results of the KF for different modifications. “Conf.” denotes the configuration of the criteria which has been applied to the fit. The special case Conf. = MC means that as initial values for $p_{t\bar{t},x}$ and $p_{t\bar{t},y}$ the MC values are taken. If $p_{t\bar{t},T}$ -flag = 1 also a fit of the transverse momentum $p_{t\bar{t},T}$ of the $t\bar{t}$ system is performed (described in Section 6.1). If Boost-flag = 1 the $t\bar{t}$ system is boosted via the $p_{t\bar{t},T}$ distribution of the simulated ATLAS data (Figure 6.8). “ ν -error” indicates the percentage of events which are rejected due to a physically unreasonable neutrino reconstruction (Section 6.1). $E_{\text{ff}}^{\text{correct}}$ stands for the percentage of the events in which the correct jet combination is found. $\text{RMS}_{\text{had}}^{\text{top}}$ and $\text{RMS}_{\text{lep}}^{\text{top}}$ give the RMS value for the reconstructed hadronically and leptonically decaying top quark masses, whereas $\sigma_{\text{had}}^{\text{top}}$ and $\sigma_{\text{lep}}^{\text{top}}$ is the width of a Gaussian fit around the respective top mass peak.

Conf.	$p_{t\bar{t},T}$ - flag	Boost- flag	ν -error [%]	$E_{\text{ff}}^{\text{correct}}$ [%]	$\sigma_{\text{had}}^{\text{top}}$ [GeV]	$\text{RMS}_{\text{had}}^{\text{top}}$ [GeV]	$\sigma_{\text{lep}}^{\text{top}}$ [GeV]	$\text{RMS}_{\text{lep}}^{\text{top}}$ [GeV]
1	0	0	19.9 ± 2.5	56.8 ± 1.5	10.8 ± 0.2	35.2	11.0 ± 0.2	34.4
2	0	1	26.0 ± 2.3	54.5 ± 1.6	11.2 ± 0.2	37.7	13.0 ± 0.3	37.5
MC	0	1	18.8 ± 2.6	57.5 ± 1.5	11.0 ± 0.2	34.7	10.9 ± 0.2	35.0

In particular the leptonically decaying top quark depends directly on the reconstructed neutrino momentum, whereas the hadronically decaying top quark is only affected by the neutrino momentum via the equal mass constraint. Therefore, effects considering $p_{t\bar{t},T}$ influence especially the leptonic hemisphere (Equation (6.23)).

Comparing Conf. 1 with Conf. 2, the percentage ν -error increases if a $p_{t\bar{t},T}$ -boost is applied. Since the transverse momentum is not considered in the KF of these configurations, the initial values for $p'_{t\bar{t},x}$ and $p'_{t\bar{t},y}$ are zero, regardless if a $p_{t\bar{t},T}$ -boost is performed or not. Thus if a $p_{t\bar{t},T}$ -boost is accomplished, but no transverse momentum is taken into account, a conceptual bias is inserted into the (initial) reconstruction of the neutrino. Therefore, on average the neutrino can not so often be reconstructed if a $p_{t\bar{t},T}$ -boost is comprised within the KF. This tendency is true for all investigations which include a transverse boost of the $t\bar{t}$ system.

The $p_{t\bar{t},T}$ -boost worsens the fit results: the efficiency to correctly reconstruct the event topology decreases from $(56.8 \pm 1.5)\%$ to $(54.5 \pm 1.6)\%$, whereas the reconstruction of the top quark masses shows a larger uncertainty ($\sigma_{\text{lep}}^{\text{top}} = (13.0 \pm 0.3)$ GeV instead of $\sigma_{\text{lep}}^{\text{top}} = (11.0 \pm 0.2)$ GeV without boost, for instance). Thereby, the increase of σ^{top} mainly affects the leptonic hemisphere. This can be explained by the weak link between the leptonic and hadronic hemisphere via the equal mass constraint. The value of $\sigma_{\text{had}}^{\text{top}}$ is only weakly affected by the $p_{t\bar{t},T}$ -boost because it influences only the reconstructed neutrino of the leptonic hemisphere.

To illustrate the effect of the bias due to an additional $p_{t\bar{t},T}$ -boost, Conf. MC is added to Table 6.7. In Conf. 1 no $p_{t\bar{t},T}$ -boost is applied. Thus no wrong assumption is made by claiming $p_{t\bar{t},x} = p_{t\bar{t},y} = 0$ in contrast to Conf. 2 where a boost is performed. In Conf. MC a $p_{t\bar{t},T}$ -boost is applied as well, but for the transverse momentum initial values $p_{t\bar{t},x}^{\text{true}}$ and $p_{t\bar{t},y}^{\text{true}}$ are used which are known from MC data. Therefore, Conf. MC does not contain this bias because no wrong assumption is made for the values $p_{t\bar{t},x}$ and $p_{t\bar{t},y}$. Consequently, the results of Conf. MC are similar to the ones of Conf. 1, although in this configuration a $p_{t\bar{t},T}$ -boost is applied analogous to Conf. 2.

To counteract the bias coming from disregarding the transverse momentum of the $t\bar{t}$ system within the KF, $p_{t\bar{t},x}$ and $p_{t\bar{t},y}$ are introduced as new fit parameters (Section 6.1). Nevertheless, the initial values $p'_{t\bar{t},x}$ and $p'_{t\bar{t},y}$ are set to zero, regardless if a $p_{t\bar{t},T}$ -boost is performed or not.

Note that this conceptual bias does not result from a wrong application of the Method, but from the fact that for fitting $p_{t\bar{t},T}$ two parameters are included into the KF for which no initial value exist. Consequently, a bias can not be avoided due to the concept of the χ^2 method itself. The assumption $p'_{t\bar{t},x} = p'_{t\bar{t},y} = 0$ is the best one which can be made. Any other value which differs from zero would mark out a certain direction which introduces a worse systematical bias. Describing the transverse momentum of the $t\bar{t}$ system via the two coordinates $p_{t\bar{t},T}$ and $\phi_{t\bar{t},T}$ does not change the result. This is because both descriptions are equivalent due to the one-to-one transformation

$$p_{t\bar{t},T} = \sqrt{p_{t\bar{t},x}^2 + p_{t\bar{t},y}^2}, \quad (6.45)$$

$$\phi_{t\bar{t},T} = \begin{cases} \arccos\left(\frac{p_{t\bar{t},x}}{p_{t\bar{t},T}}\right) & , p_{t\bar{t},y} \geq 0 \\ -\arccos\left(\frac{p_{t\bar{t},x}}{p_{t\bar{t},T}}\right) & , p_{t\bar{t},y} < 0. \end{cases} \quad (6.46)$$

Assuming a certain $p_{t\bar{t},T}$ unlike zero in these coordinates would also mark out a certain direction because a particular angular $\phi_{t\bar{t},T}$ is to be taken.

Table 6.8 summarises results analogous to the results of Table 6.7 which are obtained if the fit of $p_{t\bar{t},x}$ and $p_{t\bar{t},y}$ is added to the KF (criterion C.2).

Table 6.8.: Fit results of the KF for different modifications analogous to Table 6.7. Here, also a fit of $p_{t\bar{t},T}$ has been applied.

Conf.	$p_{t\bar{t},T}$ - flag	Boost- flag	ν -error [%]	$E_{\text{ff}}^{\text{correct}}$ [%]	$\sigma_{\text{had}}^{\text{top}}$ [GeV]	$\text{RMS}_{\text{had}}^{\text{top}}$ [GeV]	$\sigma_{\text{lep}}^{\text{top}}$ [GeV]	$\text{RMS}_{\text{lep}}^{\text{top}}$ [GeV]
3	1	0	19.9 ± 2.5	43.7 ± 1.7	12.7 ± 0.3	45.4	13.8 ± 0.4	50.2
4	1	1	26.0 ± 2.4	44.0 ± 1.8	12.3 ± 0.3	45.9	14.8 ± 0.5	49.6
MC	1	1	18.8 ± 2.5	43.7 ± 1.7	12.6 ± 0.3	45.8	13.5 ± 0.4	49.7

The introduction of the new fit parameters worsens the fit results. Comparing Conf. 1 with Conf. 3 clearly points this out: in both configurations no $p_{t\bar{t},T}$ -boost is applied but in the latter one a fit of the transverse momentum is performed. The new freedom of the KF to vary two more fit parameters leads to the effect, that the event topology is more often wrongly reconstructed. Thus, more events contribute to the combinatorial background and the RMS value increases.

Comparing Conf. 3 with Conf. 4 similar tendencies can be recognized as from comparison of Conf. 1 with Conf. 2: ν -error increases if a $p_{t\bar{t},T}$ -boost is performed while σ^{top} increases in particular for the leptonically decaying top quark. However, the RMS values and the combinatorial efficiency show no systematic tendency because the bias from the new fit parameters worsens the result too strongly. This aspect is also emphasized regarding the result of Conf. MC. Although the use of the correct values $p_{t\bar{t},x}^{\text{true}}$ and $p_{t\bar{t},y}^{\text{true}}$ eliminates the bias of wrong initial values for the transverse momentum (the decrease of ν -error points this out), no improvement of the combinatorial efficiency can be observed.

The decrease of $E_{\text{ff}}^{\text{correct}}$ of roughly 13% if a $p_{t\bar{t},T}$ -boost is performed, is due to the permutation of the two b quark jets. This can be shown by considering separately the efficiency of the correct reconstruction of b_{lep} and b_{had} , compared to the b -tagging efficiency $E_{\text{ff}}^{\text{b-tag}}$ and the efficiency $E_{\text{ff}}^{\text{correct}}$ of the correct event reconstruction. In Table 6.9 these efficiencies are summarised for Conf. 1 and Conf. 3.

Table 6.9.: Combinatorial and b -tagging efficiencies of the KF for different modifications. “Conf.”, “ $E_{\text{ff}}^{\text{correct}}$ ” and the flags are defined as in Table 6.7. “Had. correct” (“Lep. correct”) indicates the percentage of fitted events in which the b quark jet of the hadronically (leptonically) decaying top quark is correctly assigned. $E_{\text{ff}}^{\text{b-tag}}$ denotes the percentage of fitted events in which a b quark jet is correctly identified.

Conf.	$p_{t\bar{t},T^-}$ flg	Boost- flg	$E_{\text{ff}}^{\text{correct}}$ [%]	$E_{\text{ff,b,had}}^{\text{correct}}$ [%]	$E_{\text{ff,b,lep}}^{\text{correct}}$ [%]	$E_{\text{ff}}^{\text{b-tag}}$ [%]
1	0	0	56.8 ± 1.5	61.6 ± 1.4	73.5 ± 1.3	82.0 ± 1.2
3	1	0	43.7 ± 1.7	49.9 ± 1.6	57.0 ± 1.5	79.4 ± 1.3

The efficiency of the correct reconstruction of b_{lep} decreases stronger than of the b quark jet of the hadronic hemisphere:

$$\Delta E_{\text{ff,b,had}}^{\text{correct}} = (11.7 \pm 1.6)\%, \quad (6.47)$$

$$\Delta E_{\text{ff,b,lep}}^{\text{correct}} = (16.5 \pm 1.5)\%. \quad (6.48)$$

However the b -tagging efficiency decreases only marginal:

$$\Delta E_{\text{ff}}^{\text{correct}} = (2.6 \pm 1.3)\%. \quad (6.49)$$

This is due to the fact that in particular a permutation of the two b quark jets takes place. On the assumption that in all events in which b_{had} is wrongly reconstructed, b_{had} and b_{lep} have been mixed up, there remain $\Delta E_{\text{ff,b,lep}}^{\text{correct}} - \Delta E_{\text{ff,b,had}}^{\text{correct}} = (4.8 \pm 1.6)\%$ of events in which only b_{lep} is not correctly reconstructed. Thus due to this effect $E_{\text{ff}}^{\text{correct}}$ decreases for a few percent: $\frac{4.8 \pm 1.6}{2}\% = (2.4 \pm 0.8)\% \approx \Delta E_{\text{ff}}^{\text{correct}}$. Thereby, the factor $\frac{1}{2}$ results from the fact that in these events b_{lep} was not correctly reconstructed, but b_{had} , such that one of two b quark jets of the event is successfully b -tagged.

6.6. Studies with the Kinematic Fit Using MadEvent Data – ATLAS Smeared

For the following, the KF is applied on the MadEvent data sample with simulated measured energies which are smeared according to the energy resolution of simulated ATLAS data (Section 6.7.3). The motivation is to investigate the effect of a non-Gaussian energy resolution, in particular tails. The studies presented here are analogous to the studies presented in Section 6.5. Therefore, especially the differences of the results are discussed.

6.6.1. Studies of the Energy Resolution

Figure 6.9 shows the energy resolution of the simulated measured and fitted energies for light quark and b quark jets separately.

Table 6.10 summarises the result of the Gaussian fit to the peaks of the energy resolutions.

In principle all tendencies investigated in Section 6.5.1 (Table 6.3) can be recognized. The relative improvement of the light quark energy resolution ($\approx 13\%$) for instance is larger than of the b quark jets ($\approx 9\%$). However, due to the asymmetry of the energy distribution, the absolute values decreased compared to the results of Gaussian-like smeared energies.

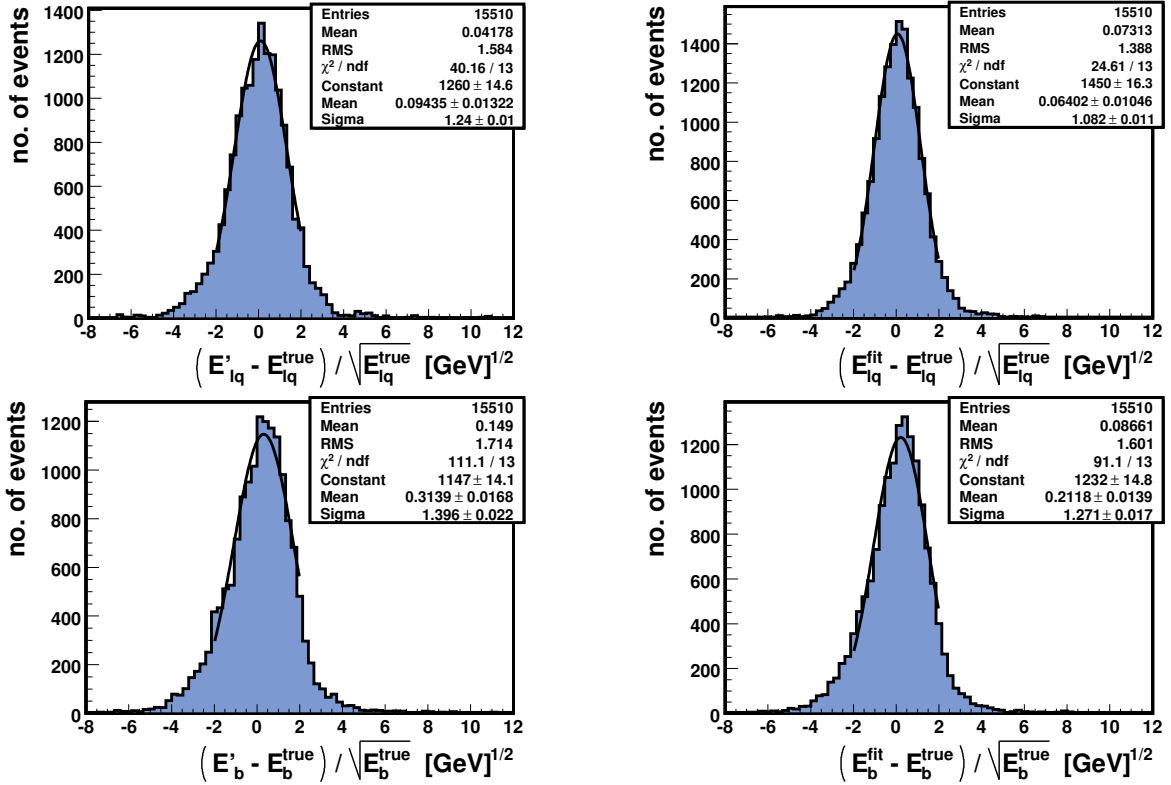


Figure 6.9.: Energy resolution of MadEvent data where the simulated measured energies are smeared according to the energy resolution of simulated ATLAS data. Top: for light quark jets. Bottom: for b quark jets. Left: for the measured energies. Right: for the fitted energies.

Table 6.10.: Widths σ of the Gaussian fit to the energy resolutions of light quark and b quark jets. The widths of the measured values represent the characteristic energy resolution parameter of the detector. “Rel. impr.” denotes the relative improvement of the width due to the fit. The errors are the errors of the mean of the Gaussian fits.

object	$\sigma' [GeV]^{1/2}$	$\sigma^{\text{fit}} [GeV]^{1/2}$	rel. impr. [%]
lq jet	1.24 ± 0.01	1.082 ± 0.011	12.74 ± 0.01
b quark jet	1.396 ± 0.022	1.271 ± 0.017	8.95 ± 0.02

This points out that the non-Gaussian tails of the energy distribution lead to a consequent worsening of all results of the KF: the widths of the fitted energies are always broader if the applied energy resolution has non-Gaussian tails.

6.6.2. Reconstruction of the Decay Topology of $t\bar{t}$ Events

The combinatorial efficiencies are investigated analogous to Section 6.5.2. The results are summarized in Table 6.11.

Compared to the results of Section 6.5.2, ν -error and $E_{\text{ff}}^{\text{correct}}$ decrease by roughly 2% and 11% respectively, while $E_{\text{ff}}^{\text{only lep}}$ and $E_{\text{ff}}^{\text{wrong}}$ increase by approximately 4% and 8%.

Table 6.11.: Results of the KF applied to Gaussian smeared MadEvent events. “ ν -error” indicates the percentage of events which are rejected due to a physically unreasonable neutrino reconstruction (Section 6.1). $E_{\text{ff}}^{\text{correct}}$ stands for the percentage of the events in which all four jets of the $t\bar{t}$ decay are correctly assigned. $E_{\text{ff}}^{\text{only had}}$ ($E_{\text{ff}}^{\text{only lep}}$) is the percentage of the events in which only the hadronically (leptonically) hemisphere is correctly reconstructed. $E_{\text{ff}}^{\text{wrong}}$ denotes the percentage of events which are completely wrong reconstructed. The error comes from Poisson statistics.

ν -error [%]	$E_{\text{ff}}^{\text{correct}}$ [%]	$E_{\text{ff}}^{\text{only had}}$ [%]	$E_{\text{ff}}^{\text{only lep}}$ [%]	$E_{\text{ff}}^{\text{wrong}}$ [%]
22.3 ± 2.4	45.5 ± 1.7	0.0 ± 0.0	20.5 ± 2.5	34.1 ± 2.0

Thus the efficiency for the correct reconstruction of the event topology is worsened by the non-Gaussian tails of the energy resolution. Therefore, the assumption of a Gaussian distribution of the energy resolution causes a bias of the KF.

However, the efficiency of the correct reconstruction of only the leptonic hemisphere increases by a few percent. This is due to the fact that in events, which have been completely correctly reconstructed in Section 6.5.2, the jets of the hadronic hemisphere are wrongly assigned while for the leptonic hemisphere the chance of a correct reconstruction still exists. Consequently, the absolute number of events in which a correct reconstruction of the leptonic hemisphere is possible is larger compared to the results of Section 6.5.2.

Since the only difference of the studies of the KF made in Section 6.5.2 is the implementation of non-Gaussian energy resolution, the worsening of the correct reconstruction of the entire event topology can thus be explained.

6.6.3. b -tagging Efficiencies

The b -tagging is investigated analogous to Section 6.6.3. Table 6.12 shows the result of the b -tagging and combinatorial efficiency of the KF applied to the MadEvent data which has been smeared which an energy resolution according to the simulated ATLAS data.

Table 6.12.: b -tagging and combinatorial efficiencies of the KF for the MadEvent data smeared according the simulated ATLAS data. This table is analogous to Table 6.5

$E_{\text{ff}}^{\text{b-tag}}$ [%]	$E_{\text{ff,b-had}}^{\text{correct}}$ [%]	$E_{\text{ff,b-lep}}^{\text{correct}}$ [%]	$E_{\text{ff}}^{\text{correct}}$ [%]
75.7 ± 1.3	51.8 ± 1.9	66.0 ± 1.4	45.5 ± 1.7

The efficiencies are smaller compared to those of Section 6.5.3: the b -tagging efficiency decreases by roughly 6% and the combinatorial efficiency by approximately 11%. Hence, the b -tagging efficiency is not so strongly affected by the non-Gaussian energy distribution as the combinatorial efficiency. This is due to the fact that there are events in which the two b quark jets of the $t\bar{t}$ decay are interchanged. These events are correctly b -tagged but not correctly reconstructed in terms of the event topology.

6.6.4. Reconstruction of the Top Quark Mass

Since in Section 6.5.4 the combinatorial background is discussed in detail, here only the differences of analogous results are presented.

In Table 6.13 the width of a Gaussian fit to the peak of the reconstructed invariant top quark mass and the RMS value are shown for the KF in which the correct jet combination is taken and for the KF in which the correct combination is estimated via the Lagrange function.

Table 6.13.: Results of the reconstruction of the invariant mass of hadronically decaying top quarks from the fitted energies. This table is analogous to Table 6.6.

Combi – flg.	$E_{\text{ff}}^{\text{correct}}$ [%]	$\sigma_{\text{top}}^{\text{had}}$ [GeV]	$\text{RMS}_{\text{top}}^{\text{had}}$ [GeV]
0	100	11.1 ± 0.2	17.3
1	45.5 ± 1.7	12.0 ± 0.3	39.8

Though, due to the non-Gaussian distributed energy resolution, the absolute values of the widths and RMS values increase. Compared to Table 6.6 the same tendencies of the results can be recognized. The bias coming from the assumption of a Gaussian-like energy resolution thus causes a worsening of the reconstruction of the invariant top quark mass.

6.6.5. Studies of the Transverse Momentum of the $t\bar{t}$ System

For comparison of the studies of the transverse momentum of the $t\bar{t}$ system made in Section 6.5.5, here the corresponding results are summarised in Table 6.14.

Table 6.14.: Fit results of the KF for different modifications analogous to Table 6.7 and Table 6.8.

Conf.	$p_{t\bar{t},T^-}$ flg	Boost-flg	ν -error [%]	$E_{\text{ff}}^{\text{correct}}$ [%]	$\sigma_{\text{had}}^{\text{top}}$ [GeV]	$\text{RMS}_{\text{had}}^{\text{top}}$ [GeV]	$\sigma_{\text{lep}}^{\text{top}}$ [GeV]	$\text{RMS}_{\text{lep}}^{\text{top}}$ [GeV]
1	0	0	22.3 ± 2.4	45.5 ± 1.7	12.0 ± 0.3	39.8	13.2 ± 0.4	39.6
2	0	1	28.0 ± 2.4	43.8 ± 1.9	13.6 ± 0.4	42.3	15.8 ± 0.6	42.6
3	1	0	22.3 ± 2.2	34.8 ± 1.8	13.7 ± 0.4	48.1	17.1 ± 0.8	51.8
4	1	1	28.0 ± 2.2	34.9 ± 2.0	14.6 ± 0.5	49.1	18.8 ± 1.1	41.6

This Table is analogous to Table 6.7 and Table 6.8 – the same tendencies can be recognized which are discussed in Section 6.5.5 in detail. However, all results are worsened. Since the only difference of the studies made in Section 6.5.5 is the implementation of a non-Gaussian energy resolution, the worsening of the results can thus be explained.

6.7. Studies with the Kinematic Fit Using Simulated ATLAS Data

The data of the MC@NLO generated sample are miscalibrated. Since it is intended to investigate systematically the sensitivity of the method for the JES, beforehand a calibration of the calorimeter is necessary. All JES studies are performed for light quark and b quark jets separately.

The studies made in the following are analogous to the studies presented in the previous sections. Due to the fact that the ATLAS data is simulated as realistic as possible the generated $t\bar{t}$ pairs are boosted on parton level. Hence, investigations of unboosted $t\bar{t}$ systems are omitted.

6.7.1. JES – Calibration

The calibration of the hadronic calorimeter is realised using true energy values of the simulated data. The motivation is to ensure a correctly calibrated calorimeter before varying the JES systematically. To ensure that the calibration is not biased by a wrong jet identification, the correct jet assignment has been chosen using MC data. All studies in which the simulated ATLAS data sample is used are based on the *calibrated* data.

If the detector is correctly calibrated the mean μ of the ratio of the measured energy values and the true energy values $\mu\left(E'/E^{true}\right) \approx 1$ is expected to peak around one. Figure 6.10 shows this ratio for light quark (left) and b quark jets (right) separately before calibration. The energy

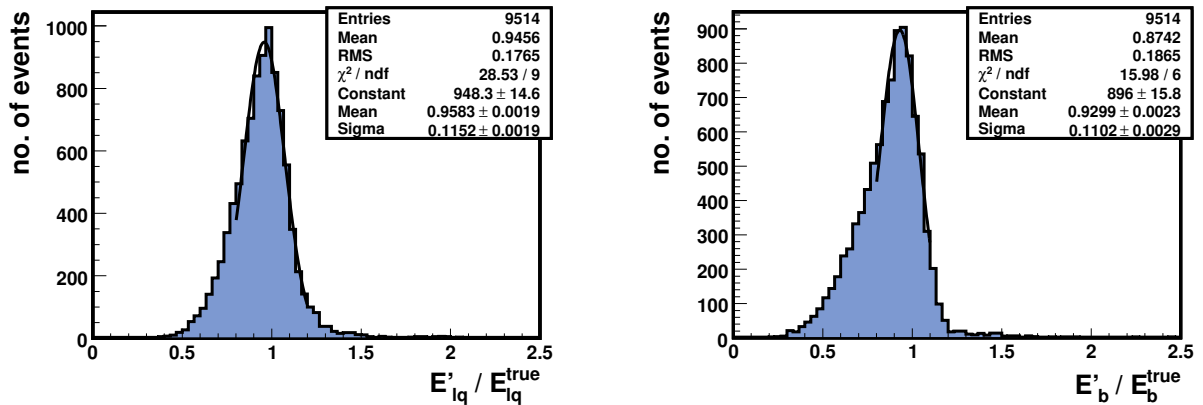


Figure 6.10.: Ratio $\frac{E'}{E^{true}}$ of uncalibrated energies. Left: for light quarks. Right: for b quarks. The peaks are significantly shifted from one.

distribution of b quark jets shows a larger asymmetric tail. This is due to the fact that there are additional effects for b quark jets which result in a lower measured energy (Section 6.7.3). The peaks of the distributions are significantly shifted from one:

$$\mu_{lq}\left(E'_q/E_q^{true}\right) = 0.9583 \pm 0.0019 \quad (6.50)$$

$$\mu_b\left(E'_b/E_b^{true}\right) = 0.9299 \pm 0.0023. \quad (6.51)$$

The measured energy is too small on average. For a calibration this shift must be reversed depending on the energy. For energy intervals of 7 GeV distributions of the difference $(E' - E^{true})$ have been plotted.

Therefrom, the systematic deviation of the measured energy values from the true energy values is pointed out. A Gaussian fit to the peak yields the mean μ of these distributions. In Figure 6.11 the mean of these distributions is plotted as a function of the true energy for light quark and b quark jets separately. The error comes from the error of the mean from the Gaussian fits and increases with a decreasing number of events in a bin which is especially for higher energies the case.

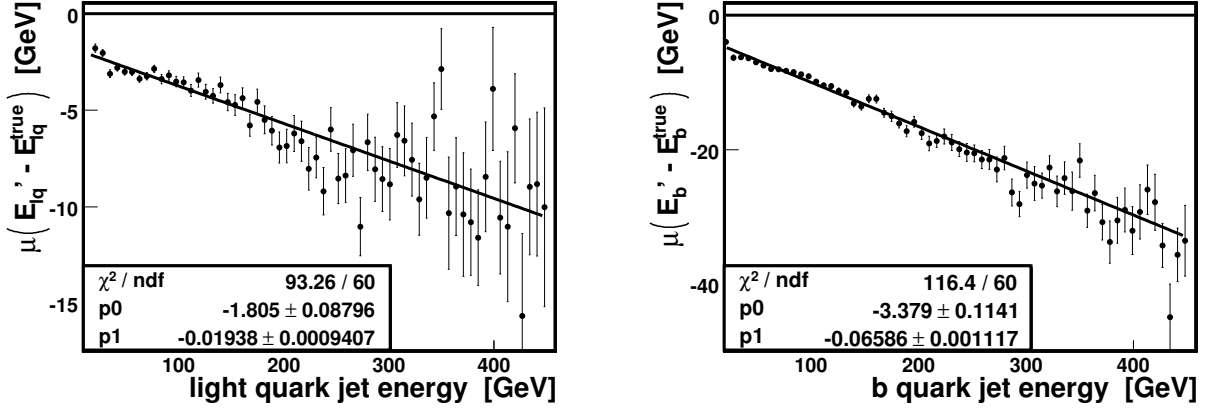


Figure 6.11.: Mean of a Gaussian fit around the peak of the distributions of $(E' - E^{true})$ as a function of the true energy. Left: for light quarks. Right: for b quarks.

A linear model is taken as a simple parametrization for the dependency of $\mu(E' - E^{true})$ as a function of the energy E^{true} . The coefficients of a linear fit to the plot in Figure 6.11 yield a possibility to calibrate the calorimeter response for light quark and b quark jets separately. For the calibrated energies E^{calib} it is

$$E_q^{calib} = a \cdot E'_q + b, \quad a := 1.01938 \pm 0.00094, \quad b := 1.805 \pm 0.009 \quad (6.52)$$

$$E_b^{calib} = a \cdot E'_b + b, \quad a := 1.06586 \pm 0.00112, \quad b := 3.379 \pm 0.114. \quad (6.53)$$

Using Equation (6.52) and Equation (6.53) to calibrate all jet energies, the energy resolution for light quark and b quark jets peaks around one within their errors (Figure 6.12).

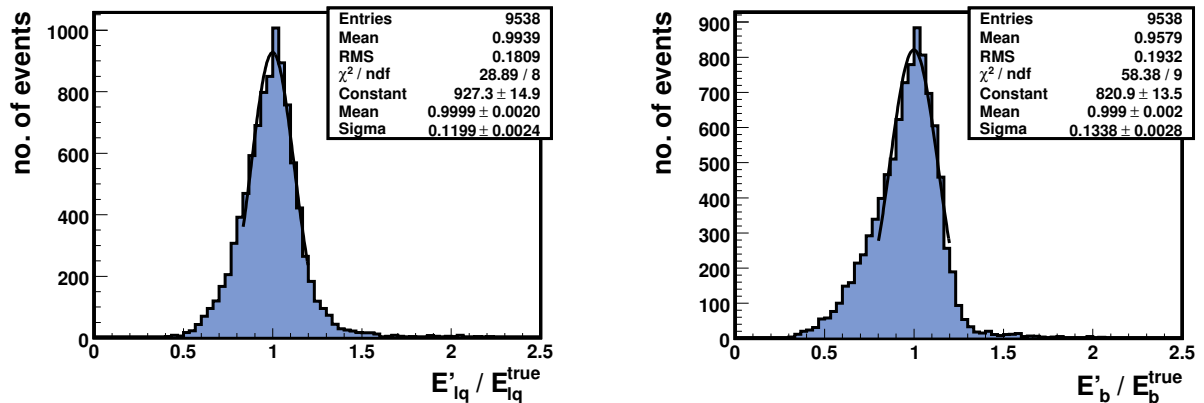


Figure 6.12.: Ratio $\frac{E'}{E^{true}}$ of calibrated energies. Left: for light quark jets. Right: for b quark jets. The peaks are located around one within their errors.

After calibration it is:

$$\mu_{lq} \left(E'_q / E_q^{true} \right) = 0.9999 \pm 0.0020 \quad (6.54)$$

$$\mu_b \left(E'_b / E_b^{true} \right) = 0.999 \pm 0.002. \quad (6.55)$$

The calibration of the JES also affects the reconstructed top quark masses – if all energies are systematically shifted to smaller energies e.g., the top quark mass is shifted to smaller masses. Figure 6.13 shows the reconstruction of the hadronically decaying top quark mass before and after calibration.

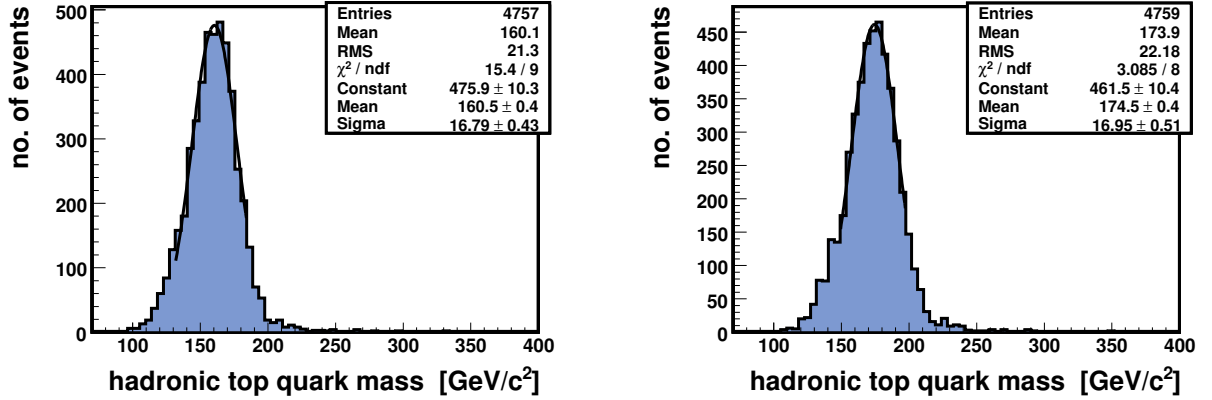


Figure 6.13.: Reconstructed hadronically decaying top quark mass. Left: before calibration. Right: after calibration. The top mass was generated at 175 GeV/c².

A Gaussian fit to the top quark mass peak yields

$$\mu(m_{top}) = 160.5 \pm 0.4 \text{ GeV}/c^2 \quad (\text{before calibration}) \quad (6.56)$$

$$\mu(m_{top}) = 174.5 \pm 0.5 \text{ GeV}/c^2 \quad (\text{after calibration}). \quad (6.57)$$

From the sensitivity of the top quark mass to systematical shifts of the energies, follows the potential of the calibration of the JES. For all studies made in the following always the calibrated energies are used and denoted by E' .

6.7.2. JES – Sensitivity of the Kinematic Fit

Since within the KF the energy of detector signals is fitted, it contains the potential to be sensitive to the JES. This can be investigated by studying the fit results in which the JES has been varied. Therefore, every jet energy value is multiplied by a JES factor of α . The aim is to estimate α only from the result of the KF. This is done by establishing a JES calibration curve for light quark and b quark jets separately. This curve has been created for the correct jet assignment. The investigation with respect to jet combinatorics happens in the same way but has not yet been performed.

The distribution $\frac{\alpha \cdot E'_i}{E_i^{true}}$ shows if the method is sensitive to the JES. If so, the KF performs a restraint to the fitted energies in such a manner that the fitted energy values tend towards the true energy values and therefore, they tend to compensate a wrong JES factor α . This restraint is performed by the first W -mass constraint and the equal mass constraint which are of totally different quality (see below).

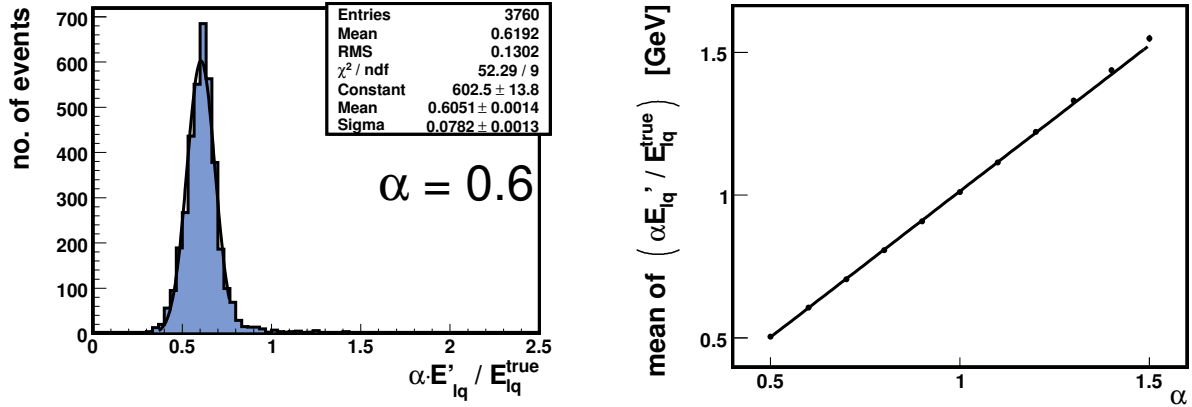


Figure 6.14.: Consistency check for the JES. Left: distribution of the ratio $\frac{E'_{lq}}{E_{lq}^{true}}$ for a JES factor of $\alpha = 0.6$. A Gaussian fit marks the peak. Right: peak position of the Gaussian fit of several plots analogous to the left plot with different JES factors α . The line marks a linear fit of the points. The error results from the error of the Gaussian fit.

The result of a consistency check for the JES is shown in Figure 6.14. The left plot depicts the distribution of the ratio $\frac{\alpha \cdot E'_{lq}}{E_{lq}^{true}}$ for a factor of $\alpha = 0.6$. Let $\mu \left(\alpha \cdot E'_{lq} / E_{lq}^{true} \right) =: \mu'_{\alpha, lq}$ be the mean of a Gaussian fit of a peak to this distribution. For the left plot of Figure 6.14 it is $\mu'_{0.6, lq} = 0.6051 \pm 0.0014 \approx \alpha$ which is consistent with the included JES. Note that the number of events has been decreased compared to the plots in Figure 6.12 for instance. This is due to the fact that the JES was remarkably modified. Consequently, more events are discarded because it is more often the case that no physically reasonable neutrino can be reconstructed (ν -error increases).

The right plot of Figure 6.14 shows $\mu'_{\alpha, lq}$ as a function of α for $0.5 \leq \alpha \leq 1.5$ in steps of 0.1. A linear fit to this plot yields a bisecting line. Therefore, the included factor of α is extracted one-to-one from the changed energy values. Thus the consistency check is successful. An analogous result follows for b quark jets.

In the next step, the sensitivity of the KF to the JES is investigated by studying the distribution of the ratio $\frac{\alpha \cdot E'_{fit}}{E_{fit}}$ which only depends on the measured and fitted energy values. Figure 6.15 shows this ratio for both light quark and b quark jets separately for a JES factor of $\alpha = 0.6$. The distribution for the light quark jets is significantly shifted from one, with a peak at $\mu_{0.6, q}^{fit} = 0.797 \pm 0.002$. Evidently the fitted energies receive a restraint which causes them to have on average larger energies than the measured ones. This tendency leads to fitted energy values which are on average closer to the true energies than the measured ones because all measured energies are scaled with a factor of 0.6 in this example. Thus the KF is sensitive to the JES of the light quarks.

The right plot of Figure 6.15 shows the analogous distribution for b quark jets. The mean $\mu_{0.6, b}^{fit} = 1.003 \pm 0.001$ is not shifted from one. Although the measured energies are scaled with a factor of 0.6 the fitted energies are not systematically shifted to higher energies. Thus the KF applied as described in Section 6.1 is not sensitive to the JES of the b quark jets.

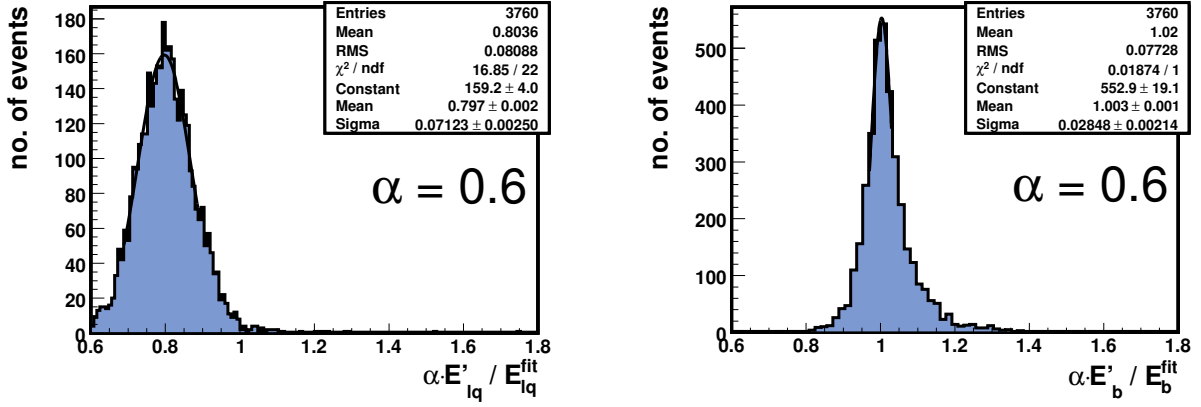


Figure 6.15.: Distribution of the ratio $\frac{E'}{E^{fit}}$. Left: for light quark jets. Right: for b quark jets.

The same investigations are made for different JES factors of $0.5 \leq \alpha \leq 1.5$ in steps of 0.1. Figure 6.16 shows μ_{α}^{fit} as a function of α for light quark and b quark jets separately. Note the change in scales. In the left plot the dependency of the fitted energies from the JES can be

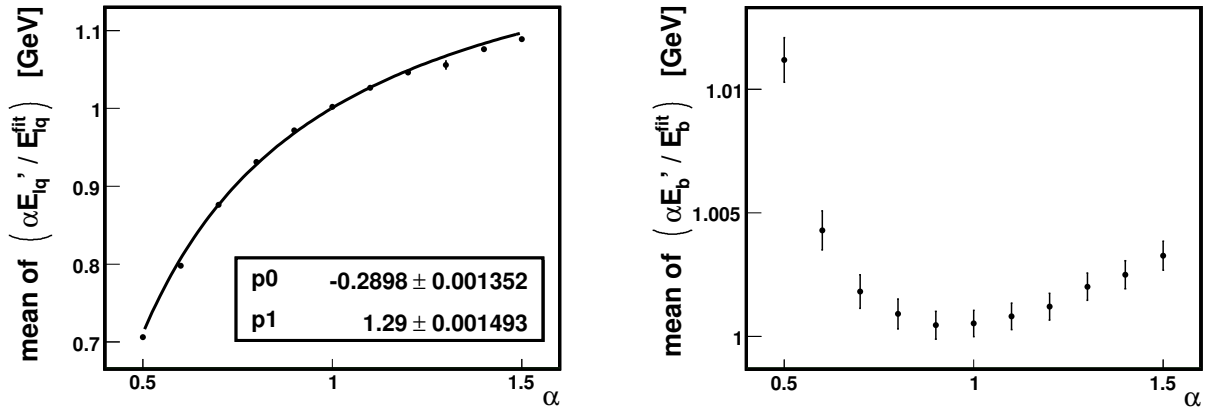


Figure 6.16.: Mean of the distribution of the ratio $\frac{\alpha E'}{E^{fit}}$ for several JES factors $0.5 \leq \alpha \leq 1.5$ in steps of 0.1. Left: for light quark jets. Right: for b quark jets.

recognized: the larger the JES factor α the larger $\mu_{\alpha, lq}^{fit}$. This plot represents a calibration curve for the JES of light quark jets.

To understand the shape of the curve the following consideration can be made: the ideal calibration curve would be the bisecting line of Figure 6.14 (right plot): if the fitted energies always led to the true energy values the calibration curve would be identical with this plot. On the other hand the fitted energies would be identical with the measured energies if there were no constraints (Section 5.1). In this case no calibration could be performed because for every $\alpha > 0$ the mean $\mu_{\alpha, q}^{fit}$ would be equal one, resulting in a horizontal line in Figure 6.16 (left plot) at $\mu_{\alpha, q}^{fit} = 1$. Thus the calibration curve is situated between the constant $\mu_{\alpha, q}^{fit} = 1$ and the bisecting line caused by the restraint of the constraints. Thereby at $\alpha = 1$ also the distribution $\frac{E'_{lq}}{E^{fit}_{lq}}$ peaks at one, because the detector is calibrated (Section 6.7.1).

To estimate the precision of the calibration of the JES, the error of the mean $\sigma(\mu_{\alpha,q}^{fit})$ can be used. This error depends on the number N of events which were applied to the fit:

$$\sigma(\mu_{\alpha,q}^{fit}) \propto \frac{1}{\sqrt{N}}. \quad (6.58)$$

A data sample with a luminosity of 43.4 pb^{-1} is used for these studies as described in Section 6.2.2. Since the calibration curve is not linear but a function of the JES, the precision of the calibration of the JES is a function of α . Therefore, the curve must be parametrized. This is done by the following model:

$$\mu_{\alpha,q}^{fit} = \frac{c_1}{\alpha} + c_2, \quad \begin{aligned} c_1 &:= -0.2898 \pm 0.0014 \\ c_2 &:= 1.2900 \pm 0.0014. \end{aligned} \quad (6.59)$$

The precision of the JES can thus be obtained from the one-sigma environment $\sigma(\mu_{\alpha,q}^{fit})$ for different values of α

$$\sigma(\mu_{0.5,q}^{fit}) = 0.0020 \quad \Rightarrow \quad \alpha = 0.5 \begin{matrix} +0.0017 \\ -0.0017 \end{matrix} \quad (6.60)$$

$$\sigma(\mu_{1.0,q}^{fit}) = 0.0007 \quad \Rightarrow \quad \alpha = 1.0 \begin{matrix} +0.0024 \\ -0.0024 \end{matrix} \quad (6.61)$$

$$\sigma(\mu_{1.5,q}^{fit}) = 0.0022 \quad \Rightarrow \quad \alpha = 1.5 \begin{matrix} +0.0156 \\ -0.0153 \end{matrix}. \quad (6.62)$$

In the right plot of Figure 6.16 the calibration curve for the b quark jets is depicted. Note that the scale of the y -axis is stretched by a factor of roughly 50 compared to the left plot. For $\alpha = 1$ the mean $\mu_{1,b}^{fit}$ is not exactly one but $\mu_{1,b}^{fit} \approx 1.0005 \pm 0.0005$. This is because the calibration of the detector can not be performed with infinite accuracy. However, the calibration was successful since $\mu_{1,b}^{fit}$ differs less than one per mill from one which lies within the one sigma environment. A large modification of the JES by a factor of $\alpha = 1.5$ causes a shift of the mean $\mu_{1.5,b}^{fit}$ of only two per mill. This is due to the fact that the equal mass constraint and the first W -mass constraint are of totally different quality: the latter one introduces an *absolute reference value* to the KF, namely the distinct value of the pole mass of the W boson. It depends only on the two light quark energies and claims the equality of their invariant mass with a particular W boson mass. Thus an absolute benchmark is inserted into the KF for the light quark jets, resulting in a strong restraint for the light quark energy parameters and leading to the sensitivity for the JES. In contrast, within the equal mass constraint only the equality of the invariant mass of the two decaying top quarks is demanded without inserting an absolute value. Hence, via the equal mass constraint no sensitivity to an absolute energy scale is performed. Additionally, the equal mass constraint implies a larger freedom to the parameters because six quantities can be varied in order to satisfy it.

Nevertheless, certain tendencies can be recognized. For JES factors smaller than one the curve increases meaning that on average the fitted energy of the b quarks E_b^{fit} decreases. This can be explained by the first W -mass constraint: for $\alpha < 1$ the measured jet energies are smaller than the true energies. Therefore the fitted light quark jet energies are larger than the measured ones (Figure 6.16, left plot). According to the equal mass constraint the higher energy of the light quark jets must be balanced by the energy of the b quark jets. Consequently, on average E_b^{fit} decreases. For $\alpha > 1$ the measured energy values are on average larger than the true ones. The influence of the light quarks to the equal mass constraint is smaller than for the case $\alpha < 1$ because the slope of the calibration curve in Figure 6.16 (left plot) decreases for increasing α . Thus the measured energy value of the lepton becomes more important. The lepton is the only particle which is not affected by the JES.

All energies of the decay products of t_{had} are scaled with α , in contrast to the decay products of t_{lep} where the lepton is released. Therefore the smaller invariant mass of t_{lep} must be compensated by decreasing energies $E_{\alpha,b}^{fit}$ of the hadronic hemisphere in order to balance the leptonic one. Consequently, the curve of Figure 6.16 (right plot) increases for increasing α .

6.7.3. Studies of the Energy Resolution

In Figure 6.17 the energy resolution of the simulated events before and after the fit is plotted for electrons, light quark and b quark jets separately. The correct jet combination has been chosen in order not to distort the result by combinatorial background.

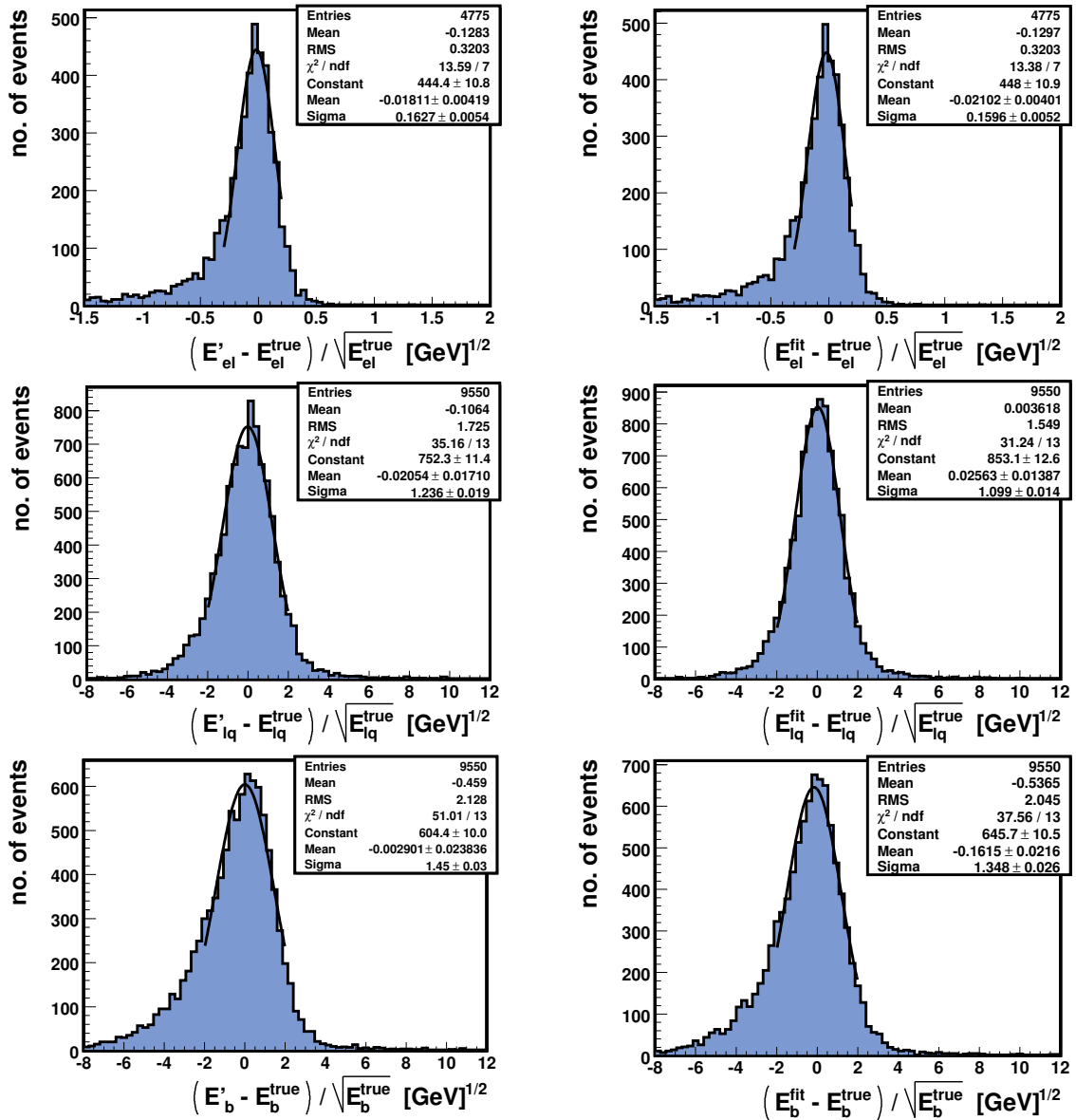


Figure 6.17.: Energy resolution for electrons (top), light quark jets (middle) and b quark jets (bottom). On the left plot in each case the energy resolution of the measured energies is plotted and on the right plot the energy resolution of the fitted energies respectively.

From the left plots of Figure 6.17 it can be recognized that the energy resolution of the simulated ATLAS data is not Gaussian-like distributed but is asymmetric and contains non-Gaussian tails. Therefore, considering more realistic ATLAS data, the assumption of Gaussian distributed energy parameters is only an approximation.

From the reduced χ^2 values of a Gaussian fit to the peak of the energy distributions the tendency to fit the energies such that they are Gaussian distributed can be recognized: for b quark jets (light quark jets) the reduced χ^2 value of the Gaussian fit of the measured energy resolution is about 3.9 (2.7) while for the fitted energy resolution it decreases to 2.9 (2.4). Thus the fitted energies consequently have a more Gaussian-like character.

Table 6.15 summarises the results of the Gaussian fit to the peaks of the energy resolutions.

Table 6.15.: Widths σ of the Gaussian fit to the energy resolutions of electrons, light quark jets and b quark jets. These widths yield the characteristic energy resolution parameters for smearing the energies Gaussian-like (Section 6.5.1). “Rel. impr.” denotes the relative improvement of the width due to the fit. The error is the error of the mean of the Gaussian fit.

object	σ' [GeV] ^{1/2}	σ^{fit} [GeV] ^{1/2}	rel. impr. [%]
electron	0.1627 ± 0.0054	0.1596 ± 0.0052	1.905 ± 0.032
lq jet	1.236 ± 0.019	1.099 ± 0.0014	11.084 ± 0.015
b quark jet	1.45 ± 0.03	1.38 ± 0.026	4.828 ± 0.033

The widths of the measured energy resolutions yield the parameters for the Gaussian-like smearing of the MadEvent data (Section 6.2.1).

For electrons the width of the energy resolution is about $\sigma'_{el} \approx 16\% \text{ GeV}^{1/2}$ which is by far a better resolution than that for the measurement of hadronic jets. This is due to the fact, that electrons leave isolated signals in the electromagnetic calorimeter and do not hadronize to jets.

Concerning jets the relative energy resolution is larger than $120\%/\sqrt{E} [\text{GeV}]$. As described in Section 3.2.2 for pions the energy resolution is about $50\%/\sqrt{E} [\text{GeV}]$. This discrepancy can be explained by effects concerning jets: pions leave very collimated signals in a calorimeter because they consist of quarks in a bound state. In contrast single quarks hadronize by forming jets. There are algorithms which take care of the assignment, mis-identification or clustering of jets (cone-algorithm, K_T -algorithm, etc.). In multijet events (events with more than one jet) it is often difficult to determine which track belongs to which jet. The assignment is not unique and depends on sharp criteria which have to be defined in order to identify a jet signal. A certain maximum size of a jet for instance can be defined by a cone in the η - ϕ -plane (cone algorithm). Thus it is possible that two jets cannot be separated and are regarded as one or vice versa, that one jet is identified as several ones. Thus there are more uncertainties for the measurement of the energy of a jet.

Regarding b quark jets, their width ($\sigma'_b = 1.45 \text{ GeV}^{1/2}$) is larger than the width of light quark jets ($\sigma'_{lq} = 1.22 \text{ GeV}^{1/2}$). This is because of the following effects: within b quark jets more often muons and neutrinos are released than in light quark jets. Thus on average more energy is missing in b quark jets. Furthermore, b quark jets are on average broader than light quark jets due to their larger invariant mass. A larger invariant mass causes a larger showering angle, similar to a two body decay (Equation (5.3)). Since it is more difficult to estimate the energy of broad jets, b quark jets are thus measured with a lower accuracy than light quark jets.

Similar to b quark jets the electrons are only directly affected by the equal mass constraint which causes a weak restraint compared to the first W -mass constraint (Section 6.7.2). Thus the relative improvement of the fit yields roughly 2% (5%) and for electrons (b quark jets). By contrast the improvement of the energy resolution of light quark jets is approximately 11%.

6.7.4. Reconstruction of the Decay Topology of $t\bar{t}$ Events

In this section the combinatorial efficiency of the KF applied on simulated ATLAS events is studied. Other than for the investigations with MadEvent data, the events are generated in NLO and contain jets which are not coming directly from the decay of a $t\bar{t}$ system but from ISR and FSR, respectively. The KF is first tested on events without ISR and FSR and the results are compared to those of Section 6.5 and Section 6.6. In a second study, the events with ISR and FSR are investigated. They cannot be separated from the events without ISR/FSR in a real experiment.

Jets coming directly from the decay of a $t\bar{t}$ system (and not from ISR or FSR) can be identified using MC data: a matching flag indicates the origin of a jet. Therefore, it is possible to test the KF with events which do not contain additional jets by selecting only events with four matched jets (Figure 6.2, events marked in red in the four-jet bin). The evaluation of the KF with these events gives information about the performance of the method using data with realistic generated jets.

The matching flag does not exist for real data. Thus a selection of solely events without ISR/FSR cannot be performed in a real experiment. Consequently, all four-jet events must be used with the KF (the whole four-jet bin of Figure 6.2, right plot).

It is also possible to consider events in which five jets are measured. Thereby one jet must be discarded. This selection can be realised by evaluating the Lagrange function for every possible jet assignment of four from five jets. Since the number of jet permutations is remarkably larger for five jets ($\frac{5!}{2} = 60$), the efficiency to find the correct jet combination strongly decreases. Hence, the consideration of five-jet events is not suitable for the studies performed in this thesis.

If a jet coming from ISR/FSR is assigned to a jet of the decay products of a $t\bar{t}$ system, it is always treated as a wrong assigned jet. Thus a four-jet event in which one jet is faked cannot be entirely correct reconstructed. Another consequence is that it is possible to reconstruct an event in which only the hadronic hemisphere is correctly assigned if a jet coming from ISR/FSR is assigned to the leptonic hemisphere while the hadronic hemisphere is accurately reconstructed. This is not possible without additional jets coming from ISR/FSR (Section 6.5.2).

In Table 6.16 combinatorial results of the KF fit are given for four-jet events in which all jets are matched. Thereby the errors are larger compared to previous investigations because of the lower statistics.

Table 6.16.: Results of the KF applied to simulated ATLAS data. The table is analogous to Table 6.11. The uncertainties are statistic uncertainties only.

ν -error [%]	$E_{\text{ff}}^{\text{correct}}$ [%]	$E_{\text{ff}}^{\text{only had}}$ [%]	$E_{\text{ff}}^{\text{only lep}}$ [%]	$E_{\text{ff}}^{\text{wrong}}$ [%]
26.5 ± 7.0	43.8 ± 5.5	0.0 ± 0.0	22.1 ± 7.7	34.1 ± 6.2

These results correspond to the results of Table 6.11. There, the energy resolution is also smeared according to a realistic simulation of the ATLAS detector resolution. Consequently, the results are the same within their uncertainties.

This comparison shows that the substantial effects of the results of the KF can be investigated by using MadEvent data in which the energy resolution is smeared with respect to the ATLAS detector.

In the next step, the result of the KF including additional jets from ISR/FSR is investigated. Table 6.17 shows the results of the KF for all four-jet events including events with ISR/FSR (Figure 6.2, right plot, four-jet bin).

Table 6.17.: Results of the KF applied to simulated ATLAS data. The table is analogous to Table 6.4.

ν -error [%]	$E_{\text{ff}}^{\text{correct}}$ [%]	$E_{\text{ff}}^{\text{only had}}$ [%]	$E_{\text{ff}}^{\text{only lep}}$ [%]	$E_{\text{ff}}^{\text{wrong}}$ [%]
28.7 ± 4.6	20.1 ± 5.5	0.9 ± 25.8	24.3 ± 5.0	54.8 ± 3.3

This is the most appropriate result of the KF within this thesis: it contains a boost of the $t\bar{t}$ system, considers ISR and FSR as well as the jet combinatoric, but not the fit of $p_{t\bar{t},T}$, because this consequently leads to a worsening of the results (Section 6.7.7). The KF with this configuration yields a combinatorial efficiency for the completely correct reconstruction of a $t\bar{t}$ decay of approximately 20%, where only 47% of the input data has the potential to be correctly reconstructed (Figure 6.2, right plot, four-jet bin). This is consistent with the result of Table 6.16: multiplying the efficiency $E_{\text{ff}}^{\text{combi}}$ of roughly 44% with the fraction of 47% of the events without ISR/FSR yields about 20%.

6.7.5. b -tagging Efficiencies

In this section the b -tagging efficiency of the KF using simulated ATLAS data is studied. Analogous to the previous section investigations for events without additional jets from ISR/FSR are performed for comparing the results with the results with MadEvent data in which no ISR and FSR appears (Section 6.6.3). Finally, the b -tagging efficiencies for all four-jet events including events in which ISR and FSR occur are presented.

The results of the KF using four-jet events of simulated ATLAS data in which no jets from ISR/FSR emerge are presented in Table 6.18. The results show the same tendencies as the results

Table 6.18.: b -tagging efficiencies and combinatorial efficiencies of the KF for different modifications where only the events without additional jets coming from ISR/FSR were used. This Table is analogous to Table 6.12.

Conf.	$p_{t\bar{t},T}$ - flag	Combi- flag	$E_{\text{ff}}^{\text{combi}}$ [%]	$E_{\text{ff,b,had}}^{\text{combi}}$ [%]	$E_{\text{ff,b,lep}}^{\text{combi}}$ [%]	$E_{\text{ff}}^{\text{b-tag}}$ [%]
2	0	1	43.8 ± 5.5	49.2 ± 5.2	65.9 ± 4.5	76.5 ± 4.1
4	1	1	32.8 ± 6.3	39.8 ± 5.7	50.3 ± 5.1	74.3 ± 4.2
MC	0	1	46.2 ± 5.2	51.9 ± 4.9	67.1 ± 4.3	76.4 ± 4.0

of the KF with the MadEvent data which are discussed in Section 6.5.3 in detail. Likewise, the absolute values of the b -tagging efficiency corresponds to those of Table 6.5.

In Table 6.19 analogous results to Table 6.18 are shown for all four-jet events of the simulated ATLAS data (including jets from ISR and FSR). Comparison of Table 6.19 with Table 6.18 yields the same tendencies of the results. The fit results are worsened.

Table 6.19.: b -tagging efficiencies and combinatorial efficiencies of the KF for different modifications including jets from ISR/FSR. This Table is analogous to Table 6.12.

Conf.	$p_{t\bar{t},T^-}$ flg	Combi- flg	$E_{\text{ff}}^{\text{combi}}$ [%]	$E_{\text{ff,b,had}}^{\text{combi}}$ [%]	$E_{\text{ff,b,lep}}^{\text{combi}}$ [%]	$E_{\text{ff}}^{\text{b-tag}}$ [%]
2	0	1	20.1 ± 5.5	33.8 ± 4.2	44.3 ± 3.7	58.8 ± 3.2
4	1	1	15.0 ± 6.3	30.4 ± 4.5	35.6 ± 4.1	57.6 ± 3.2
MC	0	1	23.9 ± 5.2	38.3 ± 4.1	49.4 ± 3.6	61.5 ± 3.2

This is due to the fact that the jets coming from ISR/FSR bias the result. Conf. 2 is the configuration of the KF with the most realistic investigations of the data and yields a b -tagging efficiency of about $(58.8 \pm 3.2)\%$. The implementation of an additional fit of the transverse momentum of the $t\bar{t}$ system (Conf. 4) worsens the efficiency to approximately $57.6 \pm 3.2\%$.

6.7.6. Reconstruction of the Top Quark Mass

Analogous to Section 6.5.4 the reconstructed top quark mass of the hadronically decaying top quark is depicted in Figure 6.18. The mass is plotted for matched (left) and unmatched (right) events.

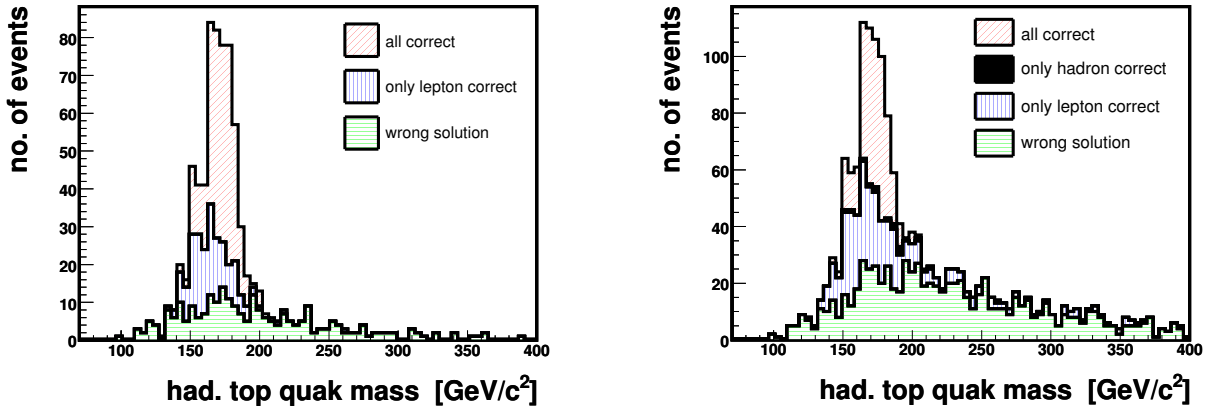


Figure 6.18.: Reconstructed invariant mass of the hadronically decaying top quark. For the reconstruction the fitted energies are taken (Section 6.7.4). Within a stack plot it is colour-coded how the event topology could be reconstructed: red, hatched ascending from right to left: correct combination. Blue, hatched vertically: only the leptonic hemisphere is correctly reconstructed. Black, filled: only the hadronic hemisphere is correctly reconstructed. Green, hatched horizontally: no hemisphere is correctly reconstructed. Left: fit in which only matched events are used (Figure 6.2, right, four-jet bin, events marked in red). Red: $\approx 44\%$, blue: $\approx 22\%$, black: 0% , green: $\approx 34\%$. Right: fit in which unmatched events are used (Figure 6.2, right, the whole four-jet bin). Red: $\approx 20\%$, blue: $\approx 25\%$, black: $\approx 1\%$, green: $\approx 54\%$.

In Table 6.20 the RMS value and the widths of a Gaussian fit to the peak of the plots in Figure 6.7 are summarised.

Table 6.20.: Results of the reconstruction of the invariant mass of hadronically decaying top quarks from the fitted energies. This table is analogous to Table 6.6.

	$E_{\text{ff}}^{\text{correct}}$ [%]	$\sigma_{\text{top}}^{\text{had}}$ [GeV]	$\text{RMS}_{\text{top}}^{\text{had}}$ [GeV]
matched	43.8 ± 5.5	11.1 ± 0.7	36.4
unmatched	20.1 ± 5.5	13.3 ± 0.9	59.6

The result of the matched data sample is in accordance with the result of Table 6.13 within the error. Considering the unmatched events, it is possible to reconstruct the hadronic hemisphere correctly while the leptonic one is wrongly assigned via a jet coming from ISR/FSR (Section 6.5.2). This is the case for about 1% of the events. The RMS value increases considerably compared to the fit with matched events. This is because the fraction of wrongly reconstructed events, which forms the combinatorial background, is larger. Comparing the plots in Figure 6.18 with each other, the larger combinatorial background can clearly be recognized in the larger fraction of events marked in green.

Although the additional combinatorial background for events including jets from ISR/FSR is considerably larger (the ratio of wrong events to fitted events increases for more than 60% for unmatched events, Section 6.6.2), the width of a Gaussian fit to the mass peak only increases for approximately 2% percent. Thus the bias coming from ISR/FSR only slightly worsens the reconstruction of the invariant top quark mass.

6.7.7. Studies of the Transverse Momentum of the $t\bar{t}$ System

Since the simulated decaying $t\bar{t}$ pairs of the ATLAS data are boosted on parton level, no investigation of unboosted $t\bar{t}$ pairs is made. The effect of the boost is already studied in Section 6.5 and 6.6.

Table 6.21 is analogous to Table 6.14 and summarises the results for a KF of matched and unmatched data.

Table 6.21.: Fit results of the KF for different modifications analogous to Table 6.7 and Table 6.8. If “Mat.-flag.= 1” only matched data is used.

Conf.	Mat.- flag	$p_{t\bar{t},T}$ - flag	ν -error [%]	$E_{\text{ff}}^{\text{correct}}$ [%]	$\sigma_{\text{had}}^{\text{top}}$ [GeV]	$\text{RMS}_{\text{had}}^{\text{top}}$ [GeV]	$\sigma_{\text{lep}}^{\text{top}}$ [GeV]	$\text{RMS}_{\text{lep}}^{\text{top}}$ [GeV]
2a	1	0	26.5 ± 7.0	43.8 ± 5.5	11.1 ± 0.7	36.9	13.0 ± 1.0	36.4
4a	1	1	26.5 ± 7.0	32.8 ± 6.3	12.7 ± 1.0	48.4	17.1 ± 2.7	46.3
2b	0	0	28.7 ± 4.6	20.1 ± 5.5	13.3 ± 0.9	59.5	14.8 ± 1.1	55.7
4b	0	1	28.7 ± 4.6	15.0 ± 6.3	17.7 ± 2.2	61.9	26.7 ± 7.8	60.4

Comparing Conf. 2a and Conf. 4a with the corresponding configurations of Table 6.14, leads to the same tendencies. This is also true for a comparison of Conf. 2b and Conf. 4b with the same table. However, the results of the KF with the configurations Conf. 2b and Conf. 4b are worsened due to the jets coming from ISR/FSR.

Considering Conf. 4b, the width of the Gaussian fit to the leptonically decaying top quark is $\sigma_{\text{lep}}^{\text{top}} = (26.7 \pm 7.8)$ GeV. In this particular case the Gaussian fit was not suitable and did not fit to the histogram which led to an outlier. This configuration is better characterized by its RMS value which increases from $\text{RMS}_{\text{lep}}^{\text{top}} = 55.7$ to $\text{RMS}_{\text{lep}}^{\text{top}} = 60.4$ comparing Conf. 2b. Hence, here also the worsening of the fit result due to the consideration of $p_{t\bar{t},T}$ can be recognized.

6.7.8. Studies of the Energy Resolution Including Jet Combinatorics

In Section 6.7.3 the energy resolution for light quark and b quark jets is investigated with respect to the correct jet combination. However, in a real experiment, the correct jet assignment must be estimated by the fit result. Therefore, in the following, the energy resolution is investigated using the jet combination coming from the application of the KF. Furthermore, the data sample including ISR/FSR is used for the studies in order to test the KF with more realistic data.

In Figure 6.19 the energy resolution for light quark (top) and b quark jets (bottom) is depicted for the measured (left) and fitted energy values (right).

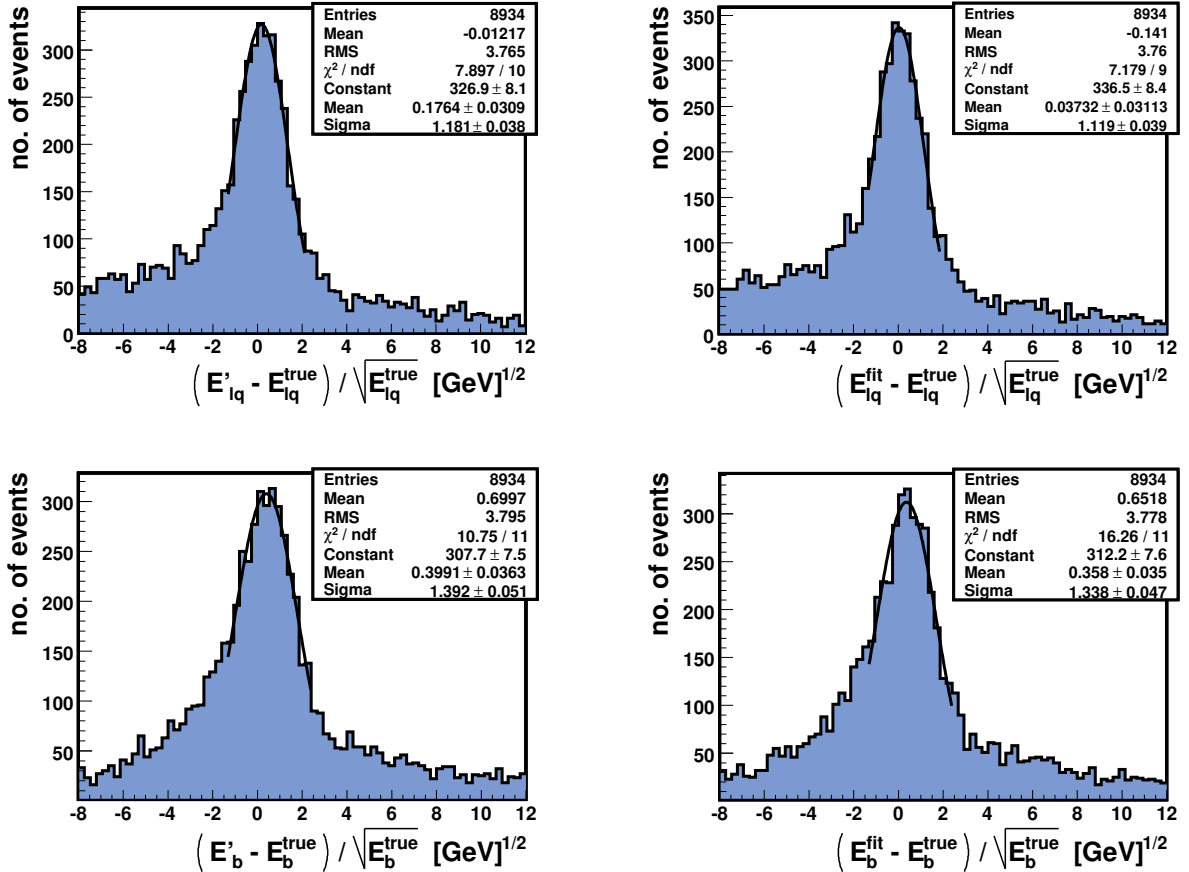


Figure 6.19.: Energy resolution of jets coming from simulated $t\bar{t}$ events. Thereby the jet assignment is estimated via the KF. The used data include jets coming from ISR/FSR. Top: for light quark jets. Bottom: for b quark jets. On the left in each case: energy resolution of the smeared energy values. On the right in each case: energy resolution of the fitted energies.

The combinatorial background can be recognized in each plot of Figure 6.19. In these events the reconstruction of the event topology leads to a wrong jet assignment. Consequently, at the comparison with the true energy values, different jets are compared with each other, leading to outliers in the energy resolution. If the correct jet is assigned to a parton, it contributes to the peak of the energy resolution.

Nevertheless, the restraint of the KF leads to an improvement of the energy resolution. In Table 6.22 the widths of a Gaussian fit to the peaks of Figure 6.19 is summarised and the relative improvement of the energy resolution is indicated.

Table 6.22.: Widths σ of the Gaussian fit to the energy resolutions of light quark jets and b quark jets. The relative improvement of the resolutions is also indicated. The errors are the errors of the mean of the Gaussian fits.

object	σ' [GeV] ^{1/2}	σ^{fit} [GeV] ^{1/2}	rel. impr. [%]
lq jet	1.18 ± 0.04	1.12 ± 0.04	5.25 ± 0.05
b quark jet	1.39 ± 0.05	1.34 ± 0.05	3.88 ± 0.05

For light quark (b quark) jets an improvement of about $5.3 \pm 0.1\%$ ($3.9 \pm 0.1\%$) of the energy resolution is found. Thus the KF positively affects the energy resolution of jets, with respect to the estimated jet assignment, under consideration of ISR/FSR. Here, also the tendency that in particular the light quark jets – compared to the b quark jets – are positively affected by the KF, can be recognized.

7. Conclusion and Outlook

In the following, the results of the KF are summarised and conclusions are drawn. Finally, further possible investigations and improvements of the KF are presented within an outlook.

7.1. Summary and Conclusion

In this thesis a KF of $t\bar{t}$ events in the semi-leptonic channel has been established using the χ^2 method and extending it by the method of the Lagrangian multipliers in order to take constraints into account. The constraints have been derived from the application of the fundamental energy- and momentum conservation to the $t\bar{t}$ decay topology. They have been inserted valuable information into the method which has positively affected the fit results.

Firstly, the concept of the KF has been established and investigated for the simple example of the decay of a pion into two photons. It has been shown that the KF works and yields an improvement of the relative energy resolution of more than 15%. The test of the KF has thus been successful. Consequently, the method contains the potential to be successfully applied to other decay processes.

Subsequently, the KF has been applied to the decay of a $t\bar{t}$ system via the semi-leptonic decay channel. In all studies made in Chapter 6 the KF led to an improvement of the relative energy resolution: the fitted energies were on average closer to the true energy values than the measured ones. Therefore, it is sensitive to the JES of a calorimeter. The KF, as it has been performed in the presented studies, is sensitive to the light quark JES: a calibration curve has been established and discussed. For a simulated data sample of 43.4 pb^{-1} , the JES can be estimated with a precision of roughly 0.2% for a JES factor of $\alpha = 0.5$ and approximately 2% for a JES factor of $\alpha = 1.5$, disregarding jet combinatorics. Thus the calibration of a calorimeter can be performed with respect to light quark jets.

For b quark jets a calibration curve has also been established; but it has been shown, that there are only small effects due to a variation of the JES. Consequently, the KF as it has been realised in these studies, is not sensitive to the JES of b quark jets. This different behavior of the KF concerning light quark and b quark jets has been explained by the different impact of the constraints.

The KF also yields a handle on the reconstruction of the topology of the $t\bar{t}$ decay. In approximately 44% of the events (without ISR/FSR, Table 6.16) the decay topology has been completely reconstructed, in contrast to finding the correct combination by chance, with only a probability of roughly 8%. Taking ISR and FSR into account, the efficiency decreases to about 21% for the correct reconstruction with the KF and to approximately 4% for the correct combination by chance.

Since the transverse momentum of $t\bar{t}$ pairs is of importance at the LHC, it has been studied by introducing new fit parameters to the KF. The consideration of a transverse momentum within the KF via the χ^2 method always causes a decrease of result accuracy, with respect to the $p_{t\bar{t},T}$ distribution of simulated ATLAS data. This is due to a conceptual bias of the χ^2 method itself: wrong assumptions must be made in order to introduce $p_{t\bar{t},T}$ into the KF. Therefore, the χ^2 method is not appropriate to take the transverse momentum of a $t\bar{t}$ system into account.

Two further applications of the KF have been performed: the identification of b quark jets and the reconstruction of the top quark mass. The efficiency of the b -tagging is about 77% (59%) without (with) ISR/FSR and is only slightly affected by the fit of a transverse momentum of the $t\bar{t}$ system. The reconstruction of the top quark mass is sensitive to every fit parameter. Therefore, the top quark mass provides a *standard candle* for investigations via the KF. Systematic effects of different modifications of the KF have been recognized and understood, considering the reconstructed top quark mass.

For all these studies, the comparison of the results in which the KF has been applied to different data sets has shown the systematical effect, that the χ^2 method introduces a conceptual bias by the assumption of a Gaussian distributed energy resolution.

By applying tight cuts, a data sample can be enriched with events, in which the detector signal comes directly from the decay of a $t\bar{t}$ system. These tight cuts are also suitable for a separation of signal and background. The ratio of events in which no ISR/FSR occurs to events with ISR/FSR could be increased from approximately $(35 \pm 1)\%$ (without tight cuts) to about $(47 \pm 2)\%$ (including tight cuts).

Altogether the KF via the χ^2 method yields a data calibration method which is a powerful tool for the calibration of a detector calorimeter.

7.2. Outlook

For future investigations with the KF, further studies with the χ^2 method can be performed. However, there are certain disadvantages of this method:

- An initial value for every fit parameter is needed.
- The fit parameters are assumed to be Gaussian distributed.
- Constraints have to be linear.

To avoid these disadvantages, the KF can be established using another ansatz: the Likelihood method.

Further studies of the KF via the χ^2 method

- Consideration of background processes (Section 2.2.4). The tight cuts discussed in Section 6.2.2 can be used to separate the signal from the background. A modification of the tight cuts, e.g. the variation of the p_T -cut, can be investigated in order to find the optimal cuts.
- Investigation of the JES with respect to jet combinatorics. In principle, a calibration curve can be obtained analogous to the studies presented in Section 6.7.1.
- Variation of the JES for light quark and b quark jets separately.

- Studies for the sensitivity of the JES to physics analysis, e.g. to the reconstruction of the top quark mass. Since the top quark mass is the most precisely measured quark mass, its invariant mass can be used as *standard-candle* for detectors. The shift of the reconstructed top quark mass due to a miscalibrated calorimeter (Section 6.7.1) points out that via the reconstruction contains the potential to be sensitive to the JES (also for the b quark jets).
- Alternatively to the latter item, a *hard constraint* for the top quark mass can be introduced, analogous to the first W -mass constraint. A particular value of the top quark mass introduces an absolute reference value to the KF. The method would thus be sensitive to the JES of b quark jets.

Further studies of the KF via the Likelihood method

The Likelihood method avoids the disadvantages of the χ^2 method which has been listed above. In addition to the investigations performed in this thesis using the χ^2 method, the following studies can be accomplished with the Likelihood method:

- Insertion of *non-linear* constraints into the KF.
- The energy resolution can be parameterized in terms of *transfer functions*. This is a more realistic description of the energy resolution than the one which follows from the assumption of a Gaussian distribution.
- The masses of the W boson and the top quarks can be assumed to be Breit-Wigner distributed (*soft constraint*). This is a more realistic assumption than the use of a distinct pole-mass (*hard constraint*). Note that the top quark mass of the simulated ATLAS data which has been used in the presented studies has been generated at a sharp value (Section 6.2.2).
- The events which have been discarded from the χ^2 function because the measured values yield a physically unreasonable neutrino solution, can be fitted by the Likelihood method. A separate evaluation of only these events would point out, if they cause a bias to the fit results and should be discarded for the benefit of better fit results.

Analogous to the χ^2 method, the realisation of the KF via the Likelihood method requires the establishment of a Likelihood function \mathcal{L} . A short outline of such a function can be found in the appendix.

Parallel to the studies presented in this thesis, first investigations with the Likelihood method were performed. Since the results are only preliminary they have not been included. However, first tests have shown that in principal results similar to those of this thesis can be achieved. Thus the Likelihood method seems to work fine. For future studies, it would be worth to establish the kinematic fit via the Likelihood method, analogous to the here presented χ^2 method.

A. Notation

The following notation is used in this diploma thesis:

\vec{a}	Vector of a set of (fitting-)parameters
A	Coefficient matrix of χ^2 terms
\vec{b}	Constant terms of the constraints
B	Coefficient matrix of linear terms of the constraints
$BR(x)$	Branching ratio of process x
b_{had}	b quark of the hadronically decaying top quark
b_{lep}	b quark of the leptonically decaying top quark
E_α	Energy of a particle α
E'_α	Measured energy of a particle α
E_α^{true}	True energy of a particle α
E_T^{miss}	Missing transverse energy
f_i	i -th constraint
\tilde{f}_i	i -th approximated constraint via Taylor expansion
L	Lagrange-function
\mathcal{L}	Likelihood-function
lep	Lepton of the leptonically decaying top quark (here: either an electron or a muon)
m_α	Mass of a particle α
$\hat{n}_\alpha = \begin{pmatrix} n_{\alpha,x} \\ n_{\alpha,y} \\ n_{\alpha,z} \end{pmatrix} := \frac{\vec{p}_\alpha}{E_\alpha}$	Unit vector of a particle α with momentum p_α
p_T	Transverse momentum
$p_\alpha = \begin{pmatrix} p_{\alpha,x} \\ p_{\alpha,y} \\ p_{\alpha,z} \\ E_\alpha \end{pmatrix} = \begin{pmatrix} \vec{p}_\alpha \\ E_\alpha \end{pmatrix}$	Four-momentum-vector of a particle α with momentum \vec{p}_α and energy E_α
q	Light quark, i.e. u -quark, d -quark, c -quark or s -quark
\bar{q}	Light anti-quark, i.e. \bar{u} -quark, \bar{d} -quark, \bar{c} -quark or \bar{s} -quark
\sqrt{s}	Centre-of-mass energy

t	Top quark
\bar{t}	Anti-top quark
V	Error matrix
W	W boson; mediator of the weak force
\vec{x}	Vector of a set of measured input variables (of a model $f(x_i)$ e.g.)
\vec{y}	Vector of fit parameter
\vec{y}	Vector of a set of measured values
γ	Photon
δ	Kronecker delta
η	Pseudo-rapidity
ν	Neutrino of the leptonically decaying top quark (here: either an electron-neutrino or a muon-neutrino)
π^0	Neutral pion
λ_i	i -th Lagrange multiplier
χ^2	chi-square-function
$\mathbf{1}_n$	Unit matrix of dimension n
∇_{E_α}	Gradient with respect to the energy of the particle α
\approx	Approximately
\equiv	Identical

Additional used variables are not globally defined and explained in the context.

B. Auxiliary Calculations

B.1. Determination of the Lagrangian Multipliers

As described in Section 4.2, Lagrangian multipliers $\vec{\lambda}$ are introduced in the Lagrange function L in order to take constraints into account. To determine these multipliers one requirement is used: if L is minimal its derivative must become zero. Solving the corresponding equation for the Lagrangian multipliers yields a solution of $\vec{\lambda}$. For the calculation two assumptions are made:

- Constraints can be expressed in a linear way: $B\vec{a} - \vec{b}$.
- Errors are not correlated: $(V^{-1})^T \equiv V^{-1}$.

Thus the Lagrange function can be written as

$$L = \underbrace{(\vec{y} - A\vec{a})^T V^{-1} (\vec{y} - A\vec{a})}_{\chi^2} + 2\vec{\lambda}^T \cdot \underbrace{(B\vec{a} - \vec{b})}_{\text{Constraints}} \stackrel{!}{=} \min \quad (\text{B.1})$$

$$\Rightarrow \nabla_{\vec{a}} L = -A^T V^{-1} (\vec{y} - A\vec{a}) - (\vec{y} - A\vec{a})^T V^{-1} A + 2\vec{\lambda}^T B \quad (\text{B.2})$$

$$= -\underbrace{A^T V^{-1} \vec{y}}_{=: \vec{c}} + \underbrace{A^T V^{-1} A}_{=: C} \vec{a} - \underbrace{\vec{y}^T V^{-1} A}_{\equiv A^T (V^{-1})^T \vec{y} = \vec{c}} + \underbrace{(A\vec{a})^T V^{-1} A}_{=: \vec{a}^T \underbrace{A^T V^{-1} A}_{=: C}} + 2\vec{\lambda}^T B \stackrel{!}{=} 0. \quad (\text{B.3})$$

Solving this equation for $\vec{\lambda}$ yields

$$\Leftrightarrow 0 \stackrel{!}{=} -2\vec{c} + 2C\vec{a} + 2B^T \vec{\lambda}^T \quad (\text{B.4})$$

$$\Leftrightarrow BC^{-1}\vec{c} = B\vec{a} + \underbrace{BC^{-1}B^T}_{=: V_B} \vec{\lambda}^T \quad (\text{B.5})$$

$$\Leftrightarrow \vec{\lambda}^T = V_B^{-1} BC^{-1}\vec{c} - V_B^{-1} B\vec{a} \quad (\text{B.6})$$

with the following auxiliary variables:

$$V_B := BC^{-1}B^T \quad (\text{B.7})$$

$$C := A^T V^{-1} A \quad (\text{B.8})$$

$$\vec{c} := A^T V^{-1} \vec{y} \quad (\text{B.9})$$

B.2. Reconstruction of the Neutrino

Since neutrinos can not be measured at the ATLAS detector, its momentum has to be calculated from the kinematics of the $t\bar{t}$ decay. The x - and y - components of its momentum follow from the assumption

$$p_{\nu,i} = p_{t\bar{t},i} - (p_{q,i} + p_{\bar{q},i} + p_{b_{had},i} + p_{b_{lep},i} + p_{lep,i}) \quad , i := x, y, \quad (\text{B.10})$$

where for $p_{t\bar{t},i}$ the most probable value is taken, namely zero (Section 6.5.5). Considering the remaining z -component of the neutrino, the second W -mass constraint is applied in order to solve it for $p_{\nu,z}$. This results in a quadratic equation. Consequently, there are two solutions for the z -component of the neutrino momentum. Geometrically one solution results from mirroring the other one at the x - y -plane. From the mathematical point of view, both solutions are equitable, but only one solution corresponds to the physical reality. The correct solution is estimated via the value of the whole Lagrange function (Chapter 4). In the following, $p_{\nu,z}$ is determined by using the second W mass constraint:

$$f_3(E_{lep}, E_\nu) = (p_{lep} + p_\nu)^2 - m_W^2 \quad (\text{B.11})$$

$$= \underbrace{E_{lep}^2 - p_{lep}^2}_{=m_{lep} \approx 0} + \underbrace{E_\nu^2 - p_\nu^2}_{=m_\nu \approx 0} + 2E_{lep}E_\nu - 2\vec{p}_{lep}\vec{p}_\nu - m_W^2 \quad (\text{B.12})$$

$$\stackrel{!}{=} 0. \quad (\text{B.13})$$

With $E_\nu = \sqrt{p_{\nu,x}^2 + p_{\nu,y}^2 + p_{\nu,z}^2}$ it follows

$$2(E_{lep}E_\nu - \vec{p}_{lep}\vec{p}_\nu) \stackrel{!}{=} m_W^2 \quad (\text{B.14})$$

$$\Leftrightarrow E_\nu = \frac{m_W^2}{2E_{lep}} + \frac{\vec{p}_{lep}\vec{p}_\nu}{E_{lep}} \quad (\text{B.15})$$

$$\Rightarrow p_{\nu,x}^2 + p_{\nu,y}^2 + p_{\nu,z}^2 = \frac{m_W^4}{4E_{lep}^2} + \left(\frac{\vec{p}_{lep}\vec{p}_\nu}{E_{lep}}\right)^2 + \frac{m_W^2}{E_{lep}^2} \cdot \vec{p}_{lep}\vec{p}_\nu \quad (\text{B.16})$$

$$= \frac{m_W^4}{4E_{lep}^2} + \frac{1}{E_{lep}^2} (p_{lep,x}p_{\nu,x} + p_{lep,y}p_{\nu,y} + p_{lep,z}p_{\nu,z})^2 \quad (\text{B.17})$$

$$+ \frac{m_W^2}{E_{lep}^2} (p_{lep,x}p_{\nu,x} + p_{lep,y}p_{\nu,y} + p_{lep,z}p_{\nu,z}), \quad (\text{B.18})$$

where it is assumed that $E_\nu > 0 \Rightarrow E_\nu^2 > 0$. Solving for $p_{\nu,z}$ one gets

$$\begin{aligned} & p_{\nu,z}^2 - \frac{1}{E_{lep}^2} \cdot p_{lep,z}p_{\nu,z}^2 \\ & - 2\frac{1}{E_{lep}^2} \cdot \left[(p_{lep,x}p_{\nu,x} + p_{lep,y}p_{\nu,y}) p_{lep,z}p_{\nu,z} + \frac{1}{2}m_W^2 \cdot p_{lep,z}p_{\nu,z} \right] \\ & - \frac{1}{E_{lep}^2} \cdot \left[\frac{m_W^4}{4} + m_W^2 \cdot (p_{lep,x}p_{\nu,x} + p_{lep,y}p_{\nu,y}) + (p_{lep,x}p_{\nu,x} + p_{lep,y}p_{\nu,y})^2 \right] + p_{\nu,x}^2 + p_{\nu,y}^2 \\ & \qquad \qquad \qquad = -\frac{1}{E_{lep}^2} \left[\frac{m_W^2}{2} + (p_{lep,x}p_{\nu,x} + p_{lep,y}p_{\nu,y}) \right]^2 \end{aligned}$$

$$\stackrel{!}{=} 0.$$

(B.19)

With

$$p_{\nu,z}^2 - \frac{1}{E_{lep}^2} \cdot p_{lep,z}^2 p_{\nu,z}^2 = p_{\nu,z}^2 \left(1 - \frac{p_{lep,z}^2}{E_{lep}^2} \right) = p_{\nu,z}^2 \left(\frac{E_{lep}^2 - p_{lep,z}^2}{p_{lep,z}^2} \right) = p_{\nu,z}^2 \left(\frac{p_{lep,x}^2 + p_{lep,y}^2}{E_{lep}^2} \right) \quad (\text{B.20})$$

it follows

$$\begin{aligned} p_{\nu,z}^2 - \frac{2p_{lep,z}}{p_{lep,x}^2 + p_{lep,y}^2} \cdot \underbrace{\left[\frac{m_W^2}{2} + (p_{lep,x} p_{\nu,x} + p_{lep,y} p_{\nu,y}) \right]}_{=:b} \cdot p_{\nu,z} \\ - \underbrace{\frac{1}{p_{lep,x}^2 + p_{lep,y}^2}}_{=:a} \cdot \underbrace{\left[\frac{m_W^2}{2} + (p_{lep,x} p_{\nu,x} + p_{lep,y} p_{\nu,y}) \right]^2}_{=:b^2} + \frac{E_{lep}^2}{p_{lep,x}^2 + p_{lep,y}^2} \cdot (p_{\nu,x}^2 + p_{\nu,y}^2) \quad (\text{B.21}) \\ \stackrel{!}{=} 0. \end{aligned}$$

Thus a squarish equation follows

$$\Rightarrow p_{\nu,z}^2 - 2 \cdot ab \cdot p_{lep,z} \cdot p_{\nu,z} - ab^2 + a \cdot E_{lep}^2 \cdot (p_{\nu,x}^2 + p_{\nu,y}^2) \stackrel{!}{=} 0, \quad (\text{B.22})$$

where the following auxiliary variables have been defined:

$$a := \frac{1}{p_{lep,x}^2 + p_{lep,y}^2}; \quad b := \left[\frac{m_W^2}{2} + (p_{lep,x} p_{\nu,x} + p_{lep,y} p_{\nu,y}) \right]. \quad (\text{B.23})$$

Finally the z -component of the neutrino momentum is

$$p_{\nu,z}^{(1,2)} = ab \cdot p_{lep,z} \pm \sqrt{a^2 b^2 \cdot p_{lep,z}^2 + ab^2 - a \cdot E_{lep}^2 \cdot (p_{\nu,x}^2 + p_{\nu,y}^2)}. \quad (\text{B.24})$$

The energy of the neutrino follows under the assumption $m_\nu \approx 0$:

$$E_\nu = \sqrt{p_{\nu,x}^2 + p_{\nu,y}^2 + p_{\nu,z}^2} = E_\nu(p_q, p_{\bar{q}}, p_{b_{had}}, p_{b_{lep}}, p_{lep}). \quad (\text{B.25})$$

B.3. Derivatives of the Equal Mass Constraint

In order to perform a Taylor expansion of the equal mass constraint, it must be derived by the particle energies. Writing the constraint more explicit, the derivatives can be calculated more easily:

$$f_1 = (p_q + p_{\bar{q}} + p_{b_{had}})^2 - (p_{b_{lep}} + p_{lep} + p_\nu)^2 \quad (\text{B.26})$$

$$= \underbrace{p_q^2 + p_{\bar{q}}^2 + p_{b_{had}}^2 - p_{b_{lep}}^2 - p_{lep}^2 - p_\nu^2}_{\approx 0} \quad (\text{B.27})$$

$$+ 2 [p_q p_{\bar{q}} + p_q p_{b_{had}} + p_{\bar{q}} p_{b_{had}} - p_{b_{lep}} p_{lep} - p_{b_{lep}} p_\nu - p_{lep} p_\nu] \quad (\text{B.28})$$

$$= 2 [(E_q E_{\bar{q}} - \vec{p}_q \vec{p}_{\bar{q}}) + (E_q E_{b_{had}} - \vec{p}_q \vec{p}_{b_{had}}) + (E_{\bar{q}} E_{b_{had}} - \vec{p}_{\bar{q}} \vec{p}_{b_{had}})] \quad (\text{B.29})$$

$$- (E_{b_{lep}} E_{lep} - \vec{p}_{b_{lep}} \vec{p}_{lep}) - (E_{b_{lep}} E_\nu - \vec{p}_{b_{lep}} \vec{p}_\nu) - (E_{lep} E_\nu - \vec{p}_{lep} \vec{p}_\nu) \quad (\text{B.30})$$

Let

$$\hat{n}_\alpha = \begin{pmatrix} n_{\alpha,x} \\ n_{\alpha,y} \\ n_{\alpha,z} \end{pmatrix} := \frac{\vec{p}_\alpha}{E_\alpha} \quad (\text{B.31})$$

be the unity vector of the momentum of a particle α . Defining the auxiliary terms t_i

$$t_1 := (1 - \hat{n}_q \hat{n}_{\bar{q}}) \quad (\text{B.32})$$

$$t_2 := (1 - \hat{n}_q \hat{n}_{b_{had}}) \quad (\text{B.33})$$

$$t_3 := (1 - \hat{n}_{\bar{q}} \hat{n}_{b_{had}}) \quad (\text{B.34})$$

$$t_4 := \left(1 - \hat{n}_q \hat{n}_{b_{had}} \cdot \frac{E_{b_{had}}}{\sqrt{E_{b_{had}}^2 - m_{b_{had}}^2}} \right) \quad (\text{B.35})$$

$$t_5 := \left(1 - \hat{n}_{\bar{q}} \hat{n}_{b_{had}} \cdot \frac{E_{b_{had}}}{\sqrt{E_{b_{had}}^2 - m_{b_{had}}^2}} \right) \quad (\text{B.36})$$

$$t_6 := \left(1 - \hat{n}_{b_{lep}} \hat{n}_{lep} \cdot \frac{E_{b_{lep}}}{\sqrt{E_{b_{lep}}^2 - m_{b_{lep}}^2}} \right) \quad (\text{B.37})$$

$$t_7 := \left(1 - \hat{n}_{b_{lep}} \hat{n}_\nu \cdot \frac{E_{b_{lep}}}{\sqrt{E_{b_{lep}}^2 - m_{b_{lep}}^2}} \right) \quad (\text{B.38})$$

$$t_8 := (1 - \hat{n}_{b_{lep}} \hat{n}_{lep}) \quad (\text{B.39})$$

$$t_9 := (1 - \hat{n}_{lep} \hat{n}_\nu). \quad (\text{B.40})$$

The derivatives for the first constraints are:

$$\frac{\partial f_1}{\partial E_{\bar{q}}} = 2 \cdot \left[E_{\bar{q}} \cdot t_1 + E_{b_{had}} \cdot t_2 - \frac{\partial f_1}{\partial E_{\nu}} \cdot \frac{\partial E_{\nu}}{\partial E_{\bar{q}}} \right] \quad (\text{B.41})$$

$$\frac{\partial f_1}{\partial E_{\bar{q}}} = 2 \cdot \left[E_{\bar{q}} \cdot t_1 + E_{b_{had}} \cdot t_3 - \frac{\partial f_1}{\partial E_{\nu}} \cdot \frac{\partial E_{\nu}}{\partial E_{\bar{q}}} \right] \quad (\text{B.42})$$

$$\frac{\partial f_1}{\partial E_{b_{had}}} = 2 \cdot \left[E_{\bar{q}} \cdot t_4 + E_{\bar{q}} \cdot t_5 - \frac{\partial f_1}{\partial E_{\nu}} \cdot \frac{\partial E_{\nu}}{\partial E_{b_{had}}} \right] \quad (\text{B.43})$$

$$\frac{\partial f_1}{\partial E_{b_{lep}}} = 2 \cdot \left[-E_{lep} \cdot t_6 - E_{\nu} \cdot t_7 - \frac{\partial f_1}{\partial E_{\nu}} \cdot \frac{\partial E_{\nu}}{\partial E_{b_{lep}}} \right] \quad (\text{B.44})$$

$$\frac{\partial f_1}{\partial E_{lep}} = 2 \cdot \left[-E_{b_{lep}} \cdot t_8 - E_{\nu} \cdot t_9 - \frac{\partial f_1}{\partial E_{\nu}} \cdot \frac{\partial E_{\nu}}{\partial E_{lep}} \right], \quad (\text{B.45})$$

with

$$\frac{\partial f_1}{\partial E_{\nu}} = E_{b_{lep}} (1 - \hat{n}_{b_{lep}} \hat{n}_{\nu}) + E_{lep} (1 - \hat{n}_{lep} \hat{n}_{\nu}). \quad (\text{B.46})$$

The derivative of the neutrino energy can be calculated from the single components of its momentum:

$$\frac{\partial E_{\nu}}{\partial E_{\alpha}} = \frac{\partial}{\partial E_{\alpha}} \left(\sqrt{p_{\nu,x}^2 + p_{\nu,y}^2 + p_{\nu,z}^2} \right) = \frac{1}{E_{\nu}} \cdot \sum_i p_{\nu,i} \frac{\partial p_{\nu,i}}{\partial E_{\alpha}} = \sum_i n_{\nu,i} \frac{\partial p_{\nu,i}}{\partial E_{\alpha}} = \hat{n}_{\nu} \cdot \nabla_{E_{\alpha}} (\vec{p}_{\nu}), \quad (\text{B.47})$$

with $i := x, y, z$.

For the particular components of the neutrino momentum it is

$$p_{\nu,i} = - (p_{q,i} + p_{\bar{q},i} + p_{b_{had},i} + p_{b_{lep},i} + p_{lep,i}) \quad , i = x, y. \quad (\text{B.48})$$

Thus the gradient $\nabla_{E_{\alpha}} \vec{p}_{\nu} = \left(\frac{\partial p_{\nu,x}}{\partial E_{\alpha}}, \frac{\partial p_{\nu,y}}{\partial E_{\alpha}}, \frac{\partial p_{\nu,z}}{\partial E_{\alpha}} \right)^T$ is given by

$$\frac{\partial p_{\nu,i}}{\partial E_{\alpha}} = \begin{cases} -n_{\alpha,i} & , \alpha = q, \bar{q}, lep \\ -n_{\alpha,i} \cdot \frac{E_{\alpha}}{\sqrt{E_{\alpha}^2 - m_{\alpha}^2}} & , \alpha = b_{had}, b_{lep} \end{cases} \quad , i = x, y, \quad (\text{B.49})$$

where the z-component is more complicated and given by

$$\frac{\partial p_{\nu,z}^{(1,2)}}{\partial E_{\alpha}} = a p_{lep,z} \cdot \frac{\partial b}{\partial E_{\alpha}} \pm \frac{\left(a^2 p_{lep,z}^2 + a \right) 2b \cdot \frac{\partial b}{\partial E_{\alpha}} - 2a E_{lep}^2 \left(p_{\nu,x} \cdot \frac{\partial p_{\nu,x}}{\partial E_{\alpha}} + p_{\nu,y} \cdot \frac{\partial p_{\nu,y}}{\partial E_{\alpha}} \right)}{2 \cdot \sqrt{a^2 b^2 \cdot p_{lep,z}^2 + a b^2 - a \cdot E_{lep}^2 \cdot (p_{\nu,x}^2 + p_{\nu,y}^2)}} \quad (\text{B.50})$$

for $\alpha = q, \bar{q}, b_{lep}, b_{had}$. With the auxiliary variables

$$t_{10} := a^2 b^2 \cdot 2p_{lep,z} \cdot \frac{\partial p_{lep,z}}{\partial E_{lep}} \quad (\text{B.51})$$

$$t_{11} := p_{lep,z}^2 \cdot \left(a^2 2b \frac{\partial b}{\partial E_{lep}} + b^2 2a \frac{\partial a}{\partial E_{lep}} \right) \quad (\text{B.52})$$

$$t_{12} := a 2b \frac{\partial b}{\partial E_{lep}} \quad (\text{B.53})$$

$$t_{13} := b^2 \frac{\partial a}{\partial E_{lep}} \quad (\text{B.54})$$

$$t_{14} := - \left(\frac{\partial a}{\partial E_{lep}} + a 2E_{lep} \right) (p_{\nu,x}^2 + p_{\nu,y}^2) \quad (\text{B.55})$$

$$t_{15} := -a E_{lep}^2 \left(2p_{\nu,x} \frac{\partial p_{\nu,x}}{\partial E_{lep}} + 2p_{\nu,y} \frac{\partial p_{\nu,y}}{\partial E_{lep}} \right), \quad (\text{B.56})$$

the derivative of the z -component of the neutrino momentum is

$$\frac{\partial p_{\nu,z}^{(1,2)}}{\partial E_{lep}} = ab \cdot n_{lep,z} + p_{lep,z} \left(a \frac{\partial b}{\partial E_{lep}} + b \frac{\partial a}{\partial E_{lep}} \right) \quad (\text{B.57})$$

$$\pm \frac{t_{10} + t_{11} + t_{12} + t_{13} + t_{14} + t_{15}}{2 \cdot \sqrt{a^2 b^2 \cdot p_{lep,z}^2 + ab^2 - a \cdot E_{lep}^2 \cdot (p_{\nu,x}^2 + p_{\nu,y}^2)}} \quad (\text{B.58})$$

with the partial derivatives

$$\begin{aligned} \frac{\partial a}{\partial E_{lep}} &= -2 \cdot \frac{p_{lep,x} n_{lep,x} + p_{lep,y} n_{lep,y}}{(p_{lep,x}^2 + p_{lep,y}^2)^2} \\ \frac{\partial b}{\partial E_{\alpha}} &= \begin{cases} -p_{lep,x} n_{\alpha,x} - p_{lep,y} n_{\alpha,y} & , \alpha = q, \bar{q} \\ -p_{lep,x} n_{\alpha,x} \frac{E_{\alpha}}{\sqrt{E_{\alpha}^2 - m_{\alpha}^2}} - p_{lep,y} n_{\alpha,y} \frac{E_{\alpha}}{\sqrt{E_{\alpha}^2 - m_{\alpha}^2}} & , \alpha = b_{had}, b_{lep} \\ -p_{lep,x} n_{\alpha,x} - p_{lep,y} n_{\alpha,y} - n_{lep,x} p_{\alpha,x} - n_{lep,y} p_{\alpha,y} & , \alpha = lep. \end{cases} \end{aligned} \quad (\text{B.59})$$

Thereby, the derivatives concerning the b -quarks look a bit different because of the consideration of their mass:

$$\frac{\partial |\vec{p}|}{\partial E} = \frac{\partial}{\partial E} \left(\sqrt{E^2 - m^2} \right) = \frac{E}{\sqrt{E^2 - m^2}}. \quad (\text{B.60})$$

If the KF is performed including the transverse momentum of the $t\bar{t}$ system, the derivatives of $p_{t\bar{t},x}$ and $p_{t\bar{t},y}$ must be calculated:

$$\frac{\partial f_1}{\partial p_{t\bar{t},i}} = 2 \cdot \left[- (E_{b_{lep}} + E_{lep}) \frac{\partial E_{\nu}}{p_{t\bar{t},i}} + (\vec{p}_{b_{lep}} + \vec{p}_{lep}) \cdot \frac{\partial \vec{p}_{\nu}}{\partial p_{t\bar{t},i}} \right], \quad i = x, y, \quad (\text{B.61})$$

where

$$\frac{\partial E_{\nu}}{\partial p_{t\bar{t},i}} = \frac{\partial}{\partial p_{t\bar{t},i}} \left(\sqrt{p_{\nu,x}^2 + p_{\nu,y}^2 + p_{\nu,z}^2} \right) = \frac{1}{E_{\nu}} \cdot \left(p_{\nu,x} \cdot \frac{\partial p_{\nu,x}}{\partial p_{t\bar{t},i}} + p_{\nu,y} \cdot \frac{\partial p_{\nu,y}}{\partial p_{t\bar{t},i}} + p_{\nu,z} \cdot \frac{\partial p_{\nu,z}}{\partial p_{t\bar{t},i}} \right), \quad (\text{B.62})$$

with

$$\frac{\partial p_{\nu,j}}{\partial p_{t\bar{t},i}} = \delta_{ij}, \quad j = x, y, \quad i = x, y, \quad (\text{B.63})$$

and

$$\frac{\partial p_{\nu,z}^{(1,2)}}{\partial p_{t\bar{t},i}} = a \cdot p_{lep,z} \cdot \frac{\partial b}{\partial p_{t\bar{t},i}} \pm \frac{\sqrt{t_{16} + t_{17} + t_{18}}}{2 \cdot \sqrt{a^2 b^2 p_{lep,z}^2 + ab^2 - aE_{lep}^2 \cdot (p_{\nu,x}^2 + p_{\nu,y}^2)}}. \quad (\text{B.64})$$

Thereby, the following auxiliary variables have been defined:

$$a := \frac{1}{p_{lep,x}^2 + p_{lep,y}^2} \quad (\text{B.65})$$

$$b := \frac{m_W^2}{2} + (p_{lep,x} p_{\nu,x} + p_{lep,y} p_{\nu,y}) \quad (\text{B.66})$$

$$t_{16} := a^2 \cdot 2b \cdot p_{lep,z}^2 \cdot \frac{\partial b}{\partial p_{t\bar{t},i}} \quad (\text{B.67})$$

$$t_{17} := a \cdot 2 \cdot b \cdot \frac{\partial b}{\partial p_{t\bar{t},i}} \quad (\text{B.68})$$

$$t_{18} := -aE_{lep}^2 \cdot \frac{\partial}{\partial p_{t\bar{t},i}} (p_{\nu,x}^2 + p_{\nu,y}^2) = -aE_{lep}^2 \cdot 2p_{\nu,i} \quad (\text{B.69})$$

with

$$\frac{\partial b}{\partial p_{t\bar{t},i}} = \frac{\partial}{\partial p_{t\bar{t},i}} \left[\frac{m_W^2}{2} + (p_{lep,x} p_{\nu,x} + p_{lep,y} p_{\nu,y}) \right] = p_{lep,i}, \quad i = x, y. \quad (\text{B.70})$$

For the solution the same sign is chosen as for the reconstruction of the neutrino.

C. A Brief Outline of a Likelihood Function

Here the realisation of a Likelihood function \mathcal{L} is briefly outlined. The Likelihood function evaluates the quality of a fit by its value, analogous to the Lagrange function: The smaller the value of the Likelihood function, the better fit the estimated values the measured quantities with respect to the constraints. It evaluates the probability to measure a particular set of data under the assumption of certain distributions of the fit parameters.

In Equation (C.1) an example of the implementation of the Likelihood function is given.

$$\mathcal{L} := \underbrace{\sum_{\alpha} \frac{(E'_{\alpha} - E_{\alpha})^2}{\sigma_{\alpha}'^2}}_{=: t_1 = \text{energy parameters}} - \underbrace{2 \ln \left(\frac{\Gamma_{\Delta t}}{\Delta m_t^2 + \Gamma_{\Delta t}^2/4} \right)}_{=: t_2 = \text{equal mass constraint}} - \underbrace{2 \ln \left(\frac{1}{\Delta m_{W,had}^2 + m_{W,pol}^2 \cdot \Gamma_W^2} \right)}_{=: t_3 = \text{first } W\text{-mass constraint}} - \underbrace{2 \ln \left(\frac{1}{\Delta m_{W,lep}^2 + m_{W,pol}^2 \cdot \Gamma_W^2} \right)}_{=: t_4 = \text{second } W\text{-mass constraint}}, \quad (\text{C.1})$$

with $\alpha := q, \bar{q}, b_{had}, b_{lep}, lep$, $\Gamma_{\Delta t} := 3.1 \text{ GeV}/c^2$ being the width of the Breit-Wigner distributed top quark mass difference of the top- and anti-top quark, $\Gamma_W := 2.141 \text{ GeV}/c^2$ being the width of the Breit-Wigner distributed W boson mass and $m_{W,pol} := 80.403 \text{ GeV}/c^2$ the pole mass of the W boson [6]. Thereby, the following quantities have been defined:

$$\Delta m_t^2 := (p_q + p_{\bar{q}} + p_{b_{had}})^2 - (p_{b_{lep}} + p_{lep} + p_{\nu})^2 \quad (\text{C.2})$$

$$\Delta m_{W,had} := (p_q + p_{\bar{q}})^2 - m_{W,pol}^2 \quad (\text{C.3})$$

$$\Delta m_{W,lep} := (p_{lep} + p_{\nu})^2 - m_{W,pol}^2. \quad (\text{C.4})$$

The first term t_1 considers a Gaussian-like distribution of the energy resolution of the measured particles. t_2 takes the equal mass constraint into account. Thereby, the difference of the two top quark masses, which are reconstructed from their decay products, is assumed to be Breit-Wigner distributed with a width of $\Gamma_{\Delta t} := 3.1 \text{ GeV}/c^2$ (the linear sum of the widths of both the top- and the anti-top quark). The Breit-Wigner probability distribution $p(x)$ of a quantity x with a mean M and a width Γ is described by

$$p(x) := \frac{1}{2\pi} \frac{\Gamma}{(x - M)^2 + \Gamma^2/4} \quad (\text{C.5})$$

$$p(x) \propto \frac{1}{(x^2 - M^2)^2 + M^2\Gamma^2} \quad (\text{relativistic approximation}). \quad (\text{C.6})$$

Note, that for the equal mass constraint the relativistic approximation of the Breit-Wigner distribution cannot be used. This is due to the fact that the mean of the mass difference is assumed to be zero. Thus in the relativistic approximation the denominator of Equation (C.6) would become zero for equal top- and anti-top quark masses.

t_3 takes the first W -mass constraint into account by using the relativistic Breit-Wigner distribution. Analogous the second W -mass constraint could be taken into account by term t_4 .

Bibliography

- [1] The Tevatron Electroweak Working Group for the CDF and DØ Collaborations, *Combination of CDF and DØ Results on the Mass of the Top Quark*, (March 2008), FERMILAB-TM-2403-E.
- [2] S. L. Glashow, *Partial Symmetries of Weak Interactions*, Nucl. Phys. **22** (1961) 579.
- [3] S. Weinberg, *A Model of Leptons*, Phys. Rev. Lett. **19** (1967) 1264.
- [4] C. Berger, *Elementarteilchenphysik*, Springer, 2nd edn., (2006).
- [5] P. W. Higgs, *Broken Symmetries, Massless Particles and Gauge Fields*, Phys. Lett. **12** (1964) 132.
- [6] The Particle Data Group Collaboration, W. M. Yao *et al.*, *Review of particle physics*, J. Phys. **G33** (2006) 1.
- [7] J. G. Learned, *The discovery of neutrino oscillations and mass: The disappearance of muon-neutrinos*, Prepared for 23rd Johns Hopkins Workshop on Current Problems in Particle Theory: Neutrinos in the New Millennium, Baltimore, Maryland, 10-12 Jun 1999.
- [8] The Super-Kamiokande Collaboration, Y. Ashie *et al.*, *Evidence for an oscillatory signature in atmospheric neutrino oscillation*, Phys. Rev. Lett. **93** (2004) 101801, hep-ex/0404034.
- [9] M. C. Gonzalez-Garcia and Y. Nir, *Developments in neutrino physics*, Rev. Mod. Phys. **75** (2003) 345, hep-ph/0202058.
- [10] The DØ Collaboration, S. Abachi *et al.*, *Observation of the Top Quark*, Phys. Rev. Lett. **74** (1995) 2632, hep-ex/9503003.
- [11] The CDF Collaboration, F. Abe *et al.*, *Observation of Top Quark Production in $p\bar{p}$ Collisions with the Collider Detector at Fermilab*, Phys. Rev. Lett. **74** (1995) 2626, hep-ex/9503002.
- [12] The ALEPH, DELPHI, L3, OPAL, SLD Collaborations, the LEP Electroweak Working Group, the SLD Electroweak and Heavy Flavour Groups, *Precision Electroweak Measurements on the Z Resonance*, Phys. Rept. **427** (2006) 257, hep-ex/0509008.
- [13] CERN, <http://lepewwg.web.cern.ch/LEPEWWG/plots/winter2008/>.
- [14] <http://durpdg.dur.ac.uk/hepdata/pdf3.html>.
- [15] R. S. Thorne, A. D. Martin, and W. J. Stirling, *MRST parton distributions: Status 2006*, hep-ph/0606244.

- [16] *Combination of CDF top quark pair production cross section measurements with up to 760 pb⁻¹*, CDF-Note 8148.
- [17] *Measurement of the $t\bar{t}$ Production Cross Section in $p\bar{p}$ Collisions at $\sqrt{s} = 1.96$ TeV*, DØ-Note 192004.
- [18] R. Bonciani, S. Catani, M. L. Mangano, and P. Nason, *NLL resummation of the heavy-quark hadroproduction cross-section*, Nucl. Phys. **B529** (1998) 424, hep-ph/9801375.
- [19] N. Kidonakis, *Single top production at the Tevatron: Threshold resummation and finite-order soft gluon corrections*, Phys. Rev. **D74** (2006) 114012, hep-ph/0609287.
- [20] The DØ Collaboration, V. M. Abazov *et al.*, *Evidence for production of single top quarks and first direct measurement of $|V_{tb}|$* , Phys. Rev. Lett. **98** (2007) 181802, hep-ex/0612052.
- [21] The CDF Collaboration, *Combination of CDF Single Top Quark Searches with 2.2 fb⁻¹ of Data*, CDF note 9251.
- [22] The DØ Collaboration, V. M. Abazov *et al.*, *Evidence for production of single top quarks*, 0803.0739.
- [23] J. P. Koutchouk, *Investigations of the parameter space for the LHC luminosity upgrade*, Prepared for European Particle Accelerator Conference (EPAC 06), Edinburgh, Scotland, 26-30 Jun 2006.
- [24] O. Bruning *et al.*, *LHC Design Report. Vol. I: The LHC main ring*, CERN-2004-003-V-1.
- [25] O. Bruning *et al.*, *LHC Design Report. Vol. II: The LHC infrastructure and general services*, CERN-2004-003-V-2.
- [26] M. Benedikt, P. Collier, V. Mertens, J. Poole, and K. Schindl, *LHC Design Report. 3. The LHC injector chain*, CERN-2004-003-V-3.
- [27] The CMS Collaboration, G. L. Bayatian *et al.*, *CMS physics: Technical Design Report*, CERN-LHCC-2006-001.
- [28] The CMS Collaboration, G. L. Bayatian *et al.*, *CMS Technical Design Report, Volume II: Physics performance*, J. Phys. **G34** (2007) 995.
- [29] *ALICE TRD Technical Design Report*, alice tdr 9 edn., (October 2001), CERN/LHCC 2001-021.
- [30] *LHCb: Technical Proposal*, Tech. Proposal, CERN, Geneva, (1998), CERN/LHCC 98-004.
- [31] *LHCf – Technical Design Report of the LHCf experiment*, (February 2006), CERN/LHCC 2006-004.
- [32] *TOTEM – Technical Design Report*, totem-tdr-001 edn., (January 2004), CERN/LHCC 2004-02.
- [33] M. Oriunno *et al.*, *The Roman Pot for LHC*, Prepared for European Particle Accelerator Conference (EPAC 06), Edinburgh, Scotland, 26-30 Jun 2006.

-
- [34] The ATLAS Collaboration, *ATLAS: Letter of intent for a general purpose $p p$ experiment at the large hadron collider at CERN*, CERN-LHCC-92-04.
- [35] D. Froidevaux, M. Vincker, *et al.*, *The ATLAS Experiment at the CERN Large Hadron Collider – Submitted version of the ATLAS Detector Paper*, (February 2007).
- [36] The ATLAS Collaboration, M. S. Alam *et al.*, *ATLAS Pixel Detector: Technical Design Report*, CERN-LHCC-98-13.
- [37] The ATLAS Collaboration, *ATLAS Inner Detector: Technical Design Report. Vol. 1*, CERN-LHCC-97-16.
- [38] The ATLAS Collaboration, *ATLAS Inner Detector: Technical Design Report. Vol. 2*, CERN-LHCC-97-17.
- [39] R. Wigmans, *Calorimetry – Energy Measurement in Particle Physics*, Oxford Science Publications, (2000).
- [40] The ATLAS Collaboration, *ATLAS Tile Calorimeter: Technical Design Report*, CERN-LHCC-96-42.
- [41] The ATLAS Collaboration, A. Airapetian *et al.*, *ATLAS Calorimeter Performance*, CERN-LHCC-96-40.
- [42] The ATLAS Collaboration, A. Airapetian *et al.*, *ATLAS Liquid Argon Calorimeter: Technical Design Report*, CERN-LHCC-96-41.
- [43] The ATLAS Collaboration, A. Airapetian *et al.*, *ATLAS Calorimeter Performance Technical Design Report*, CERN-LHCC-96-40.
- [44] The ATLAS Collaboration, *ATLAS Muon Spectrometer: Technical Design Report*, CERN-LHCC-97-22.
- [45] The ATLAS Collaboration, *ATLAS Magnet System: Technical Design Report*, CERN-LHCC-97-18.
- [46] The ATLAS Collaboration, *ATLAS Central Solenoid: Technical Design Report*, CERN-LHCC-97-21.
- [47] The ATLAS Collaboration, *ATLAS Barrel Toroid: Technical Design Report*, CERN-LHCC-97-19.
- [48] The ATLAS Collaboration, *ATLAS End-cap Toroids: Technical Design Report*, CERN-LHCC-97-20.
- [49] ATLAS Level-1 Trigger Group, *Level-1 Trigger Technical Design Report*, (1998).
- [50] ATLAS HLT/DAQ/DCS Group, *High-Level Trigger, Data Acquisition and Controls Technical Design Report*, (July 2003), CERN-LHCC-2003-022.
- [51] R. Brun, F. Rademakers, P. Canal, I. Antcheva, and D. Buskulic, *ROOT – An Object-Orientated Data Analysis Framework*, users guide 5.16 edn., (July 2007).
- [52] F. James and M. Roos, *Minuit: A System for Function Minimization and Analysis of the Parameter Errors and Correlations*, Comput. Phys. Commun. **10** (1975) 343.
-

- [53] V. Blobel and E. Lohrmann, *Statistische und numerische Methoden der Datenanalyse*, Teubner Studienbücher, (1998).
- [54] R. J. Barlow, *A Guide to the Use of Statistical Methods in the Physical Sciences*, The Manchester Physics Series, Wiley, (1989).
- [55] L. Lyons, *Statistics for Nuclear and Particle Physicists*, Cambridge, Uk: Univ. Pr. (1986) 226p.
- [56] O. Forster, *Analysis 2 – Differentialrechnung im R^n , Gewöhnliche Differentialgleichungen*, Vieweg Studium, (1984).
- [57] F. Maltoni and T. Stelzer, *MadEvent: Automatic event generation with MadGraph*, JHEP **02** (2003) 027, [hep-ph/0208156](#).
- [58] T. Stelzer and W. F. Long, *MadGraph - Minimal User Guide*, (1994), [arXiv:hep-ph/9401258](#)].
- [59] F. Maltoni and T. Stelzer, *MadEvent: Automatic event generation with MadGraph*, JHEP **02** (2003) 027, [hep-ph/0208156](#).
- [60] R. Brun, R. Hagelberg, M. Hansroul, and J. C. Lassalle, *GEANT: Simulation Program for Particle Physics Experiments. User Guide and Reference Manual*, CERN-DD-78-2-REV.
- [61] A. Shibata, *TopView - an AOD analysis package for ATLAS top physics analysis*, (May 2007), [ATL-SOFT-PUB-2007-002](#).
- [62] The ATLAS Collaboration, S. Bentvelsen and M. Cornelius, *Top studies for the Atlas detector commissioning*, CERN ATL-PHYS-PUB-2005-024.

Acknowledgements

I wish to acknowledge the contribution of a number of people without whose assistance and support the completion of this thesis would not have been possible.

First of all, I would like to thank Prof. Arnulf Quadt for introducing me to the field of particle physics and his willingness to supervise this thesis. I am also grateful that he offered me the opportunity to participate in laboratory work at DESY.

A special thank you goes to Dr. Kevin Kröniger for his constant guidance and encouragement and the relaxed atmosphere he managed to create. He advised me patiently and readily gave his time to discuss my work.

I am grateful to all the other members of the hep-group for their constant support and suggestions and for the pleasant and relaxed atmosphere.

Balint Radics' (Bonn University) very useful advice concerning all technical issues is gratefully acknowledged.

Finally, I would like to extend my heartfelt gratitude to my family and friends for their support. My parents made it possible for me to study and helped me in every conceivable way. I particularly want to thank my brother Alexander for his late-night visits. Cheers to Sylvia, Tatjana, Alexander M. for the refreshing coffee breaks. And, last but not least, I would like to thank my girlfriend Marion, who cheered me up with her cheekiness when I needed it most.